Gravity and Gas Density Effects on Annular Flow Average Film Thickness and Frictional Pressure Drop.

A Thesis

submitted to the College of Graduate Studies and Research

in partial fulfillment of the requirements for

the Degree of

Master of Science

in

the Department of Mechanical Engineering

at the

University of Saskatchewan

by

Ryan M. MacGillivray

PERMISSION TO USE

In presenting this thesis in partial fulfillment of the requirements for a Post-graduate degree from the University of Saskatchewan, I agree that the Libraries of this University may make it freely available for inspection. I further agree that permission for copying of this thesis in any manner, in whole or in part, for scholarly purposes may be granted by Dr. K. S. Gabriel or, in his absence, by the Head of the Department of Mechanical Engineering or the Dean of the College of Engineering of the University of Saskatchewan. It is understood that any copying or publication or use of this thesis or parts thereof for financial gain shall not be allowed without my written permission. It is also understood that due recognition shall be given to me and to the University of Saskatchewan in any use which may be made of any material in this thesis.

Requests for permission to copy or to make other use of the material in this thesis in whole or in part should be addressed to:

R. M. MacGillivray
ryan.macgillivray@usask.ca

or

Head of the Department of Mechanical Engineering
University of Saskatchewan
57 Campus Drive
Saskatoon, Saskatchewan
S7N 5A9

ABSTRACT

Annular flow is an important flow regime in many industrial applications. The need for a better understanding of this flow regime is driven by the desire to improve the design of many terrestrial and space-based systems. Annular two-phase flow is frequently present in the drilling, production and transportation of oil and natural gas, boilers and condensers, and in heating and refrigeration systems. The flow regime is also important for the refueling of space vehicles, and heating and refrigeration systems for space use.

Past studies on annular flow have dealt with varying the gas or liquid Reynolds numbers and studying the effect of such changes on the flow regimes and pressure drops. The effect of two other relevant dimensionless groups, namely the gas-to-liquid density ratio and the gas-to-liquid viscosity ratio, on the film characteristics are noticeably absent. As well, with the increased interest in the space environment, studies on the effect of the gravitational acceleration on two-phase flow would be beneficial.

The effect of the gas density and the gravitational acceleration on the annular flow average film thickness and frictional pressure drop are examined. The film thickness was measured using two-wire conductance probes. Experimental data were collected in microgravity and hypergravity aboard the Novespace Zero-G Airbus microgravity simulator and normal gravity data were collected at the University of Saskatchewan. Data were collected for a range of annular flow set points by changing the liquid and gas mass flow rates. The liquid-to-gas density ratio was examined by collecting annular flow data using helium-water and air-water. The gravitational effect on the film

thickness characteristics was examined by collecting the data during the microgravity and pull-up (hypergravity) portions of each parabolic flight.

A direct comparison is possible between the normal gravity data and the microgravity data, due to the matching of the liquid and gas mass flow rates and the flow regime. The reduction in gravity causes the average film thickness to increase between two and four times from the normal gravity values. The microgravity average frictional pressure drop is within approximately 20% of the normal gravity pressure drop for the same flow conditions. For all gravity levels, the air-water and the helium-water flows give similar results, for both average film thickness and frictional pressure drop, when based on the specific energy of the gas.

The hypergravity average film thickness results are larger than at normal gravity for the same flow conditions. However, no flow regime map exists for the hypergravity condition, so the similarity of the flow regime cannot be confirmed. The hypergravity flow appears more chaotic, and may be in the transition from a churn type flow. The average frictional pressure drop is increased by approximately 20% due to the increase in the gravitational acceleration.

New non-dimensional equations, which include the effect of the gas density, are presented for each gravity level to predict the average film thickness and the average frictional pressure drop.

ACKNOWLEDGEMENTS

I would like to thank my supervisor, Prof. K. Gabriel, for his guidance and support of this project and for the opportunity for the microgravity experience. I would also like to acknowledge the invaluable support from my committee members, Prof. D. Torvi and Prof. G. Schoenau, and from the other engineering professors, including Prof. C. Hawkes, Prof. J. Bugg, Prof. B. Besant, Prof. C. Simonson and Prof. W. Szyzkowski for their help.

The work on this thesis would not have been possible without the financial assistance from the Department of Mechanical Engineering, the University of Saskatchewan and the Microgravity Science program of the Canadian Space Agency.

Great thanks are extended to Mr. Vladimir Pletser, European Space Agency, Mr. Christophe Mora and Mr. Thierry Gharib, Novespace, Dr. Andre Kuipers, astronaut, ESA, Mr. Eric Vachon, Project Manager, CSA and Dr. Catherine Colin, Institute des Mechanics de Fluids en Toulouse for the exciting opportunity and invaluable assistance with the microgravity flight campaigns.

Other members of the University of Saskatchewan who provided necessary support and assistance throughout this project include Mr. Dave Deutscher of the Thermodynamics Laboratory and Mr. Henry Berg, Mr. Dan Vessey, Mr. Bob Wilson and Mr. Keith Palmorea of Engineering Shops. The help of the other members of the Microgravity Research Group, including graduate students Mr. Tom MacDermott, Mr. Umesh Ariyadasa, Mr. Zhenfeng Zhu, Mr. Pieter de Jong, Mr. Huawei Han and Mr. Forrest Wong is appreciated, as well as the help from the undergraduate students during the summer months: Mr. Travis Wiens, Mr. Dave Cote, Mr. Devon Manz, Mr. Jonathan Moore, Ms. Nanette Robertson.

Finally, I would like to acknowledge the support and encouragement provided by both the Nogier and the MacGillivray families. Thank you for your help, encouragement and support.

Great thanks to my fiancée, Margaret Nogier. Thank you for always being there.

TABLE OF CONTENTS

LIST OF TABLES

LIST OF FIGURES

NOMENCLATURE

A	tube cross sectional area [m^2]
A	constant used in equation 1-10
B	constant used in equation 1-10
B( )	bias uncertainty of value
C	constant used in equation 1-20
d	tube diameter [m]
dP/dz_f	frictional pressure drop per unit length [Pa/m]
$dP/dz_{g,f}$	gas frictional pressure drop per unit length [Pa/m]
$dP/dz_{2\text{-}\Phi,f}$	two-phase flow frictional pressure drop [Pa/m], $= (-dP/dz)_{g,f} * \Phi^2_g$
Eu	Euler number, ratio of the pressure force to the inertial force, $= (dP/dz) * \{d / (\rho_l V_{sl}^2)\}$
f	Darcy friction factor
f_i	interfacial friction factor
Fr_{go}	gas Froude number, $= V_{sg} / (g\ d)^{0.5}$
g	gravitational acceleration [m/s^2]
g_o	normal, earth based gravitational acceleration [9.81 m/s^2]
G_g	gas mass flux [kg/m^2s], $= \dot{m}_g / A$
G_l	liquid mass flux [kg/m^2s] , $= \dot{m}_l / A$
G_{lf}	liquid film mass flux [kg/m^2s], $= \dot{m}_{lf} / (\pi\ d)$
L	length [m]
M	gas molecular weight [kg/kmol]
$\dot{m}_g$	gas mass flow rate [kg/s]
$\dot{m}_l$	liquid mass flow rate [kg/s]
$\dot{m}_{lf}$	liquid film mass flow rate [kg/s]
$\dot{m}_p$	phase mass flow rate [kg/s]
m^+	non-dimensional film thickness, $= \delta\ U_l^* / \nu_l$
P	absolute pressure [kPa]
P ( )	Precision uncertainty of value
R	universal gas constant [8.314 kJ/kg*K]
Re_g	actual gas Reynolds number
Re_l	actual liquid Reynolds number
Re_{lf}	liquid film Reynolds number, $= 4\ G_{lf} / \mu_l$
Re_{lo}	liquid only Reynolds number, $= (G_l + G_g)\ d / \mu_l$
Re_{sl}	superficial liquid Reynolds number, $= \rho_l V_{sl}\ d / \mu_l$
T	absolute temperature [K]
U_l^*	liquid friction velocity [m/s], $= (\tau_i / \rho_l)^{0.5}$
U( )	total uncertainty of (value), $= \{B( )^2 + P( )^2\}^{1/2}$
V*	normalized film thickness voltage, $= (V - V_a) / (V_w - V_a)$
V	two-phase voltage recorded by the film thickness sensor
V_a	all-air voltage recorded by the film thickness sensor

V_{sg} superficial gas velocity, velocity of gas flowing alone in the tube [m/s], $= \dot{m}_g / (\rho_g A)$

V_{sl} superficial liquid velocity, velocity of liquid flowing alone in the tube [m/s], $= \dot{m}_l / (\rho_l A)$

V_{sp} superficial velocity of given phase, velocity of phase flowing alone in the tube [m/s], $= \dot{m}_p / (\rho_p A)$

V_w all-water voltage recorded by the film thickness sensor

We_{sg} superficial gas Weber number, $= \rho_g V_{sg}^2 d / \sigma$

We_{sl} superficial liquid Weber number, $= \rho_l V_{sl}^2 d / \sigma$

We_{sp} superficial Weber number of given phase, $= \rho_p V_{sp}^2 d / \sigma$

x gas quality, $= \dot{m}_g / (\dot{m}_g + \dot{m}_l)$

X ratio of the single-phase pressure drops, $= \{(dP/dz_{l,f}) / (dP/dz_{g,f})\}^{0.5}$

Greek Symbols:

δ film thickness [m]

ΔP pressure drop [Pa]

Φ^2_g two-phase multiplier, ratio of the two-phase frictional pressure drop to the gas frictional pressure drop

μ_g gas dynamic viscosity [N s/m^2]

μ_l liquid dynamic viscosity [N s/m^2]

ν_l liquid kinematic viscosity [m^2 /s]

ν_w kinematic viscosity of water [m^2 /s]

ρ_g gas density [kg/m^3], $= P / \{(R / M) T\}$

ρ_h homogeneous density [kg/m^3], $= \{(x / \rho_g) + (1 - x) / \rho_l\}^{-1}$

ρ_l liquid density [kg/m^3]

ρ_p phase density [kg/m^3]

σ surface tension [N/m]

τ_i interfacial shear stress [kg/s^2 m]

ϑ angle of inclination from horizontal [rad] in Equation (3-4)

LIST OF ACRONYMS

AC	Alternating Current
CSA	Canadian Space Agency
DC	Direct Current
ESA	European Space Agency
GE	General Electric
ID	Inner Diameter
LabVIEW©	Laboratory Virtual Instrumentation and Engineering Workbench©
LPM	Litres Per Minute
NASA	National Aeronautics and Space Administration
PDF	Power Density Function
RMS	Root Mean Square
SLM	Standard Litres per Minute
VAC	Volts – Alternating Current
VDC	Volts – Direct Current

1.0 INTRODUCTION AND BACKGROUND

Over the past decade, a permanent human presence has been established in space and interest in nuclear power has increased. Further emphasis has been placed on energy efficiency as well as new methods of extracting the diminishing oil and natural gas reserves. Two-phase flows can be present in all of these situations, and play an important role in their operation, safety and cost. A poor understanding of the flow and its behavior can cause unsafe, inefficient or costly systems. Conversely, a proper understanding of the two-phase flow phenomenon will ensure that safety measures are identified and implemented during the design phase or that the system is operating at peak efficiency. Of particular interest in two-phase systems for design purposes are some of the characteristics of annular flow: the liquid film thickness and the frictional pressure drop. Knowledge of the liquid film thickness is necessary to avoid dry-out situations; either due to heat transfer or in shear-driven, adiabatic flows. Frictional pressure drop information is useful because it is related to the energy required to drive the two-phase flow system.

1.1 THESIS SCOPE

This thesis presents the results of an experimental study of adiabatic, two-phase flow. Vertical upward, co-current annular flow is examined using air-water and helium-water

flows in a 9.5 mm tube. The effect of the gas density and the gravitational acceleration on the annular average liquid film thickness and the two-phase frictional pressure drop are examined. The effect of the gas density is examined by repeating the flow conditions of air-water with helium-water. The gravitational acceleration is varied between earth (normal) gravity, microgravity, and hypergravity through the use of a parabolic aircraft and ground testing. The range of flows examined includes liquid mass fluxes between 76 and 314 kg/m^{2}s, air mass fluxes of 14.3 to 47.7 kg/m^{2}s, and helium mass fluxes of 5.0 to 11.6 kg/m^{2}s.

1.2 THESIS LAYOUT

This thesis is laid out as follows:

Chapter one will discuss the applications of two-phase flows, provide an overview of the various gas-liquid flow regimes, give an explanation of annular flow and outline the influence of a microgravity environment. A literature survey of past work in annular flow film thickness and pressure drop and a summary of the thesis objectives conclude the chapter.

Chapter two will detail the experimental facilities, including the experimental apparatus, the data collection instrumentation and the parabolic flight campaigns.

Chapter three will summarize the experimental test matrix, outline the data collection procedure, and explain the data selection and analysis, including the experimental uncertainty.

Chapter four will present a detailed comparison of the influence of the gas density and the gravitational acceleration on the annular flow film thickness and frictional pressure drop. Only the normal gravity and microgravity data will be discussed.

Chapter five will summarize the air-water and helium-water results for the hypergravity flows.

Chapter six will present new non-dimensional equations to be used to predict the annular flow film thickness and pressure drop in the varying gravity levels.

Chapter seven will summarize the conclusions based on the current work, and provide recommendations for future work.

1.3 TWO-PHASE FLOW APPLICATIONS

Two-phase flows can occur in many situations. The flow occurs when two immiscible substances flow together, and can be gas-solid (dust particles in air), liquid-solid (sedimentation), liquid-liquid (oil in water) or gas-liquid flows (steam and condensation).

Gas-liquid two-phase flows, in particular annular flow, can occur in a variety of industrial situations. Some of the main applications include water-cooled nuclear reactors, evaporators, boilers, condensers, heat exchangers, pipelines, steam-power and petrochemical plants, refrigeration and air-conditioning systems, chemical contacting

equipment, and other process equipment. Phase-change heat transfer is important in supercomputers with high-density multi-chip modules, high powered X-rays, heat exchangers in aerospace systems and satellite cryogenic cooling systems (Azzopardi, 1986; Willets, 1987; Keshock and Lin, 1996; Fukano and Furukawa, 1998; Ariyadasa and Rezkallah, 2001; Chen *et al.*, 2001; Wolf *et al.*, 2001; Zhao *et al.*, 2001; Zhao and Bi, 2001).

In steam heating applications, the steam vapor will invariably condense on the tube walls creating condensation. In refrigeration systems, the evaporation of the refrigerant will cause two-phase flow. Oil can be extracted from the ground using high-pressure steam, and causing the steam and oil to flow together. The high heat transfer rates associated with the boiling process make two-phase systems useful for cooling in the nuclear industry or for space applications where weight must be kept to a minimum. Thermal transport systems involving two-phase flow are lighter and more efficient than single-phase systems, so their use in space technology is desirable.

Two-phase flows are also expected to occur in other space applications, such as the refueling of space vehicles, design and operation of environmental and life support systems, wastewater reclamation units, transfer and storage of cryogenic fluids, space nuclear power systems safety and performance (both steady state and emergency situations), design and operation of an active thermal control system, cooling of electronic components and heat pipe applications, and mining of extra-terrestrial soils (Dukler *et al.*, 1988; Bousman, 1995; Keshock and Lin, 1996; Lowe and Rezkallah, 1999; Zhao *et al.*, 2001).

1.4 GAS-LIQUID FLOW REGIMES

In order to determine the flow characteristics, such as the pressure drop or film thickness, it is first necessary to know the flow regime present for the given flow conditions (Furukawa and Fukano, 2001). Within the gas-liquid two-phase flows, there can be a number of flow regimes based on the flow orientation and the gas-liquid interfacial structure (Mori *et al.*, 1999). The influence of gravity on the gas-liquid interface can be a complicating and dominating factor in the two-phase flow regimes. Therefore, microgravity two-phase flows are simpler (Zhao *et al.*, 2001). As gravity is reduced, a new balance is approached between inertial and surface forces (Colin *et al.*, 1991). The flow patterns present in microgravity flows are bubble, slug, frothy-annular and annular (Colin *et al.*, 1991; Zhao and Rezkallah, 1993; Bousman, 1995). These flow patterns can occur over a range of void fractions, which are a function of geometry, fluid properties, and system properties (Vassallo *et al.*, 2001). The void fraction is the ratio of the area of the gas core to the total tube cross-sectional area.

Most flow regime maps, however, are based on the gas and liquid superficial velocities (Rezkallah, 1990), which do not show how changing certain parameters will affect the flow regime. The superficial velocity for a given phase (V_{sp}) is the velocity of the fluid if it was flowing alone in the tube, and is calculated from

$$V_{sp} = \dot{m}_p / (\rho_p A) \qquad (1\text{-}1)$$

where $\dot{m}_p$ is the phase mass flow rate, ρ_p is the phase density and A is the tube cross-sectional area. Based on the work of Reinarts (1993), Bousman *et al.* (1996) suggested that an increase in the gas-to-liquid density ratio caused the transition to annular flow to

occur at lower void fractions and that the relative density of the gas phase to the liquid phase had a significant effect on the flow pattern map. Yang and Shieh (2001) reported similar results in that the transition to annular flow is shifted to lower V_{sg} with refrigerant R-134a, which has larger vapor and liquid densities than air-water. Witte *et al.* (1996) reported that the transition to annular was not significantly affected by changes in tube diameter or surface tension, however, Iguchi and Terauchi (2001) reported that the tube wettability affected the flow regime transitions and caused other flow regimes.

Figure 1.1 shows a non-dimensional flow regime map developed for vertical upwards and microgravity gas-liquid flows based on the Weber number estimated from the liquid and gas superficial velocities (Rezkallah, 1996). The Weber number (We) is given calculated from

$$We_{sp} = \rho_p V_{sp}^2 * d / \sigma, \qquad (1\text{-}2)$$

where d is the tube diameter, and σ is the interfacial surface tension. Annular flow exists in flows of We_{sg} greater than 20 for all liquid flows. For We_{sg} less than 1, both bubbly and slug flows are possible depending on the We_{sl}. At high We_{sl} the flow is bubbly, and at low We_{sl}, the flow is in the slug regime. The flow that occurs in between We_{sg} of 1 and 20 is a transitional flow, called frothy slug-annular or churn flow.

Flow patterns are usually obtained by visual observations, and so the flow pattern designation depends on individual interpretation of the observations and subjective judgment. Heppner *et al.* (1975) reported their observations of the flow regimes for

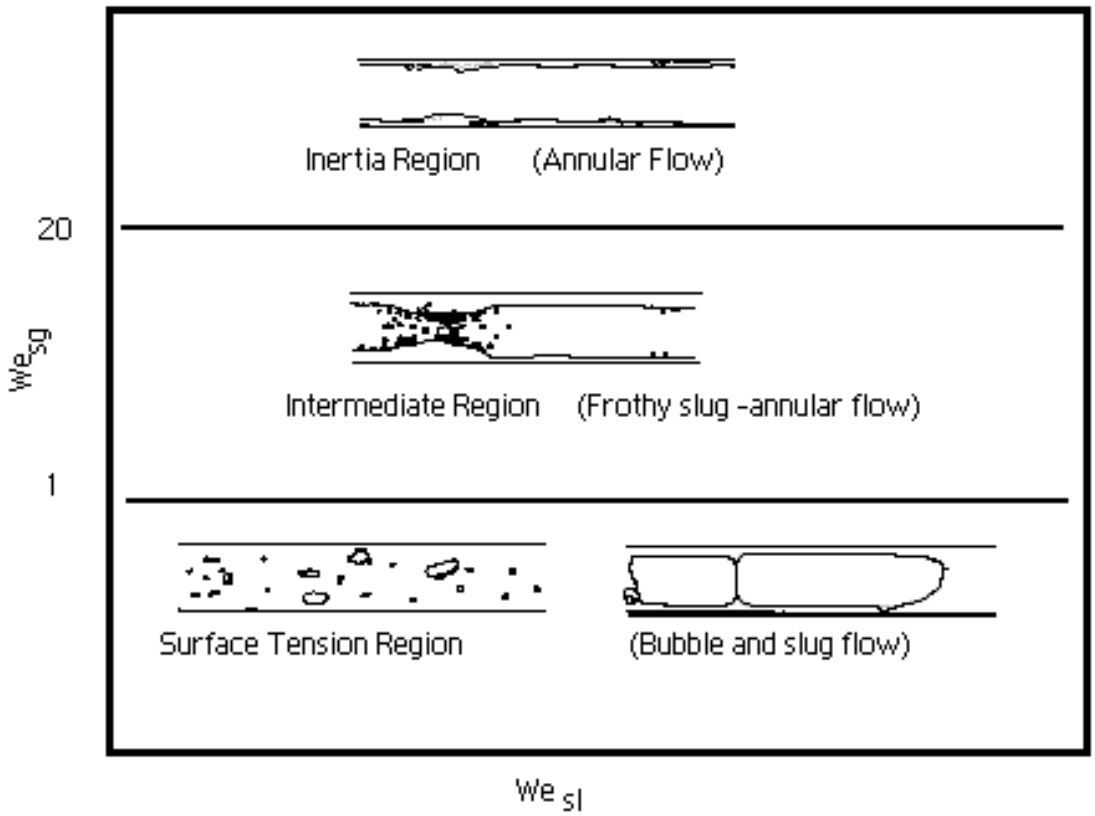

Figure 1.1. Weber number based flow regime map. (Rezkallah, 1996).

microgravity, normal gravity and hypergravity conditions, and stated that the categorization of the flow was often very difficult. More objective methods of determining the flow patterns were later developed based on statistical properties of the pressure signal or the Power Density Function (PDF) of the void fraction measuremetns (Matsui, 1984; Lowe and Rezkallah, 1999; Wu *et al.*, 2001).

The various flows are shown graphically in Figure 1.2 (de Jong, 1999). The flows, moving from left to right, represent increasing gas flows and/or decreasing liquid flows. All water, single-phase flow would be present on the left side of the graph and all gas flow would be on the right side.

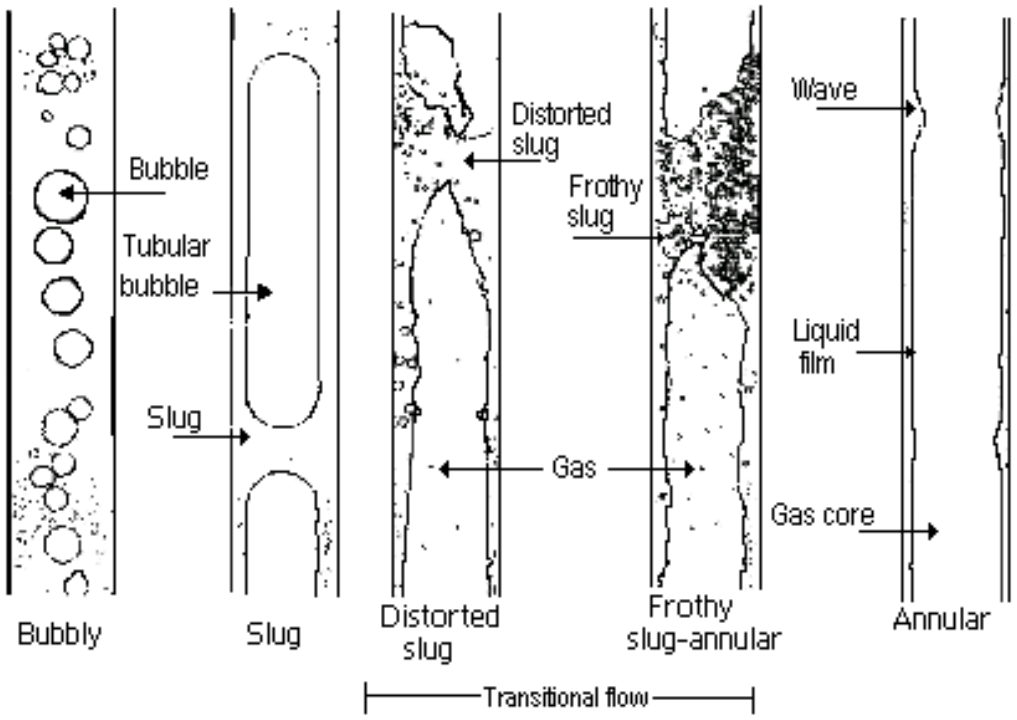

Figure 1.2. Microgravity two-phase flow regimes. (de Jong, 1999).

Bubbly flow occurs when small amounts of gas flows as spherical bubbles, generally flowing at the center of the tube. As the gas flow rate increases, the bubbles join together and form long, bullet-shaped bubbles, called "slugs", separated by sections of liquid. As the gas flow rate is increased further, the liquid bridges begin to collapse and the gas breaks through, creating a chaotic, churn flow. As the gas flow is further increased, the frequency of the liquid bridging becomes quite reduced. When gas and liquid flow concurrently at high gas velocities, an annular configuration is reached for which the liquid flows as a film along the wall and a small fraction as droplets entrained in the gas core (Asali *et al.*, 1985). The gas flows as a continuous phase at the center of the tube. This configuration of the two-phase flow regime is called annular flow. Annular flow can occur at qualities (x) of approximately 3% or higher (Azzopardi, 1986), and can occupy a large fraction of the length of a boiling channel (Willets, 1987).

1.5 ANNULAR FLOW

A typical annular flow is illustrated in Figure 1.3. Annular flow has two main components: the liquid film on the tube wall and the gas core (Azzopardi and Whalley, 1980). The majority of the liquid flows as a film uniformly distributed around the circumference (Asali *et al.*, 1985), while some of the liquid droplets are transported in the gas core. The interface between the liquid film and the gas core is highly dynamic and constantly changing. A common feature of this interface is the presence of large disturbance waves along with smaller ripple waves.

Long crested ripples having a steep front cover the film at low liquid flow rates. The surface is smooth and appears to be laminar between these waves. At high liquid flow rates, roll or disturbance waves appear on the film (Asali *et al.*, 1985). Disturbance waves are the most obvious feature of the liquid film in annular two-phase flows (Azzopardi and Whalley, 1980). At high gas velocities, the smaller ripple waves are still present (Mori *et al.*, 1999). One possible source of the entrained liquid droplets is the

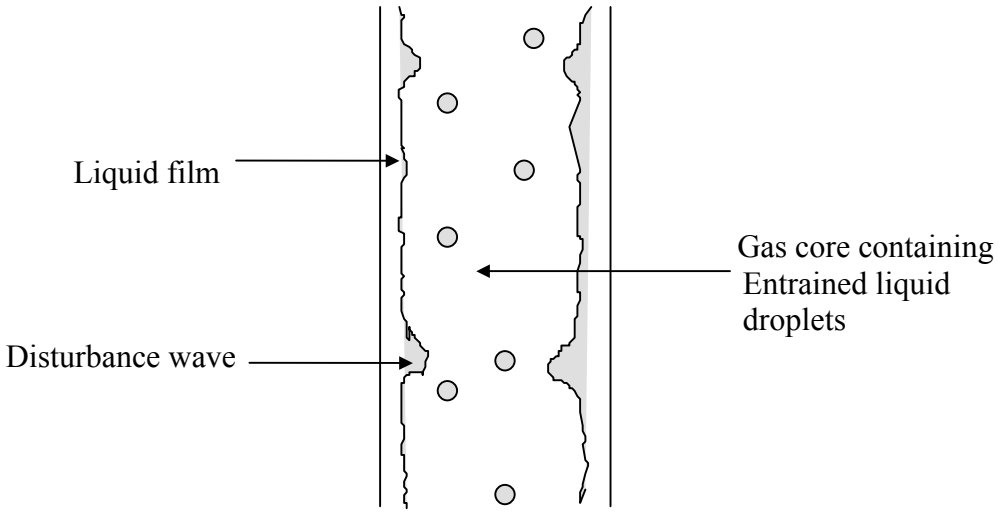

Figure 1.3. A typical annular flow.

gas shearing off the disturbance waves. This entrainment of liquid can cause a momentum transfer that can affect the velocity profile, pressure drop, film thickness and heat transfer (Ariyadasa, 2002). The largest heat transfer coefficients and frictional pressure drops can occur in annular flow (Witte *et al.*, 1996), requiring detailed knowledge of this flow regime.

1.6 NEED FOR A MICROGRAVITY ENVIRONMENT

In recent years, considerable research has been conducted on gas-liquid microgravity flows, in order to evaluate the flow patterns, pressure drops and heat transfer coefficients in a reduced gravity environment (Heppner *et al.*, 1975; Dukler *et al.*, 1988; Chen *et al.*, 1991; Colin *et al.*, 1991; Rite and Rezkallah, 1993; Bousman, 1995; Zhao *et al.*, 2001). The motivation has been to design effective thermal control systems for future spacecraft. Owing to its effects on two-phase flow, gravitational forces overwhelm the two-phase flow process on the ground. This is primarily due to the strong effects of gravity on the momentum and heat transfers in such flows. These effects are extremely difficult to distinguish and separate from others during ground-based experiments. The modeling of two-phase flow relies heavily on some empirical or semi-empirical constants to define the flow patterns and their transitions. The presence of a gravitational environment can complicate a gas-liquid two-phase flow, causing a variety of perturbations, instabilities and undesirable unsteady features (Keshock and Lin, 1996). A microgravity environment allows the study of the two-phase flow momentum and heat transfers in the absence of the masking effects of gravity, providing a better

understanding of the two-phase flow. Some of the features of microgravity flows that make them simpler than those at normal gravity are:

1) Around the tube circumference in microgravity annular flow, the waves are not of uniform shape or amplitude, however, the mean film thickness values are essentially equal. Therefore the flow can be considered axisymmetric (Bousman, 1995). In the presence of a gravity field, any deviation from vertical may cause the flow to be not be axisymmetric.
2) Though local variations in the void fraction do occur, the flow velocity in a channel of a constant cross section does not show periodic flow reversals. The flow reversals in normal gravity vertical upwards flow are due to the gas phase not maintaining sufficient energy to drive the liquid upwards against the gravitational pull.
3) In 1-g vertical upwards, annular flow, the liquid film is very thin owing to drainage by gravity. This makes it difficult to study the details of the flow in the disturbance wave region. In microgravity, the disturbance wave region can be studied at much lower gas velocities and more intensive measurements in the film can be made.
4) With a reduced gravitational acceleration, the total pressure drop is due to frictional and accelerational pressure drops. For a test section of fixed geometry (no singularities), changes due to accelerational pressure drop are significantly reduced, and the measured pressure drop would closely represent the contribution due to friction.

In normal gravity vertical flows, slug flow breaks down into churn flow in which, in addition to normal disturbance waves, there are large waves of the flooding type (flow reversal). It is not until very high gas velocities are reached that the characteristics

disturbance wave region is firmly identified without the ambiguities associated with the occurrence of churn flow. Unfortunately, at such high gas velocities, the film on the wall becomes so thin that measurements in that region become very difficult to make. In microgravity, on the other hand, such instabilities do not exist.

1.7 LITERATURE SURVEY

In many situations involving annular flow, the characteristics of the flow are important for improving system performance or ensuing safety. A good understanding of liquid film behavior is critical to prevent dry-out situations and subsequent catastrophic events. The frictional pressure drop is important to properly size pumps and blowers. The frictional pressure drop in such a system is found to be much larger than for single-phase turbulent flow in a smooth pipe (Asali *et al.*, 1985), and the pressure drop of the gas phase can increase by orders of magnitude due to the presence of a liquid annulus (Brauner, 1991; Bousman, 1995).

1.7.1 Film Thickness

The general trend of the average film thickness values is for the mean film thickness to decrease with an increase in the gas flow rate or with a decrease in the liquid flow rates (Ariyadasa, 2002). Fukano and Furukawa (1998), and de Jong (1999) reported that the film thickness dependence on the gas mass flux is not linear but rather asymptotic, regardless of the magnitude of the liquid velocity. As the gas mass flux is increased, the average film thickness will decrease asymptotically to some minimum value, which may

be a function of the liquid mass flux, the tube diameter, the liquid density, and the interfacial surface tension. The mass flux of a phase is calculated from the mass flow rate divided by the channel's cross-sectional area,

$$G_p = \dot{m}_p / A. \tag{1-3}$$

For vertical upwards, co-current flow, this asymptotic behavior of the mean film thickness is partly due to the film becoming smoother as the gas flow rate increases (Ariyadasa, 2002). The rate of change of the film thickness decreases as the gas mass flux is increased above 35 kg/m^{2}s, at which point the disturbance waves become less random, indicating a change in the film. The film thickness is dominated by, and has an inverse relation to, the gas mass flux. On the other hand, increasing the liquid mass flux causes minimal changes in the film thickness. However, for vertical upwards, co-current flow, the film thickness does increase significantly between G_l of 120-161 kg/m^{2}s, where Re_{lo} becomes turbulent (Ariyadasa and Rezkallah, 2001). The liquid Reynolds number (assuming the liquid is flowing alone) is calculated by assuming the total mass flux as equal to the liquid phase, and is given by:

$$Re_{lo} = (G_l + G_g)\, d / \mu_l, \tag{1-4}$$

where G is the phase mass flux, d is the tube diameter and μ_l is the liquid viscosity.

Despite the dominance created by the gas mass flux, most film thickness correlations are based on the liquid flow rates. As an example, Henstock and Hanratty (1976) presented an empirical relationship for calculating the film thickness, based on the interfacial shear or the entrainment, as follows:

$$m^+ = [(0.707\, Re_{lf}^{0.5})^{2.5} + (0.0379\, Re_{lf}^{0.90})^{2.5}]^{0.4}, \tag{1-5}$$

where Re_{lf} is the liquid film Reynolds number, calculated by

$$Re_{lf} = 4\ G_{lf} / \mu_l\ , \tag{1-6}$$

where G_{lf} is the liquid film mass flux, calculated from the mass flow rate of the liquid film (per unit width of wall surface),

$$G_{lf} = \dot{m}_{lf} / (\pi\ d)\ . \tag{1-7}$$

The dimensionless film thickness, m^+, is given as

$$m^+ = \delta\ U_l^* / \nu_l, \tag{1-8}$$

where δ is the film thickness, ν_l is the liquid kinematic viscosity, and U_l^* is a liquid friction velocity, calculated from:

$$U_l^* = (\tau_i / \rho_l)^{0.5}\ , \tag{1-9}$$

where τ_i is the interfacial shear stress and ρ_l is the liquid density. Ambrosini *et al.* (1991) recommend using a slightly different correlation, given by:

$$m_l^+ = A\ Re_{lf}^B, \tag{1-10}$$

where A = 0.34, and B = 0.6 for $Re_{lf} < 1000$ (based on the work of Asali *et al.*, 1985), or A = 0.0512, and B = 0.875 for $Re_{lf} > 1000$ (based on the work of Kosky, 1971). For this correlation, the liquid friction velocity is calculated using a characteristic shear stress. These correlations are not very practical for design purposes since they require either knowledge or calculation of the entrainment (to calculate the liquid film mass flow rate) and the shear stress (for the friction velocity). Both quantities are not readily available from experimental work and must be calculated with further empirical or semi-empirical correlations. In addition, as mentioned earlier, these correlations do not identify the influence of the gas mass flow rate on the average film thickness.

One of the first correlations that included the effect of the gas flow rate on the mean film thickness was presented by Fukano and Furukawa (1998). The correlation was developed for vertical upwards flow, and was based on annular flow data collected using air-water and air-glycerin solutions in 19 mm and 26 mm tubes. The correlation, which is claimed to estimate the mean film thickness to within 15% for the entire range of data, is given as:

$$\delta / d = 0.0594 \ \exp(-0.34\ Fr_{go}^{0.25}\ Re_{sl}^{0.19}\ x^{0.6}), \tag{1-11}$$

where Fr_{go} is the gas Froude number, Re_{sl} is the superficial liquid Reynolds number, and x is the gas quality. The gas Froude number is calculated from:

$$Fr_{go} = V_{sg} / (g\ d)^{0.5}, \tag{1-12}$$

where g is the gravitational acceleration. The superficial liquid Reynolds number is calculated using:

$$Re_{sl} = V_{sl}\ d / \nu_l. \tag{1-13}$$

The gas quality is the ratio of the mass of the gas divided by the total mass (liquid plus gas), and from equation 1-1, can be calculated from:

$$x = \dot{m}_g / (\dot{m}_g + \dot{m}_l) = V_{sg}\ \rho_g / (V_{sg}\ \rho_g + V_{sl}\ \rho_l) \tag{1-14}$$

More recently, de Jong (1999) performed a dimensional analysis on microgravity annular flow data. The resultant correlation involves both liquid and gas terms, and is applicable to air-water, microgravity flows in small tubes (correlation was developed using data from a 9.5 mm tube). The correlation is given as:

$$\rho_l\ V_{sl}\ \delta / \mu_l = 0.0389\ Re_{sl}^{0.85}\ (x / (1-x))^{-0.42} \tag{1-15}$$

Despite the accepted influence of the gas mass flow rate, no other correlations could be found which directly include the gas effect on the average film thickness.

In addition to the influence of the gas and liquid flow rates, many researchers have investigated the effect of other flow parameters on the mean film thickness. Asali *et al.* (1985) reported that an increase in viscosity resulted in a thinner film. However, this has been contradicted by the work of Hori *et al.* (1979), and Fukano and Furukawa (1998), who reported that an increase in the liquid viscosity resulted in an increase in the film thickness. Bousman (1995) also concluded that an increase in either the viscosity or the surface tension resulted in a thicker liquid film and larger amplitude waves. However, the ratio of wave amplitude and mean film thickness was essentially independent of surface tension and liquid viscosity.

Willets (1987) stated that for constant mass flow rate (gas and liquid), the film thickness increased with an increase in the gas density. For the same gas velocity, the film thickness increased with decreasing the gas density. Both of these conclusions agree with the general trends of the film thickness. The mass flow rate (from equation 1-1) is dependant on both the density and the velocity, therefore an increase in gas density requires a decrease in the gas velocity in order to maintain a constant mass flow rate. As mentioned previously, a decrease in the gas velocity causes an increase in the film thickness. With a constant gas velocity, a decrease in the gas density causes the gas mass flow rate to decrease, which in turn results in a decrease in the film thickness. This result was based on comparing data between researchers with the tests taken at different absolute pressures, test section lengths and tube diameters. Willets' final conclusion, however, was that the relationship between the dimensionless film thickness and the liquid film Reynolds number appeared to be almost independent of the liquid viscosity, tube diameter and gas-to-liquid density ratio.

Along with the effect of the liquid viscosity, contradictory results were also found in the scarce work that has been conducted in microgravity environments. the correlation of Fukano and Furukawa (1998), equation 1-11, predicts a thinner film thickness due to a reduction in gravity, although their correlation is not applicable as the gravity level approaches zero. de Jong (1999) concluded that a reduction in gravity results in a thinner film. Without the influence of gravity, the liquid film is subjected to less body forces, and therefore has a higher average velocity. Based on the conservation of mass, a higher velocity causes a decrease in the flow area, which means a thinner mean film thickness. The reduction in the average film thickness with the reduction of gravity lessens as either the gas or liquid flow rates are increased or as the flow becomes more inertia dominated. However, Fujii *et al.* (1998) reported that the mean film thickness was larger in microgravity than that at normal gravity, but the maximum value was larger in normal gravity. The microgravity film thickness was reported to have been increased by two to five times, almost independent of the gas Reynolds number. This result was based on drop tower experiments taken over the range of Re_l between approximately 430 and 5800, and Re_g between approximately 4500 and 20 000. Rezkallah (1990), reporting on the work of Hill *et al.* (1987), stated that the microgravity annular liquid flow is thicker when compared to ground tests by approximately two-to-one. The inverse relationship between the level of gravity and the mean film thickness was explained as the result of lower shear, which causes less interfacial friction. These contradictory results suggest further study is required.

Many correlations relate both the film thickness and the frictional pressure drop. The measured pressure drop in annular flow is greater than if the gas were flowing alone in

the pipe, because the waves and ripples formed at the interface act as an increased roughness. The roughened interface causes the drag of the gas on the liquid to increase (Henstock and Hanratty, 1976). Rezkallah (1988) attributed the increase in pressure drop under microgravity conditions (especially at high qualities) to the increase in the film thickness. As the film thickness is decreased, the interfacial friction factor, f_i, is decreased, quite often with a linear dependence. At a lower limit of the film thickness, f_i is equal to the smooth pipe friction factor, f (Ambrosini *et al.*, 1991).

The triangular relationship (Whalley, 1987) relates the pressure gradient, the film flow rate and the film thickness, based on the assumption of a smooth interface and a laminar film flow. However, it does not accurately predict the experimental film thickness, most likely due to the large disturbance waves on the surface (Willets, 1987). The triangular relationship also does not take into account the effect of the gas, and moreover, it is a mathematical model, which does not account for any mass transfer.

Fukano and Furukawa (1998) related the interfacial friction factor to the film thickness, using the correlation:

$$f_i = 1.7\,(12 + \nu_l / \nu_w)^{-1.33}\,\{1 + 12\,(\delta / d)\}^{8}, \qquad (1\text{-}16)$$

where ν_w is the kinematic viscosity of water at 20°C, and (δ / d) is calculated from equation 1-11. Using equation 1-11 and 1-16, the frictional pressure drop can be calculated from:

$$-dP/dz_f = (f_i / 2d)\,(V_{sg}^{2} / (1 - 2(\delta / d))^{5})\,\rho_g. \qquad (1\text{-}17)$$

Based on these correlations, the film thickness, interfacial friction factor and frictional pressure drop can be calculated requiring only a knowledge of the tube diameter, and the gas and liquid viscosities, densities and superficial velocities.

1.7.2 Pressure Drop

The pressure drop is related to the amount of energy required to move the two-phase flow through the system. For liquid-liquid annular flow, the more viscous liquid forms the core, which results in a pressure reduction in the system. This pressure drop is comparable to that which would have been obtained with the less viscous fluid flowing alone in the pipe at the combined mixture velocity (Brauner, 1991). However, no reduction in the pressure is possible with the less viscous fluid flowing in the core. The extreme case is for gas-liquid annular flow, where the less viscous gas forms the core. If the core viscosity is five percent of the annulus viscosity, the pressure increase can be up to 100 times larger than the pressure of the core flowing alone (Brauner, 1991).

For gas-liquid annular flow, the pressure gradient reaches a minimum at approximately the transition between churn and annular flow (Barbosa *et al.*, 2002). As the void fraction is increased, the gas core velocity is increased, the film becomes thinner, and the pressure gradient increases (Vassallo *et al.*, 2001). Therefore, as the flow is pushed further into the annular regime, the pressure drop will increase. Bousman (1995) reported that the pressure drop increased with increasing the gas or liquid superficial velocities. Similar results were presented by de Jong (1999), who stated that an increase in the gas or liquid mass flux will increase the pressure drop almost linearly, and the

slope of increase is also a function of either the gas or liquid mass flux. Even the length of time the flow is in the annular regime can have an effect on the pressure gradient. Wolf *et al.* (2001) concluded that for low air fluxes, the pressure gradient reached a steady value after about 100 tube diameters, but it was still changing after 300 diameters at high air and water flow rates. In low-pressure systems, the pressure drop in the fully developed region can cause the gas density to increase, which can result in the gas accelerating (Laurinat *et al.*, 1984; Ishii and Mishima, 1989).

Correlations for predicting pressure drop can be either flow regime dependent or independent (Klausner *et al.*, 1991). It is prudent to develop correlations specific to each flow regime, because the momentum transport is dependant on the two-phase structure. Each two-phase flow structure has different momentum and frictional characteristics, which relates the flow regime and the pressure drop. Therefore, in order to accurately predict the two-phase pressure drop, a flow regime prediction and flow regime dependant models are needed (Chen *et al.*, 1991).

In addition to the dependence on the flow regime, the frictional pressure drop is primarily related to the properties of the liquid film (Laurinat *et al.*, 1984). Bousman (1995) reported that the pressure drop increases with an increase in the liquid viscosity, but was unaffected by the surface tension. Willets (1987) reported that the interfacial friction factor was affected by tube diameter, surface tension, liquid viscosity and gas-to-liquid density ratio. For constant gas and liquid mass flow rates, the pressure gradient increased with decreasing the gas density, presumably due to the gas velocity increase. Willets (1987) also concluded that the interfacial friction factor was proportional to the

square root of the gas-to-liquid density ratio. However, this was multiplied by different constants for the different gas densities. These results, obtained using air and helium, suggested that there is an effect of density ratio on interfacial friction factor correlations that are used to correlate the friction factor against film thickness. However, further studies are necessary to establish this effect.

Based on the variety of properties that influence the pressure drop, many correlations have been proposed. Using two-phase flows of air and various liquids, Lockart and Martinelli (1949) presented the relationship between the single-phase pressure drop and the two-phase pressure drop by using a two-phase multiplier. The two-phase multiplier, Φ^2, is defined as the ratio between the two-phase pressure drop and the single phase pressure drop and is used to multiply the single-phase pressure drop (gas or liquid) to get the two-phase frictional pressure gradient, $dP/dz_{2\text{-}\Phi,f}$:

$$-dP/dz_{2\text{-}\Phi,f} = (-dP/dz)_{g,f}\, \Phi^2_g \,, \tag{1-18}$$

where $dP/dz_{g,f}$ is the gas phase frictional pressure gradient, and Φ^2_g is the gas two-phase multiplier. The single-phase frictional pressure gradient is calculated from the Darcy-Weisbach equation:

$$dP/dz_{p,f} = \Delta P / L = f\, \rho_p\, V_p^2 / (2\, d), \tag{1-19}$$

where ΔP is the pressure drop, L is the length and f is the Darcy friction factor calculated using the Moody chart (White, 1994). Chisholm (1973) approximated the Lockart-Martinelli correlation by:

$$\Phi^2_g = 1 + C\, X + X^2. \tag{1-20}$$

C is a constant dependant on the gas and liquid flows, (for turbulent gas and turbulent liquid flows, the value is 20), and X^2 is the ratio of the single-phase frictional pressure drops:

$$X^2 = (dP/dz_{l,f}) / (dP/dz_{g,f}). \quad (1\text{-}21)$$

Combining equations 1-18, 1-20 and 1-21 gives the relationship for the two-phase pressure drop:

$$(-dP/dz)_{2\text{-}\Phi,f} = (-dP/dz)_g + C\,[(-dP/dz)_g\,(-dP/dz)_l]^{0.5} + (-dP/dz)_l. \quad (1\text{-}22)$$

Although this correlation is simple, it is not very accurate. Bousman (1995) reported that the Lockart-Martinelli-Chisholm model can predict the annular flow pressure drop with about ± 20% accuracy. However, Whalley (1996) stated that even the best generally available correlations can result in root-mean-square errors on the order of 40%.

The empirical model of Fu and Klausner (1997) can predict the majority of the measured pressure drop data to within ± 25%. This pressure drop prediction, based on data for vertical up flow, down flow and microgravity, has a slightly better mean deviation for up flow, but a slightly worse mean deviation for microgravity flow when compared to the Chisholm correlation. However, the model requires knowledge of the interfacial shear stress, the entrainment, and the rate of entrainment, so it is not very practical for design purposes. Similar knowledge is required for the correlation presented by Henstock and Hanratty (1976), who stated that the prediction for upward flow gives a lot of scatter. However, they did note that there was no influence of the gas Reynolds number on the friction factor.

Similar to the dimensional analysis work performed for the average film thickness, de Jong (1999) reported a correlation for the frictional pressure drop, applicable to microgravity air-water flows in small tubes. The correlation includes both the gas and liquid properties, and is given by:

$$Eu = 4436\ Re_{sl}^{-0.33}\ (x / (1-x))^{0.80}\ (\rho_g / \rho_l)^{0.5}\ (\mu_g / \mu_l)^{0.1}, \quad (1\text{-}23)$$

where Eu is the Euler number, the ratio of the pressure force to the inertia force, given as:

$$Eu = (dP / dz)\ (d / (\rho_l\ V_{sl}^2)). \quad (1\text{-}24)$$

This work did not explore the effects of the gas and liquid densities and viscosities. Therefore, the exponents on the density and viscosity ratios were taken from the work of Lockart and Martinelli (1949), even though the power on the quality term was different. This correlation predicts the microgravity experimental pressure drop generally to within ± 10%.

As with the average film thickness, the influence of gravity on the frictional pressure drop is varied across the literature. Chen *et al.* (1991) concluded that the pressure drop in reduced gravity is approximately two times larger than that for normal gravity. However, this difference can be due to the difference in the flow regimes. The microgravity data were mostly annular, while the normal gravity data (horizontal flow) were wavy-stratified and slug flow. By their own admission, the pressure drop is dependant on the flow regime. Heppner *et al.* (1975) also reported a higher pressure drop in microgravity compared to normal gravity, but once again the flow was horizontal for the normal gravity case. The pressure drop data were not reported for

their hypergravity tests. Rezkallah (1988) reported that the microgravity pressure drop was approximately 20% higher than the normal gravity data. However, this is contrary to the work of Sridar *et al.* (1992), who concluded that the frictional pressure drop in microgravity was lower than that for normal gravity.

For vertical flows, the pressure drop tends to increase in the presence of a gravity field due to the buoyancy effect. The relative velocity between the gas and the liquid is increased, causing an increase in the interfacial shear stress, which in turn causes an increase in the pressure drop.

Bousman (1995) reported that the Lockart-Martinelli-Chisholm correlation, which is accurate to ± 20% for normal gravity, gave the same accuracy for the prediction of the microgravity pressure drop. This is not in agreement with de Jong (1999), who reported that the same correlation under-predicted the pressure drop in microgravity annular flow (but it is improved if the flow is treated as turbulent-turbulent). de Jong (1999) also concluded that the frictional pressure drop was not largely affected by the presence of gravity, however, the rate of increase of the pressure drop changed with the presence of gravity. As the gas or liquid mass flux was increased, the frictional pressure drop was increased more in the normal gravity cases when compared to the microgravity results. Ariyadasa (2002) stated that the pressure drop is basically unaffected by the change in the gravity direction (from vertical upwards to vertical downwards for air-water co-current flows), and there is little effect due to gravity on the frictional pressure drop for gas mass fluxes above 35 kg / (m^2*s).

1.7.3 Other Characteristics

The film thickness and pressure drop are also influenced by the entrainment rate and the disturbance waves. The entrainment rate is the rate at which liquid droplets leave the film and become transported by the gas phase. Knowledge of the entrainment fraction and the amount of the liquid flowing as a liquid film is needed to develop better design procedures for vertical annular gas-liquid flows (Asali *et al.*, 1985). The entrainment rate of the droplets from the liquid film is also the greatest uncertainty in the mass balance of the liquid film (Lopez de Bertodano *et al.*, 2001).

At large gas velocities, the critical liquid film Reynolds number for the creation of disturbance waves is independent, or a weak function of, the gas velocity, pipe diameter, gas density and liquid viscosity. The ripple regime can be identified with a limiting value of the liquid film Reynolds number of approximately 300 (Asali *et al.*, 1985). Azzopardi (1986) stated that the frequency of disturbance waves increased with increasing gas density (for a given gas velocity), and the disturbance wave velocity decreased with the gas density to a power of about 0.3.

The gas-to-liquid density ratio (ρ_g / ρ_l) is also observed to affect the size of entrained droplets. Ambrosini *et al.* (1991) reported the power on the density ratio for the drop size to be 0.56, while Jepson *et al.* (1989) concluded that the drop size increased with the gas density to the power 0.1. The drop concentrations were reported to be lower for helium-water flow compared to air-water flow and the deposition coefficients were slightly higher. However, Willets (1987) stated that the deposition coefficient was

essentially independent of the gas density. The deposition coefficient represents the opposite process of entrainment, where the liquid droplets in the gas core are deposited back in the liquid film. A reduction in the gas density caused a lower shear on the liquid film, which caused a decrease in the amount of entrainment (Jepson *et al.*, 1989). Pan and Hanratty (2002) stated that this relationship was based on the density to a power of 0.25. Lopez de Bertodano *et al.* (2001) concluded that the entrainment rate was dependent on the liquid-to-gas density ratio to a power of 0.5, and Vassallo *et al.* (2001) stated that the entrainment rate was enhanced at higher pressures due to the higher gas density.

Although there have been many studies with varying fluids, the effect of the varying the gas properties is not fully understood and is often contradictory. The accuracy of multiphase design and predictive tools is poor compared to single-phase systems (Keshock and Lin, 1996). By understanding the effects of both fluids, two-phase systems may be able to be optimized by choosing the gas-liquid combination. As well, two-phase flow studies occurring in a microgravity environment have increased, but very little studies have been conducted at other gravitational levels. Even among the microgravity research, the amount of data is limited for annular flows (Fujii *et al.*, 1998) and is often contradictory.

1.8 OBJECTIVES

Based on the above noted discrepancies in the annular flow results, the objectives of the present research are as follows:

1. To examine the effect of the gravitational acceleration on average film thickness,
2. To examine the effect of the gravitational acceleration average frictional pressure drop,
3. To examine the effect of the gas density on average film thickness, and
4. To examine the effect of the gas density on average frictional pressure drop.

Objectives 1 and 2 will be accomplished by studying annular flow in reduced, normal, and increased gravity fields. Objectives 3 and 4 will be accomplished by studying air-water and helium-water annular flow at matching conditions. All flows being studied will be vertical-upwards, co-current annular flow in a 9.525 mm tube.

2.0 EXPERIMENTAL FACILITIES

The following sections give a detailed description of the two-phase flow loop, the general instrumentation used for data collection, and the flight campaigns.

The two-phase flow loop apparatus was built at the University of Saskatchewan and was designed to fit inside the NASA KC-135 microgravity aircraft. Previous microgravity data have been collected using the apparatus by Huckerby (1992), Elkow (1995), Rite (1995), and Lowe (1997), and also reported by de Jong (1999) and Zhu (2004). With some modifications, it was able to fit inside the ESA A300 microgravity aircraft for the flight campaigns discussed here. The same experimental apparatus was used for the present data collection during both flight and ground tests.

2.1 TWO-PHASE FLOW LOOP APPARATUS

The two-phase flow loop apparatus is shown in Figure 2.1a, with a schematic shown in Figure 2.1b. The flow loop includes a circulating liquid loop, an open gas loop, and a computer based data acquisition and control system.

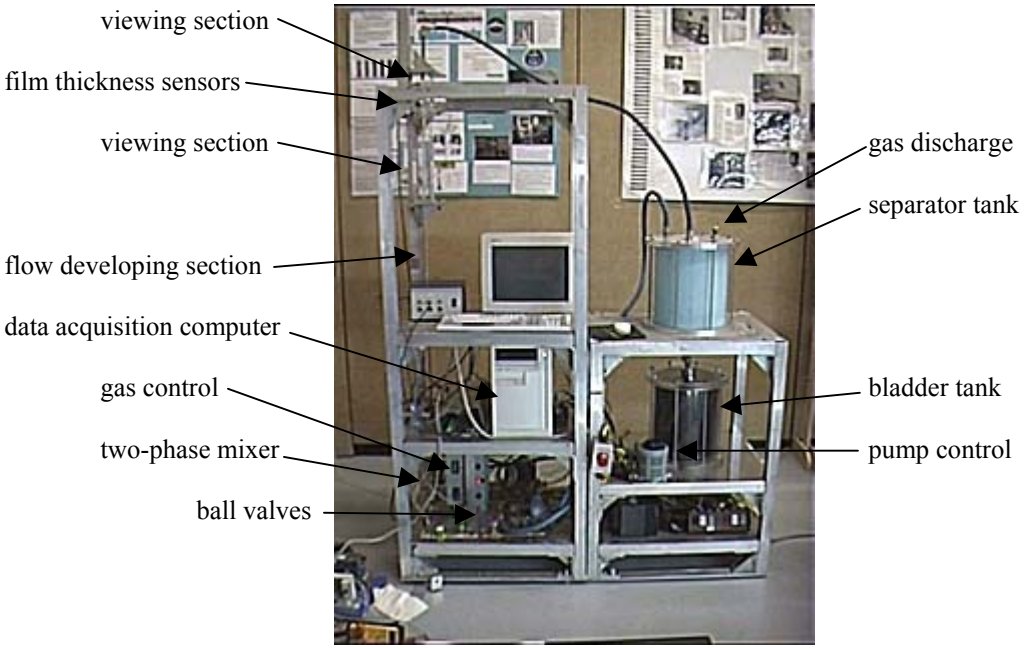

Figure 2.1a. Flight loop apparatus.

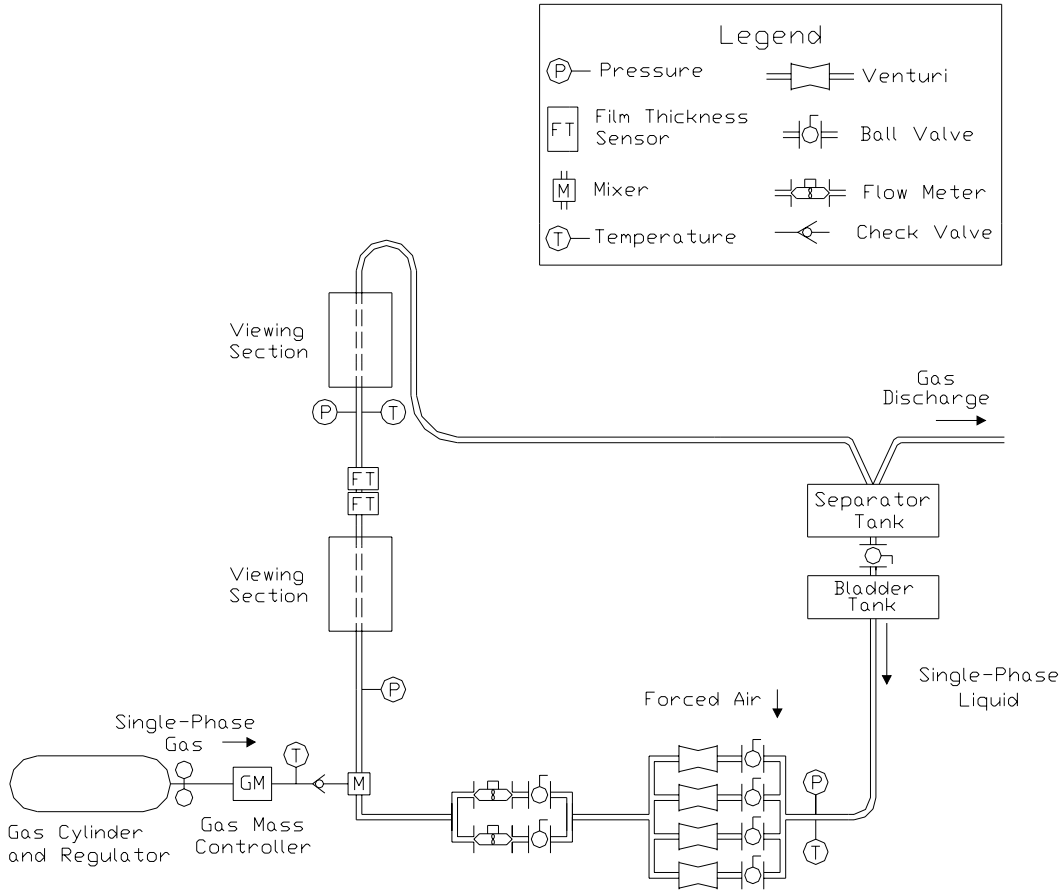

Figure 2.1b. Schematic of the flight apparatus.

2.1.1 Liquid Loop

The liquid loop of the flow apparatus consists of a collapsible bladder tank, a gear pump, a by-pass line with a check-valve, a reference film thickness probe, four flow venturies, an in-line filter, two turbine flow meters, a gas-liquid mixer, a vertical developing length, an acrylic viewing section, a pair of two-wire conductance film thickness probes, a second viewing section, and a separator tank.

The collapsible bladder tank is used to provide a positive pressure on the liquid during the microgravity duration of the flight. A variable speed DC motor is used to drive a positive displacement gear pump. The flow then passes through a tee section with one line leading to a check valve and a by-pass line to prevent excessive pressures in the system. On the other line, a film thickness sensor is installed to take reading for single-phase flow at the inlet conditions (reference conditions). The system pressure is measured using a 414 kPa (60 psi) gauge pressure transducer, and temperature is measured with a Type T (Copper-Constantine) thermocouple. The flow then passes through a heat exchanger with forced-air cooling, and then through a set of four different cavitating venturies or another by-pass line. The venturies and the by-pass line are adjusted to give the desired flow rate and to allow the pump speed to be increased while maintaining a constant flow rate, even at low liquid flow rates.

The liquid then passes through a 15-micron stainless steel filter to remove any particles prior to entering one of the two manually selectable turbine flow meters. The flow meters have a range of 0.1-2 LPM. The flow then enters axially into the mixer while the

gas is injected peripherally from the supply line. A similar mixture method was used by Colin *et al.* (1991). This method of gas-liquid mixing is used to simulate the boiling process, where the bubbles would form on the surface of the tube wall and then be carried away from the wall by the incoming liquid phase.

The two-phase mixture then enters into a 9.525 mm (3/8") ID stainless steel tube and is allowed to develop over a length of 0.72 m (76d), to where the first pressure tap is located. The second pressure tap is separated from the first by 0.88 m (92d). The differential pressure between the two taps is measured using a +/- 13.8 kPa (2 psi) differential, diaphragm type pressure transducer. The first film thickness probe is located 1.44 m (151d) downstream from the mixer, and the second film thickness probe is another 0.019 m (2d) downstream. The system pressure and temperature are measured at the second pressure tap using a 345 kPa (50 psi) absolute pressure transducer and a Type T thermocouple located flush with the tube inner wall. Digital images of the flow are recorded through a solid acrylic viewing block using a 30 frame per second digital video camera, located 0.13 m (14d) downstream of the second film thickness probe.

The two-phase flow then enters into a separator tank. The separator tank includes material that traps water by surface tension to separate the two phases during the microgravity periods. During the hypergravity portion of the parabola, or during ground testing, the liquid is forced by gravity drainage back into the bladder tank for recirculation.

2.1.2 Gas Loop

The gas loop of the apparatus consists of a cylinder of compressed gas (either air or helium), a pressure regulator, a gas flow controller, and a check valve. The compressed gas is supplied from 50 L cylinders at a pressure of 18 Mpa (2600 psi). A pressure regulator is used to reduce the outlet pressure to approximately 500 Kpa (72 psi), prior to the gas entering the mass flow controller. The gas mass flow rate is computer controlled using a 200 standard litres per minute (SLM) gas mass controller. The output of the gas controller is factory set to reference the mass of nitrogen at 0^{o}C and 760 mm Hg (101.325 kPa), to give a standard litre. The check valve is located between the gas-liquid mixer and the gas mass controller to prevent any liquid from flowing back into the gas flow controller. The gas is injected peripherally into the liquid through the mixing chamber, and flows as the two-phase mixture through the test section. After being separated from the water in the separator tank, it is vented overboard the airplane during flights, or vented to the surroundings during ground testing.

2.1.3 Film Thickness Sensors

The liquid film is measured using a two-wire conductance probe. The film thickness probes are shown in Figure 2.2, and a cross-sectional view is shown in Figure 2.3. The experimental apparatus contains three probes; one is located in the single-phase water line and the other two are mounted in the test section. Response of the film thickness probes varies with conductivity (Azzopardi and Whalley, 1980) therefore, the single-phase probe is used as a reference to account for the variations due to changes in the water conductivity or temperature. The two other probes are used to measure the film

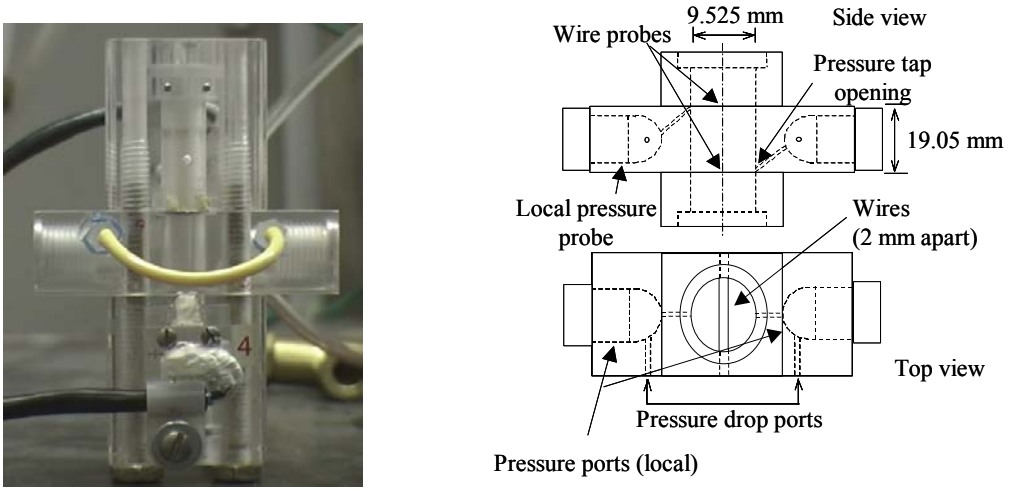

Figure 2.2. Film thickness probe photo and schematic.

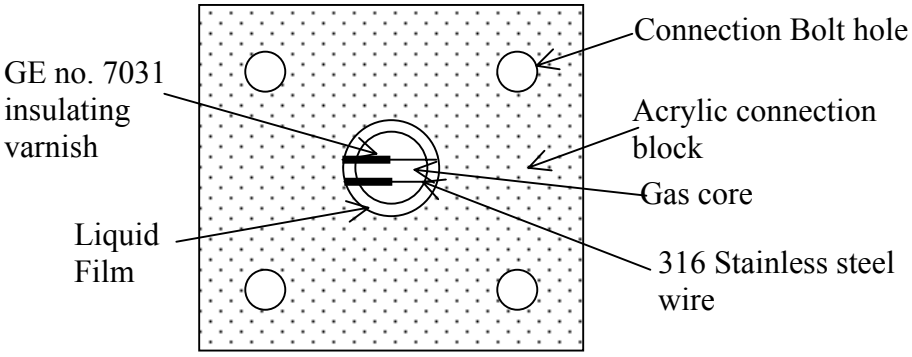

Figure 2.3. Cross-sectional view of a film thickness probe (de Jong, 1999).

thickness in the vertical tube. Two probes are used to be able to correlate the velocity of the passing waves.

The film thickness probes were designed and built at the University of Saskatchewan. The principle of operation is based on measuring the electrical conductivity across the two-phase mixture to determine the relative amounts of gas and liquid. Water has a greater conductivity than either air or helium, and hence the amount of water in the tube can be determined from the conductivity measurement across the two wires. The wires are made from 0.04064 mm (0.0016 inch) stainless steel wire, stretched across the

diameter of the tube and separated by a distance of 2 mm. Because of symmetry, measurements need only to be taken over half of the tube cross-section. Half of the wire is coated with an insulating varnish (GE no. 7031), thinned with a 50%-50% solution of Xylene and Methanol. Further details on the electronic operation of the film thickness sensors can be found in de Jong (1999).

2.1.4 Data Acquisition and Control System

The data acquisition and control system is a computer-based system. All controls are done through a LabVIEW© program, which was developed for the flight experiments by the author. The pump speed is controlled manually by adjusting a variable AC power source.

The control program prompts the user for the location of the calibration file, then reads the calibration data and reinitializes the displays. The input board is scanned continuously at the specified rate and the data are stored into a buffer. The storage buffer is also read at a specified rate and the input voltages are processed using the calibration data. All the converted data are then displayed on the screen in the form of both graphs and digital displays. The program then checks the control icons and implements any changes before reading the next set in the buffer. The controls in the program include the gas mass flow rate, the pump main-power switch, the parabola number, and the data logging. When the data logging is turned on, the program saves the information to a file specified by the parabola number. The time, date, frequency,

channel name and units, and the processed data are printed to the file until the data logging is turned off.

Flow measurements include reference temperature, gas flow rate, pump speed, single-phase water pressure and temperature, film thickness readings from the three probes, liquid flow rate, pressure drops across the pressure taps, pressure drop between the two film thickness probes located in the test section, the two-phase absolute pressure and temperature, and the acceleration levels. The calibration equations for all equipment can be found in Appendix A. A 12-bit analog output board is used for control and a 12-bit input board is used for the data acquisition. Both the input and output boards are connected to terminal blocks. Data were collected at a sampling rate of 1024 Hz. Data supplied by the aircraft pilots (after each flight) include: time, x, y, z acceleration levels, and the cabin temperature and pressure for each parabola.

2.1.5 System Hardware

Modular type platforms are used to house the two-phase flow experiment on board the A300 Zero-G Airbus. The frame was designed and constructed at the University of Saskatchewan (Durand *et al.*, 1990). The modular design of the experiment platform consists of two separate platforms that can be attached vertically, side-by-side, or used as two stand alone modules. The side-by-side configuration was used for the flights, as shown in Figure 2.4. The overall dimensions of the frame (when connected together) are a depth of 0.56 m, a width of 1.40 m, and a height of 1.84 m. The right side has a height of 1.35 m.

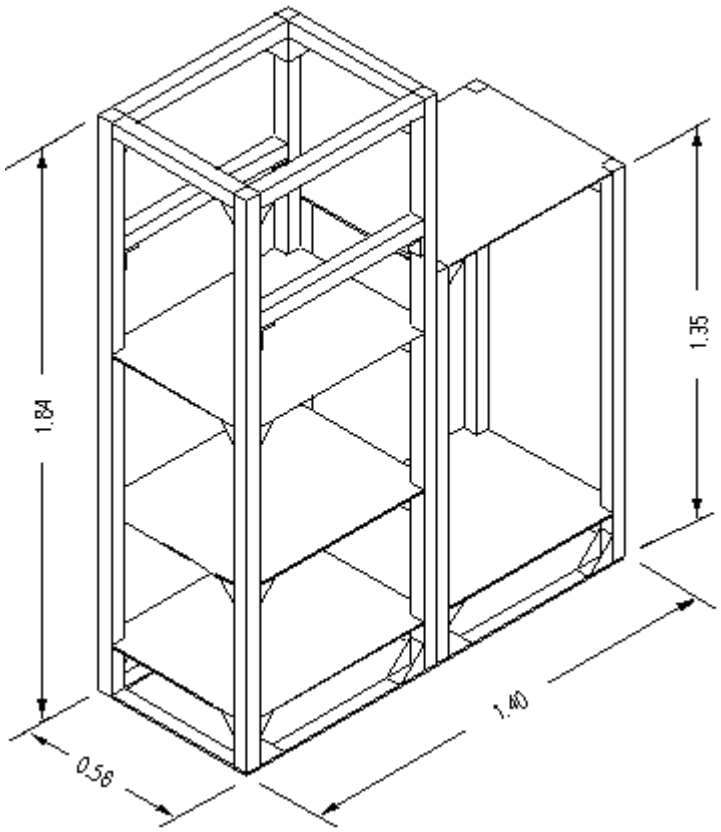

Figure 2.4. A schematic of the flight loop test frame (Dimensions in meters).

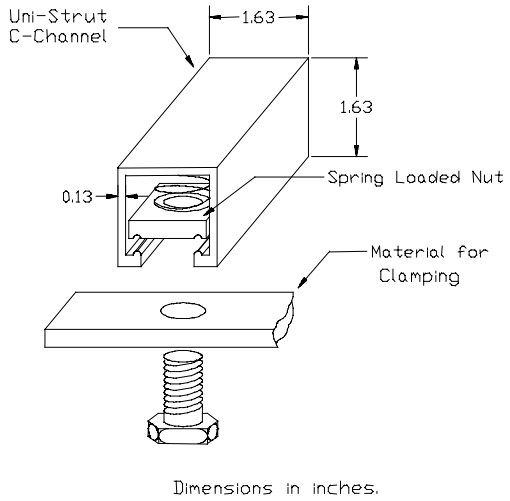

Figure 2.5. UNISTRUT© connection system.

The frame is connected together using the UNISTRUT© connection system, as shown in Figure 2.5. This type of frame allows for easy adjustment of the levels within each module. It also facilitates the attachment of auxiliary components such as cameras, lamps and sensors. The bottom supports are bolted to the aircraft floor.

2.1.6 Electrical Components

In order to be able to run the equipment in Europe, a transformer was required. A safety isolating transformer is used to reduce the 220 VAC, 50 Hz supply to the required 110 VAC, 50 Hz for use by all electrical components. A large, emergency push button shut-off switch and a 10 amp fuse are located on the input side of the transformer. The outlet is connected to a standard power bar. For ground testing at the University of Saskatchewan, the power bar is connected directly to a 110 VAC, 60 Hz source.

An 11.3 VDC electric motor drawing 4.8 amps drives the pump. The motor uses rectified AC power. The 110 VAC current is passed through a Fisher-Scientific variable transformer rated for a maximum current of 10 amps. This transformer allows the speed of the pump to be controlled by manually varying the voltage. Upon leaving the transformer, the alternating current is sent through a rectifier and a 1000 μF capacitor to provide a DC current to the motor.

2.2 Microgravity Platform

The microgravity and hypergravity data were collected on board the European Space Agency parabolic aircraft (Airbus A300; operated by Novespace) during the 29th and 30th ESA Microgravity Science Missions. Both parabolic flight campaigns were operated by Novespace, in Bordeaux, France. The first campaign was held during the week of November 20-24, 2000, and the second during the week of May 14-18, 2001.

2.2.1 Microgravity Aircraft

The Airbus A300 is the largest parabolic aircraft in the world having a test area 20 m long, 5 m wide, and 2.3 m high. The door to the testing area is 1.93 m high and 1.07 m wide (Novespace, 1999). The size of the aircraft allows 10 to 15 different experiments to be conducted concurrently. However, the size also prevents some residual acceleration levels (due to the vibration of the aircraft) from being eliminated. A typical parabolic maneuver and the cabin announcement messages during a parabola are shown schematically in Figure 2.6. Each parabola is preceded by approximately one minute of level flying. The parabola begins with the hypergravity portion, where acceleration levels are approximately 1.8-g_o for 15 seconds, followed by 5 seconds of approximately 1.5-g_o. A transition period of approximately 5 seconds occurs as the microgravity period is approached. The microgravity period lasts about 22 seconds during which time the pilots maintain the acceleration level between +/- 0.05-g_o. The recovery portion of the parabola mirrors the entry portion with 5 seconds of transition, 5 seconds of 1.5-g_o, followed by 15 seconds of 1.8-g_o. The parabola ends with approximately 30 seconds of

level flight before the next parabola sequence is started. Thirty-one parabolas are flown each day, with a normal campaign schedule of three flight days (a total of 93 parabolas). The first parabola is intended as a "warm-up" for both the pilots and the experimenters. Afterwards, the parabolas are flown as above with longer breaks after every fifth parabola, as shown in Figure 2.7. The gravity signal during the data collection period of a typical parabola, as collected by the experimental apparatus, is shown in Figure 2.8.

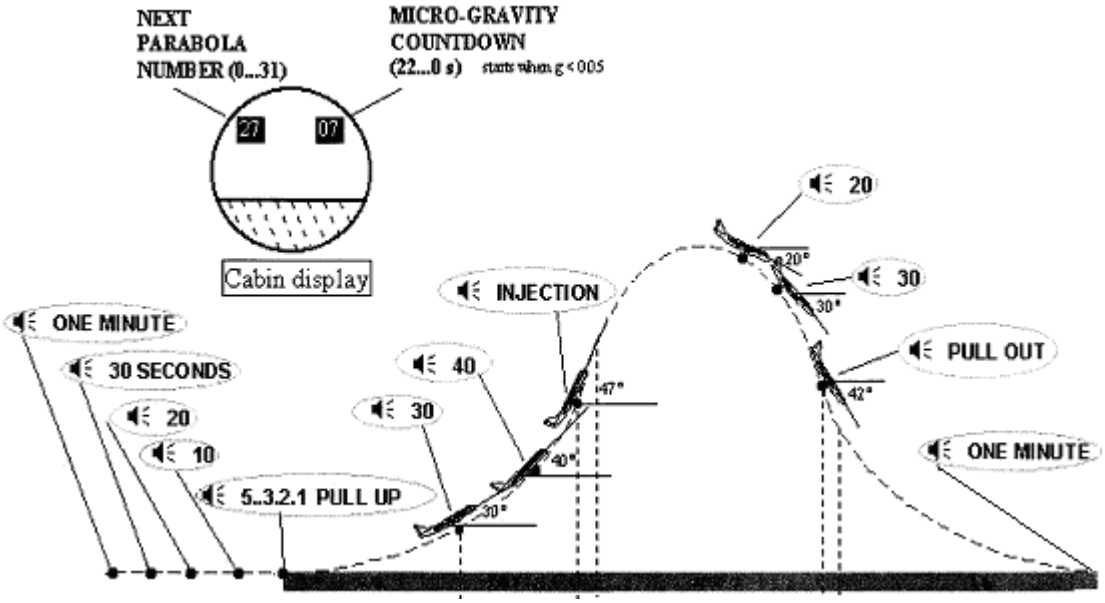

Figure 2.6. Typical Airbus A300 parabolic flight maneuver with cabin announcements. (Novespace, 1999)

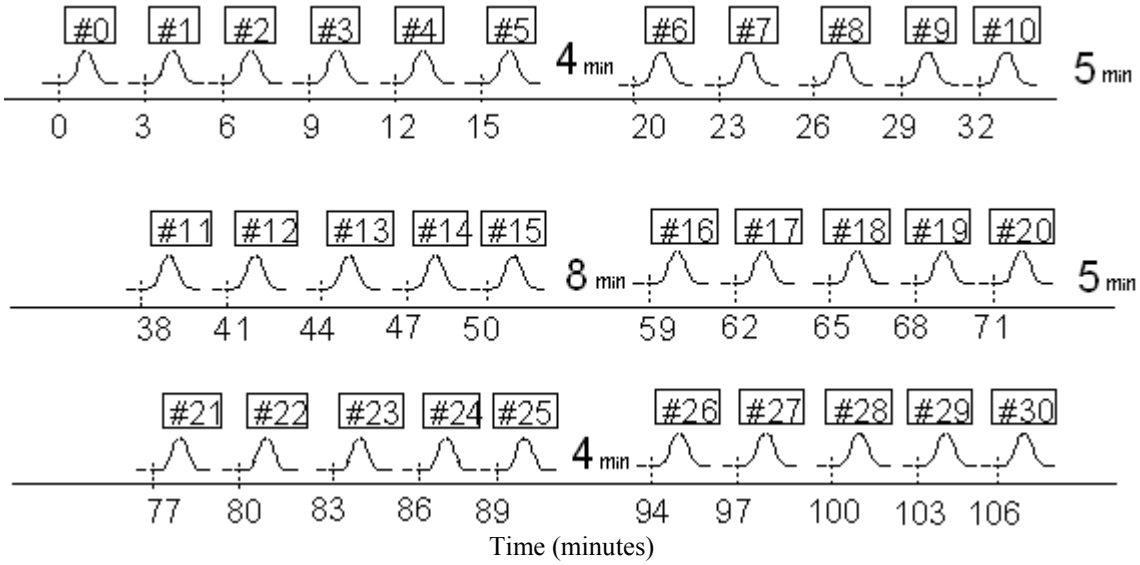

Figure 2.7. Typical parabolic sequence of the Airbus A300 microgravity flight campaign. (Noevespace, 1999)

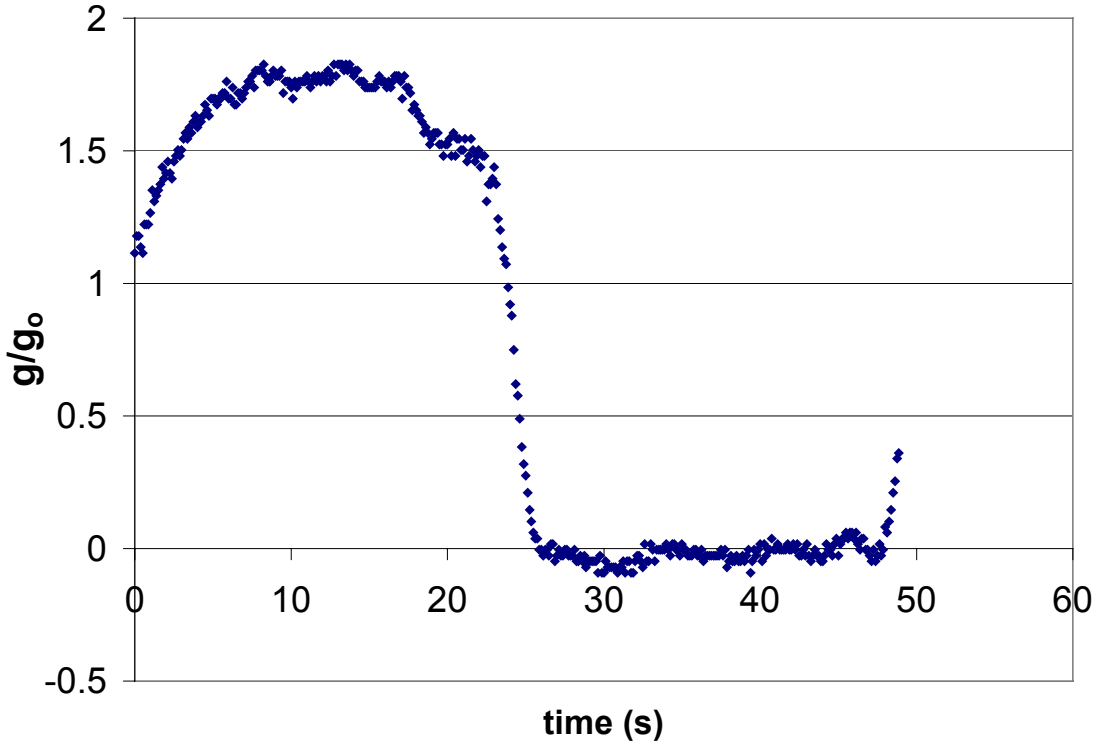

Figure 2.8. Gravity signal during data collection period of a typical parabola.

3.0 PROCEDURE AND DATA ANALYSIS

Initially, the air-water set points were selected to match the mass flow rates of the liquid and gas set points achieved in upward flow by Ariyadasa (2002). Due to the smaller size of the flight loop apparatus, the system pressure was lower, allowing lower liquid and higher gas flow rates than could be achieved on the ground apparatus. This corresponds to pushing further into the annular flow regime. The helium-water set points were then selected to match the specific energy of the gas phase and the same liquid mass flow rate. The following sections summarize the test matrix and the flight test procedure that was adopted for the ESA Airbus microgravity flight campaigns.

3.1 TEST MATRIX

In order to examine the effect of the gas density, annular set points were chosen with air-water and were then repeated using helium-water. The helium set points were chosen by matching the superficial liquid velocity and the standard gas flow rate (November 2000), or by matching the superficial liquid velocity and the gas specific energy (May 2001). The gas specific energy is given by:

$$\rho_g V_{sg}^2, \tag{3-1}$$

where ρ_g is the gas density, and V_{sg} is the gas superficial velocity. The specific energy was chosen as the basis of comparison because this term appears in a couple of relevant

non-dimensional terms, the Weber number and the Euler number. All of the ground set points were chosen to match the mass flow rates achieved during the flight campaign. The ranges of superficial liquid and gas velocities achieved for air-water and helium-water are shown in Table 3.1. The set points for helium-water (matching $\rho_g V_{sg}^2$) are at a much higher gas velocity due to the low density of helium.

Table 3.1. Range of achieved liquid and gas superficial velocities.

	Microgravity	**Hypergravity**	**Normal gravity**
Air-water	Vsl: 0.093 – 0.314 m/s Vsg: 18.2 – 37.0 m/s	Vsl: 0.075 – 0.314 m/s Vsg: 14.2 – 36.7 m/s	Vsl: 0.076 – 0.315 m/s Vsg: 13.0 – 29.4 m/s
Helium-water	Vsl: 0.102 – 0.299 m/s Vsg: 32.0 – 77.4 m/s	Vsl: 0.099 – 0.310 m/s Vsg: 22.2 – 78.8 m/s	Vsl: 0.098 – 0.312 m/s Vsg: 22.2 – 62.4 m/s

In order to examine the effect of the gravitational acceleration on the annular flow, the same set points were maintained for the hypergravity and microgravity portions of the parabolic flight, and repeated during ground testing. This allows the same data to be examined at 1-g_o, (normal gravity), +/- 0.05-g_o (microgravity), and 1.8-g_o (hypergravity).

3.2 Data Collection Procedure

The procedure followed during a flight campaign is described below:

1) Equipment is removed from the shipping crates and mounted to the frame in the appropriate positions.
2) Inspection and leak tests are performed to verify tight connections and correct operation of the equipment.

3) The apparatus is then partially disassembled and loaded onto the aircraft. (The two modules of the experiment are separated in order to fit through the aircraft cargo doors.)
4) The apparatus is then bolted to the aircraft floor and the two sides are reconnected.
5) The gas cylinders for the first flight are loaded and secured inside a special rack mounted to the floor of the aircraft.
6) The set-up and commissioning procedure is then continued to verify correct operation and the power and vent lines are connected.
7) The bladder tank is filled with approximately 15 L of low conductivity water (<7 μS/cm), which is required to match the calibration condition of the film thickness probes.
8) A data file is recorded with no flow to establish the zero points for many of the instruments.
9) Single-phase water is then circulated in the loop at high pressure for test for leaks and to verify proper operation as per the flight crew requirements. During this time, any air in the pressure transducer lines is bled out. This is to avoid any pressure reading problems associated with the compressibility of air in the lines.
10) Prior to take-off, the equipment is left in the "on" position to ensure sufficient warm-up time for all electronic instruments.
11) Power to the experiments is usually turned off approximately 30 minutes prior to take-off and is later restored during level flight approaching the flight airspace.
12) When the power is restored, the outlet of the pressure regulator is set to the desired pressure of approximately 500 kPa, and the pump is started in order to set the liquid

flow rate for the first series of tests. A videocassette is loaded into the digital camera and recording is started.

13) For the warm-up parabola, only water is circulated in the system. This is to establish a microgravity and hypergravity reference point for the data.

14) During the period of level flying between parabolas (approximately 1.5 minutes), the gas flow rate is adjusted to the desired point and the liquid flow rate is further adjusted, if necessary.

15) The data logging is typically started between 3 and 10 seconds prior to the "Pull-up" announcement and data is logged until the "Pull-out" announcement. This allows the hypergravity and microgravity data to be recorded in the same file and with the same parameters.

The longer breaks between every fifth parabola are used to adjust the liquid flow rate and to take single-phase water readings. If time permits, the camera and gas pressure are checked and, if necessary, the gas cylinder is changed.

After the parabolas are complete, the equipment is shut off in order to prepare for landing. Upon landing, the empty gas cylinders are replaced with full ones and the conductivity of the water is verified to be in the correct range. During the November 2000 campaign, the water was drained out due to the possibility of freezing overnight and was refilled the next morning. After each flight campaign, the equipment was disassembled and repacked for the return trip to Canada.

The data collection procedure for the ground testing was similar to the flight procedure. The equipment was uncrated and reassembled. Leak tests were performed to verify correct operation, and the system was filled with the low conductivity water. Reference files with no water and all water flow were recorded. The gas and liquid flow rates were set to the desired values to match the flight set points. When the flow rates become stable, a data file and the digital video are recorded for approximately ten seconds. The flow rates are then adjusted for the next point. All-water reference files are recorded after approximately every ten two-phase files.

3.3 Data Selection

The main data obtained during the parabolic flights (for this work) include the liquid and gas flow rates, the two-phase pressure drop across the test section and the two film thickness readings. These parameters are collected during both the microgravity and hypergravity portions of the flights. Since aircraft vibrations and gravity fluctuations affect the flow rates, only those portions of the data where gravity settles at approximately 1.75-g_o or +/- 0.05-g_o are used. The criteria for establishing the usable portion of a parabola are summarized in Table 3.2.

Table 3.2. Flight data selection criteria.

Parameter	Criteria
V_{sl}	Max fluctuation: +/- 7% of average
$\dot{m}_g$	Max fluctuation: +/- 1% of average
Microgravity data	3 seconds after reaching +/- 0.05-g_o
Hypergravity data	2 seconds after reaching 1.75-g_o
File size	4 seconds long

The criteria for the gas and liquid flow rates are based on previous microgravity data and represent the maximum allowable fluctuation from the average value. Therefore, all of the data must fall within 0.93 and 1.07 times the average value for the liquid flow rate, or 0.99 to 1.01 times the average value for the gas flow rate. The time delays for choosing the microgravity and hypergravity data are based on the time for the flow to overcome the disturbances due to the change in gravity (Rite, 1995). The 2-g portions of the parabolas and the quick change in the gravitational fields before and after each reduced gravity portion can induce undesired system transients (Zhao *et al.*, 2001). However, the flow patterns and flow characteristics in microgravity appear to reach equilibrium after the first 1.2s after the pullout from the hypergravity conditions (Dukler *et al.,* 1988; Chen *et al.,* 1991). If a four-second data collection window cannot be found in the data, a two-second window that satisfies all the other criteria is selected. If a two-second window cannot be found, the parabola is ignored.

The same data selection criteria are used for selecting the windows of the ground data. However, without the vibrations of the aircraft, the ground data set points are much more stable, and quite often, the entire ten-second data file fits the criteria.

3.4 Data Analysis

Once an appropriate window of data is found, the remaining analysis can take place. The minimum, maximum, average, and standard deviation values are calculated of the 4096 data points (for a four-second window) for each different instrument reading in the data file. The minimum and maximum values of the flow rates are verified to see if they

fall within the data selection criteria. All further analysis is done using the calculated average values, except the film thickness calculations.

3.4.1 Film Thickness Calculation

The output of the film thickness sensors is a voltage proportional to the relative amounts of water and gas in the tube. Similar to the work of Lowe (1997), the film thickness calibration is best when the output voltage is normalized. This is to account for changes in the water conductivity. The normalization equation is:

$$V^* = \frac{V - V_a}{V_w - V_a}, \tag{3-2}$$

where V* is the normalized voltage, V is the two-phase voltage recorded by the film thickness sensor, V_a is the all-air voltage reading, and V_w is the all-water voltage reading. The all-air readings are taken when the system is completely dry, and the all-water readings are taken when only water is flowing in the experimental loop. The normalized voltage is then applied to the calibration equation for the sensor, to convert to the film thickness measurements in millimeters. The minimum, maximum, average and standard deviation are then calculated using the calculated film thickness measurements.

3.4.2 Pressure Drop Calculation

The total pressure drop of a fluid system can be represented as the sum of three pressure components. These are the gravitational, frictional, and accelerational pressure-drops:

$$\left(\frac{dP}{dz}\right)_{total} = \left(\frac{dP}{dz}\right)_{gravitational} + \left(\frac{dP}{dz}\right)_{frictional} + \left(\frac{dP}{dz}\right)_{accelerational} \quad (3\text{-}3)$$

The total pressure drop is the value measured by the pressure transducers. The gravitational pressure-drop is given by:

$$\left(\frac{dP}{dz}\right)_{gravitational} = \rho_H \, g \sin(\theta), \quad (3\text{-}4)$$

where ρ_H is the homogeneous density, g is the gravitational acceleration measured using the accelerometers, and θ is the angle of inclination from horizontal. The homogeneous density is used even though the flow is not homogenous, however, the homogeneous density does show up in annular flow equations based on conservation of momentum. In addition, no other appropriate density for annular flow has been identified. The homogeneous density is given by:

$$\frac{1}{\rho_H} = \frac{x}{\rho_g} + \frac{1-x}{\rho_l}, \quad (3\text{-}5)$$

where x is the gas quality, ρ_g is the gas density and ρ_l is the liquid density. The gas density is calculated using the Ideal Gas Law:

$$\rho_g = \frac{P}{(R / M)\, T}, \quad (3\text{-}6)$$

where P is the absolute pressure in the system (kPa), R is the universal gas constant (8.314 kJ/kg K), M is the molecular weight of the gas, and T is the absolute temperature of the gas (K). The system pressure and temperature are recorded just after the test section of the apparatus. The molecular weight of air is 28.97 kg / kmol, and the molecular weight of helium is 4.003 kg / kmol. The liquid density is taken as constant at 998 kg / m^3.

For vertical upwards flow, θ in equation 3-4 is equal to 90^{o}, making $\sin(\theta)$ equal to 1. The accelerational pressure drop can be caused by changes in geometry or due to gas density changes. The flow does not undergo any changes in geometry, but the gas density can change due to the pressure drop. At the highest flow rates the frictional pressure drop can represent 13% of the absolute pressure, causing a similar reduction in the gas density. For a worst-case scenario, the liquid film will remain at the same thickness, causing the gas to flow in a constant area, and the gas velocity is increased by the same percentage. The corresponding increase in the velocity head is approximately 160 Pa, which represents less than two percent of the measured pressure drop. For the lower flows, the pressure drop is even less. For actual flows, it is noted previously that an increase in the gas velocity will result in a thinner liquid film, so the area of flow of the gas may increase, causing less of an increase in the gas velocity. Therefore, the accelerational pressure drop can be neglected.

In order to eliminate problems associated with the compressibility of the two-phase flow, the pressure transducer lines are filled with water prior to data collection. This creates a column of water on the pressure transducer, and thus an initial gravitational pressure head. This value varies based on the gravitational acceleration, and is taken from the all-water files recorded in between the two-phase flows. The frictional pressure drop is then calculated for the various set points, using the measured total pressure drop and the calculated gravitational pressure drop. The set-up for measuring the pressure drop is validated by measuring the pressure drop for single-phase flow.

3.5 Experimental Uncertainty

The method of calculating the experimental uncertainty in the measurements is based on that of Coleman and Steele (2001). For every measurement, there is a bias (systematic) uncertainty, B(m), and a precision (random) uncertainty, P(m). The total uncertainty of a measurement, U(m), is the root-sum-square of the components of uncertainty,

$$U(m) = (B(m)^2 + P(m)^2)^{1/2}. \quad (3\text{-}7)$$

Both the bias and the precision uncertainties are also calculated using the root-sum-square method to combine the components.

3.5.1 Film Thickness

For the film thickness measurements, the bias uncertainty is due to the uncertainties in the tube bore (0.0254 mm), the Teflon calibration inserts (0.02 mm), and the wax coating during calibration (0.02 mm). The total bias uncertainty from these values is 0.038 mm. The precision uncertainty is a combination of the uncertainty in the normalized voltage, the data acquisition error, and the standard error of estimate from the calibration equation used to convert the normalized voltage to film thickness. The uncertainty in the normalized voltage varies based on the voltage reading, ranging from 0.013 mm for the all-air voltage to 0.284 mm for the all-water voltage reading. The variation in the film thickness due to the all-air voltage is due to electrical interference in the film thickness sensors. Any errors in the all-water voltage, due to electrical interference and the dynamic nature of the waves, are magnified due to the normalized voltage dependence on the all-water value. For the range of film thickness encountered

in a typical annular flow, the maximum uncertainty in the normalized voltage is 0.061 mm. The data acquisition error results in an uncertainty of 0.014 mm. The standard error of estimate from the calibration is 0.0744 mm. These values give a total precision uncertainty of 0.097 mm. The maximum total uncertainty (using equation 3-7) is therefore 0.104 mm for the film thickness measurements.

3.5.2 Pressure Drop

The same uncertainty analysis can be applied to the pressure drop measurements, however since the pressure drop calculation relies only on one measurement, it is simpler. The bias uncertainty associated with the pressure drop is due to the uncertainty in the Druck Precision Indicator used for the calibration, and the accuracy of the pressure transducer. The pressure calibrator is accurate to ± 5 Pa, and the pressure transducer has an accuracy of ± 0.5% of the full-scale value, or 69 Pa. Combining these values gives the total bias uncertainty to be 69 Pa. The precision uncertainty is due to the standard error of estimate, the uncertainty in the voltage measurements, and the fluctuations present in the flow. The standard error of estimate from the calibration equation is 66 Pa. The data acquisition error in the measurement of the voltage output of the pressure transducers corresponds to 7 Pa. For constant, all-water flow (single phase flow), the output of the pressure transducer varies up to ± 300 Pa. This can be attributed to the pressure fluctuations present in the flow due to the pumping system. As was mentioned previously, the acceleration of the gas phase can cause an additional pressure drop of 160 Pa, which can be added to the precision uncertainty. The total precision uncertainty is therefore 346 Pa. Combining the bias and the precision uncertainties give

the total uncertainty for the pressure drop to be 353 Pa. The uncertainty values for all other measured values are shown in Table 3.3.

Table 3.3. Uncertainty of measured values.

Parameter	Uncertainty
$\dot{m}_g$ (air)	0.000023 kg/s
$\dot{m}_g$ (helium)	0.000009 kg/s
V_{sl}	0.007 m/s
Gauge Pressure	2.9 KPa
Absolute Pressure	10.6 KPa
Temperature	0.5 ^{o}C

3.6 Data Repeatability

The data to be presented in the following sections were collected at various times, but were still repeatable. The flight data were collected over the course of six days on two different trips to Bordeaux, France. The ground data were collected over a couple of months at the University of Saskatchewan. In some cases, the equipment underwent additional calibration in between the data collection periods. Despite the time or calibration differences, the data collected agree within the uncertainty values presented above.

4.0 NORMAL AND MICROGRAVITY RESULTS

The following sections present the experimental data collected during the two ESA flight campaigns and the post flight ground data. The average film thickness data are presented first, followed by the frictional pressure drop data. For each flow characteristic, the effect of the gas and liquid mass fluxes will be presented for the different gases and gravity levels. Comparisons will then be made to examine the effect of the gravitational acceleration and the gas phase density. All hypergravity data will be discussed separately in Chapter 5. For all graphs, the lines shown are the best-fit lines to the data using a power relationship.

The air-water data were collected over a range of G_l of 75.8 to 314.4 kg/m^{2}s and of G_g from 14.3 to 47.7 kg/m^{2}s. The entire data set for normal gravity, microgravity and hypergravity is tabulated in Appendix B. The helium-water data were collected over a range of G_l of 97.8 to 311.7 kg/m^{2}s and G_g of 5.0 to 11.6 kg/m^{2}s. The entire data set for normal gravity, microgravity and hypergravity is tabulated in Appendix C.

For the following figures, the data are separated into ranges of the liquid or gas mass fluxes that represent a portion of the data where the results are approximately constant. These ranges represent the data where the flow rates have not changed enough to significantly affect the results. Through the remainder of this chapter, these ranges will

be referred to as "constant" gas or liquid mass fluxes. A sample of the digital images of the normal gravity and microgravity flows can be found in Appendix D.

4.1 Average Film Thickness

Figure 4.1 shows the normal gravity, air-water average film thickness values as a function of the gas mass flux and separated into constant liquid mass fluxes. The y-error bars are equal to the uncertainty of 0.104 mm. It can be seen that the influence of changing the liquid mass flux on the average film thickness is minimal: for an increase in the liquid flow rate of over three times, all of the average film thickness values agree within the experimental uncertainty. This will be discussed further in section 4.1.2. For all subsequent figures, the uncertainty bars will be omitted to maintain figure clarity.

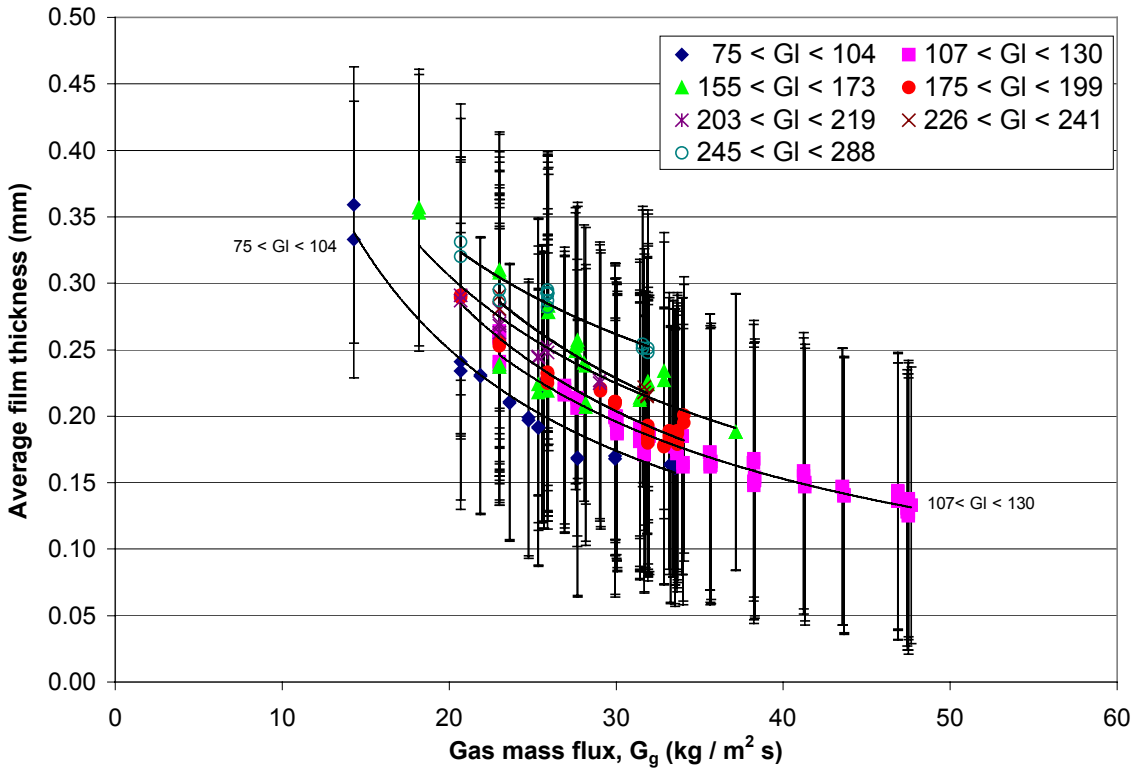

Figure 4.1. Air-water average film thickness and uncertainty for normal gravity.

Figure 4.1 is repeated without the uncertainty bars in Figure 4.2a. Figures 4.2 and 4.3 show the effect of the gas and liquid mass fluxes on the average film thickness, for air-water and helium-water at normal and microgravity. The air-water data are presented at the top, and the helium-water data are shown at the bottom. The normal gravity data is shown on the left, with the microgravity data on the right. Figure 4.2 shows the effect of the gas mass flux while maintaining the liquid mass flux constant. For all liquid flow rates, the average film thickness values vary inversely with the gas mass flux. An increase in the gas mass flux results in a decrease in the average film thickness. This result is visible for all cases, regardless of gravity level or gas phase.

Figure 4.3 shows the effect of the liquid mass flux on the average film thickness values. The lines represent the constant gas flow rates. For a uniform gas mass flux, the average film thickness values vary directly with the liquid flow rate. An increase in the liquid flow rate results in an increase in the average film thickness and a decrease in the liquid flow rate causes a reduction in the film thickness values. However, the change in the film thickness due to an increase in the liquid mass flux is not as great as the effect of the gas mass flux. The film thickness for the helium-water flow at normal gravity for G_g of 5 – 6 kg/m^2 s is approximately constant over the range of liquid flows. As the high gas mass fluxes the average film thickness values are approximately equal.

In all cases (normal or microgravity, air or helium) the trend is the same. The average film thickness decreases as the gas mass flux increases or as the liquid mass flux decreases. This is in agreement with past studies of air-water annular flow in microgravity and vertical upwards flow in normal gravity.

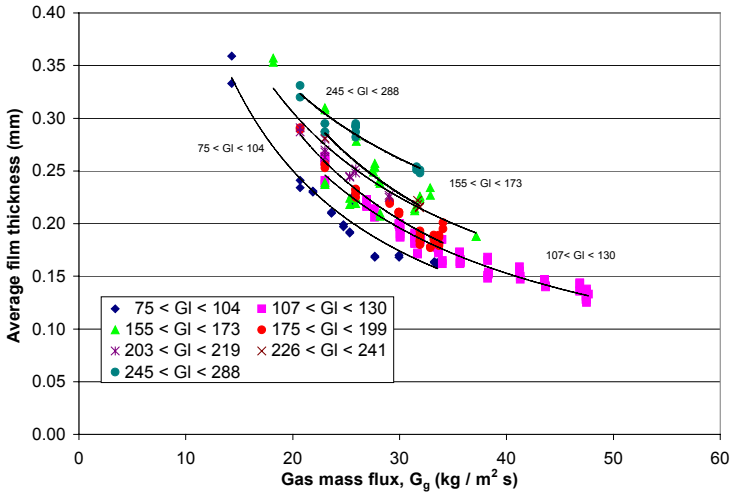

a) Air-water film thickness, normal gravity

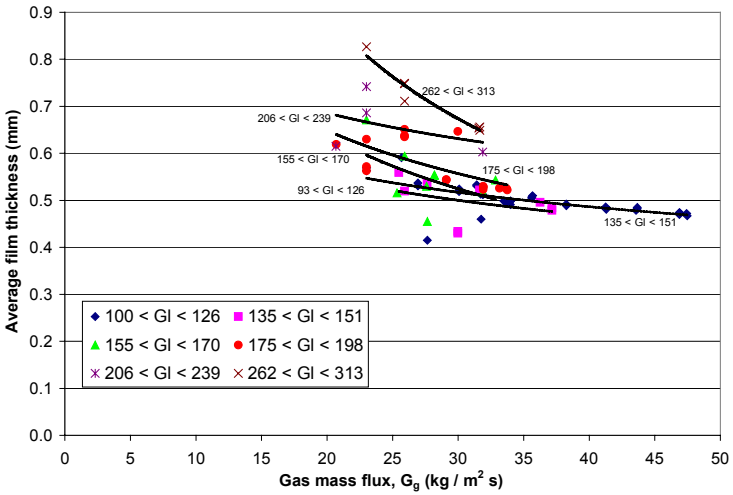

b) Air-water film thickness, microgravity

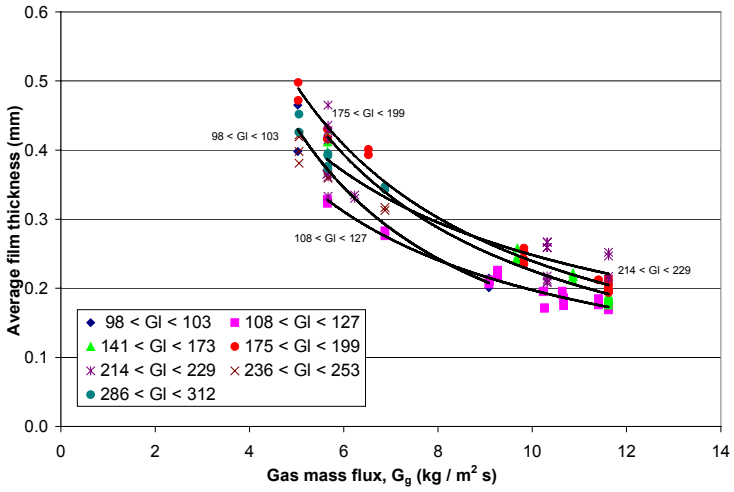

c) Helium-water film thickness, normal gravity

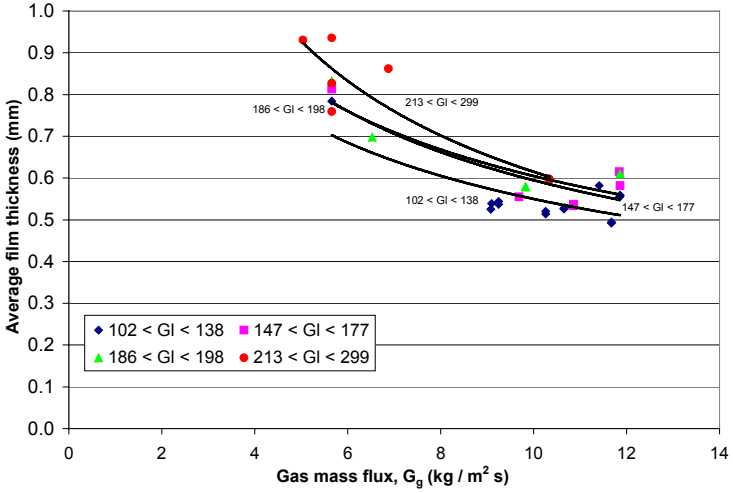

d) Helium-water film thickness, microgravity

Figure 4.2. Effect of gas mass flux on the average film thickness.

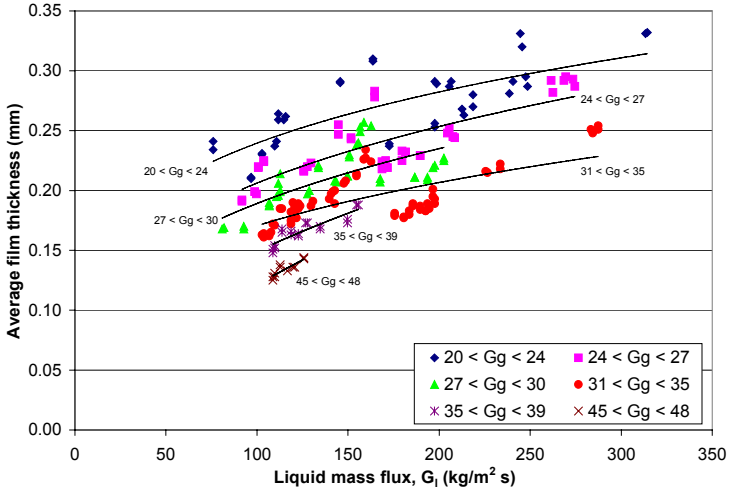

a) Air-water film thickness, normal gravity

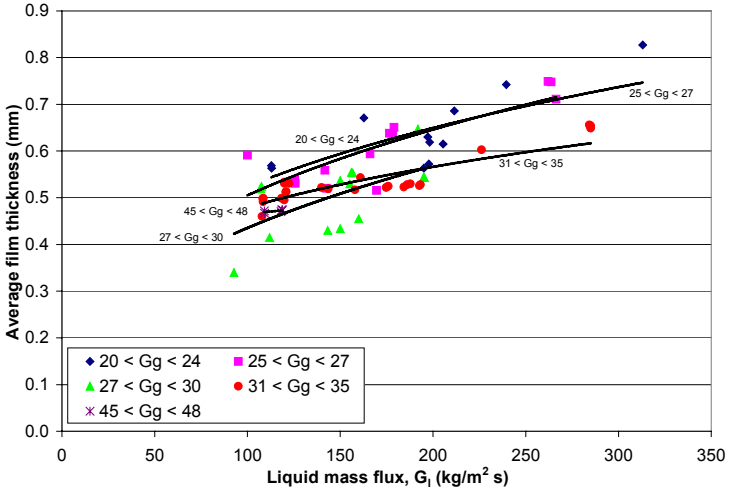

b) Air-water film thickness, microgravity

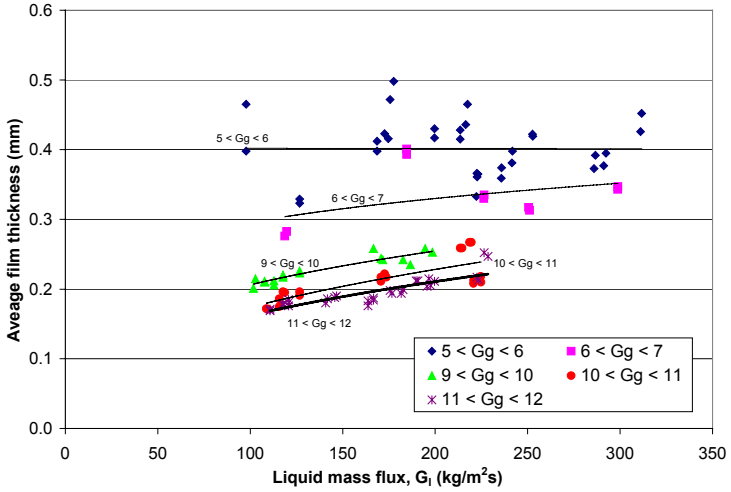

c) Helium-water film thickness, normal gravity

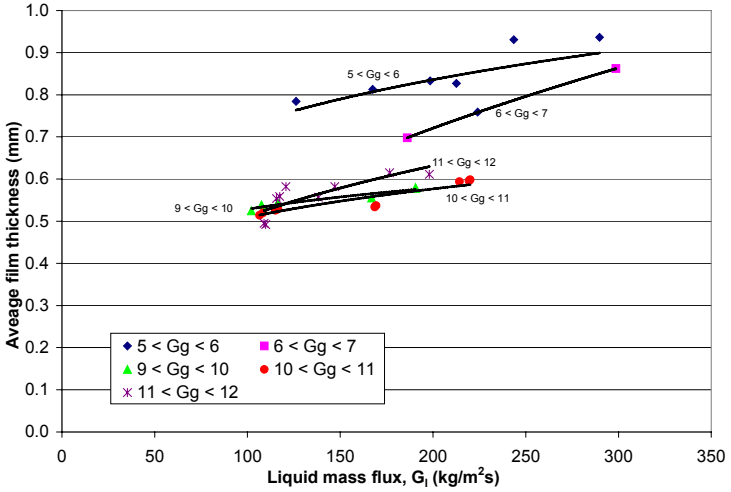

d) Helium-water film thickness, microgravity

Figure 4.3. Effect of liquid mass flux on the average film thickness.

4.1.1 Effect of Gravitational Acceleration

The comparison between the vertical upwards data and the microgravity data for the air-water flow is shown in Figure 4.4. The figure shows the average film thickness values as a function of the liquid mass flux plotted on logarithmic axes, with the data separated by gas mass flux. The normal gravity data points are shown as solid symbols and are represented as the "N" data set, while the microgravity data points are shown as open symbols and as the "M" data set. For the same liquid and gas mass flow rates the microgravity data are larger than the normal gravity data. The range of the normal gravity film thickness is 0.13 mm to 0.33 mm while the microgravity film thickness ranges from 0.34 mm to 0.83 mm. The smallest increase in the average film thickness is 0.17 mm and the largest increase is 0.50 mm. The average value of the normal gravity film thickness is 0.21 mm and the average film thickness for the microgravity data is 0.54 mm. The root-mean-square (RMS) increase in the average film thickness due to the reduction in gravity is 0.34 mm.

The helium-water data for microgravity and vertical upwards, normal gravity are shown on a log scale plot in Figure 4.5. The lines represent the data of the gas mass flux within the indicated ranges. The solid symbols show the normal gravity data points, labeled "N", while the microgravity data points are shown with open symbols and labeled "M". The range of the normal gravity average film thickness is 0.17 mm to 0.43 mm. For the same gas and liquid mass flux, the range of the microgravity data is 0.49 mm to 0.94 mm. The average normal gravity film thickness is 0.25 mm, and the average microgravity film thickness is 0.63 mm. For the helium-water data, the smallest

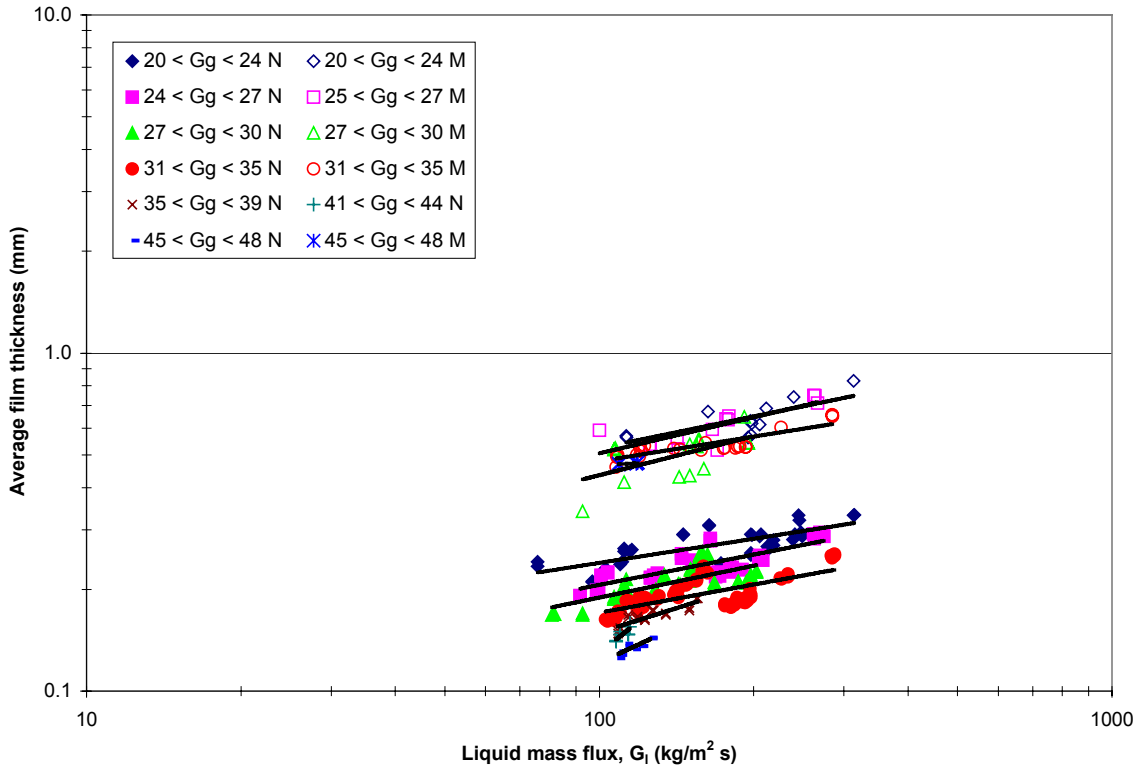

Figure 4.4. Air-water average film thickness for normal and microgravity.

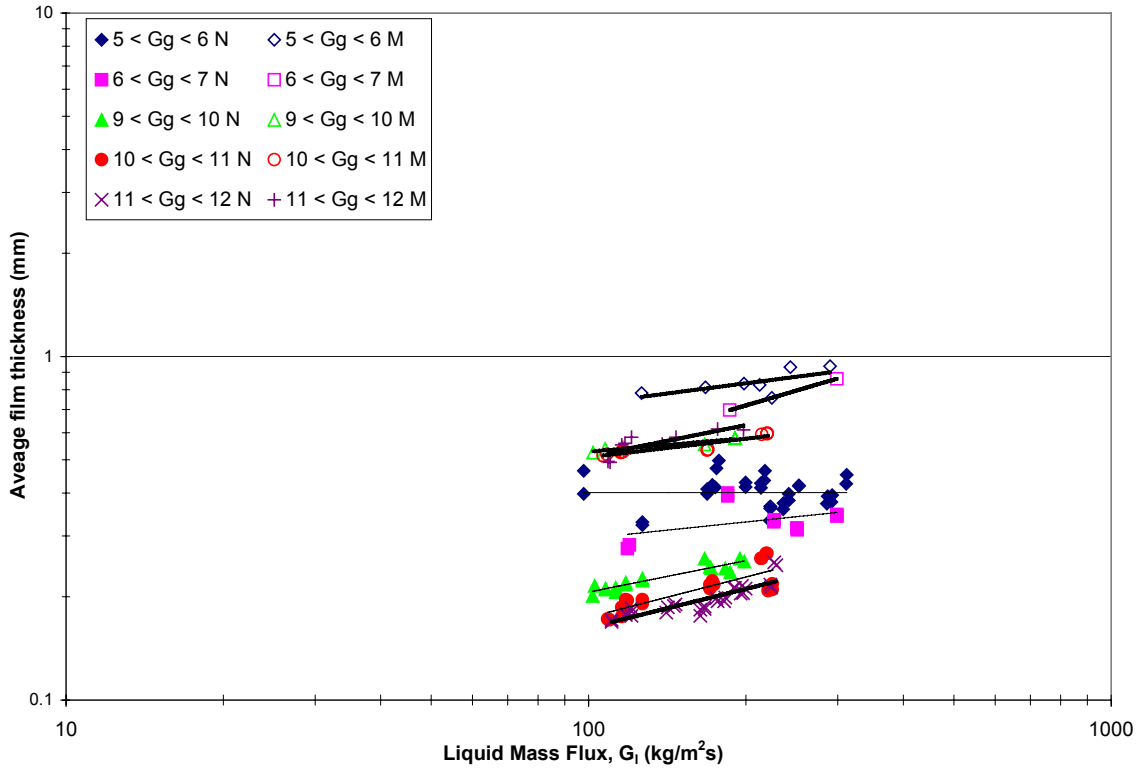

Figure 4.5. Helium-water average film thickness for normal and microgravity.

increase due to the reduction in gravity is 0.30 mm, the largest increase is 0.56 mm, and the RMS increase in the film thickness is 0.38 mm. All of the helium-water film thickness values are approximately the same as the air-water values. This is discussed in section 4.1.2.

For both the air-water and the helium-water data, the microgravity average film thickness is thicker than the vertical upwards data. This is in agreement with the work of Fujii *et al.* (1998) and Rezkallah (1990). For the microgravity film thickness values, Fujii *et al.* (1998) report that the normalized average film thickness (film thickness divided by the tube radius) gives values between approximately 0.1 and 0.2, while the normal gravity data gives values between approximately 0.03 and 0.09. Using the same normalized film thickness for the current set of data (both air-water and helium-water) gives values of 0.07 to 0.21 for the microgravity data, and between 0.03 and 0.10 for the normal gravity data. For almost the same flow conditions and tube diameter as the current data, Fujii *et al.* (1998) report that the average film thickness is two to five times larger in microgravity compared to the normal gravity. The current data shows an increase of between two and four times due to the reduction in gravity. The increase in the film thickness can be attributed to a reduced shear stress on the flow, which causes a lower interfacial friction factor. This lower interfacial friction may allow waves to become larger and not be sheared off into the gas core, thus giving a larger average.

4.1.2 Effect of Gas Density

In order to match the helium-water data points with the air-water data points, the liquid mass flux was kept constant. Due to the low density of helium and the equipment capabilities, it was not possible to match the gas mass flux. Therefore, the gas phase specific energy is used. Figure 4.6 shows the normal gravity average film thickness values as a function of the gas phase specific energy. The air-water data are shown with the solid symbols and the helium-water data are shown with open symbols. For a constant liquid mass flux, the average film thickness is dependant on the gas specific energy but not strongly on the gas density. A narrow band based on a fixed liquid flow rate can represent both the air-water data and the helium-water data. Similar results can be seen in microgravity, Figure 4.7.

Over the range of the gas energy values, the film thickness varies significantly. However, as was mentioned earlier, over the range of increase of the liquid flow rate, the increase in the film thickness is not very large. The entire data set for each gravity level can be represented by one general trend. Figure 4.8 shows the normal gravity average film thickness values as a function of the gas energy, without identifying the individual liquid flow rates, for both the air-water and the helium-water data. The solid line represents the best-fit power series line to the data, and the dashed lines represent the best fit line plus and minus twenty percent. The majority of the data fall within this range, which is less than or approximately equal to the experimental uncertainty. Figure 4.8 shows that over the range of liquid mass fluxes from 75 to 199 kg/m^2s, the change in the liquid mass flux has minimal effect on the average film thickness.

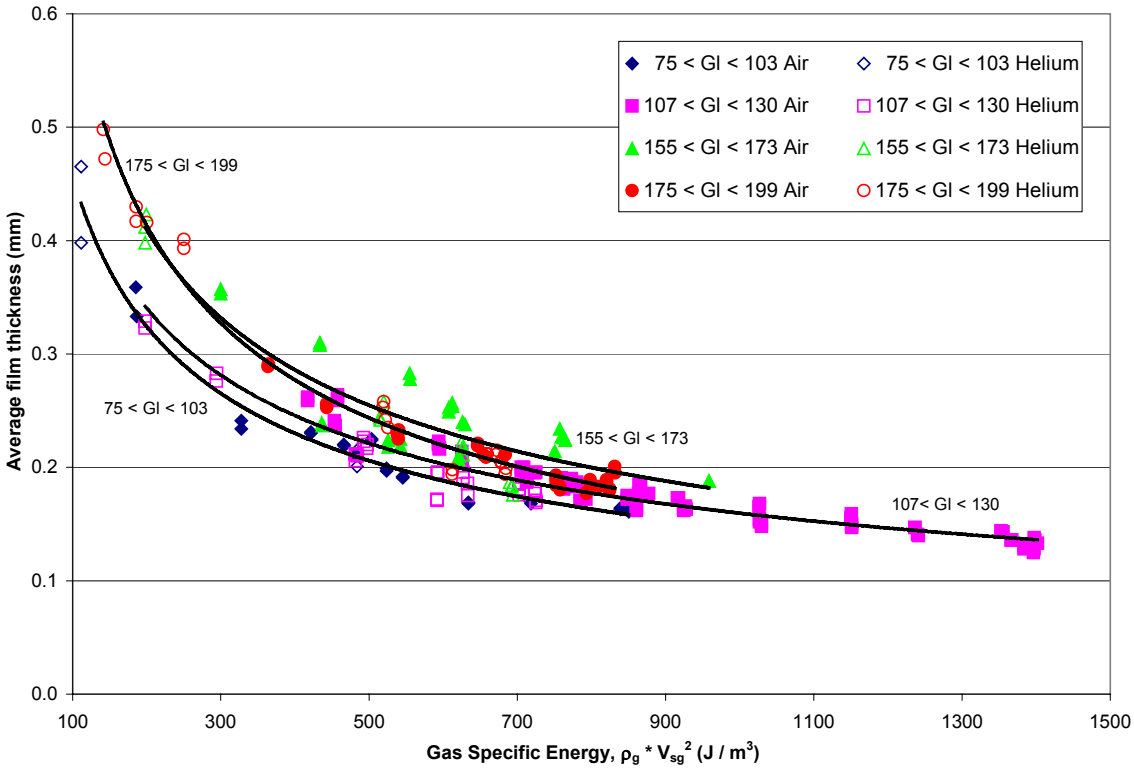

Figure 4.6. Air-water and helium-water average film thickness, normal gravity.

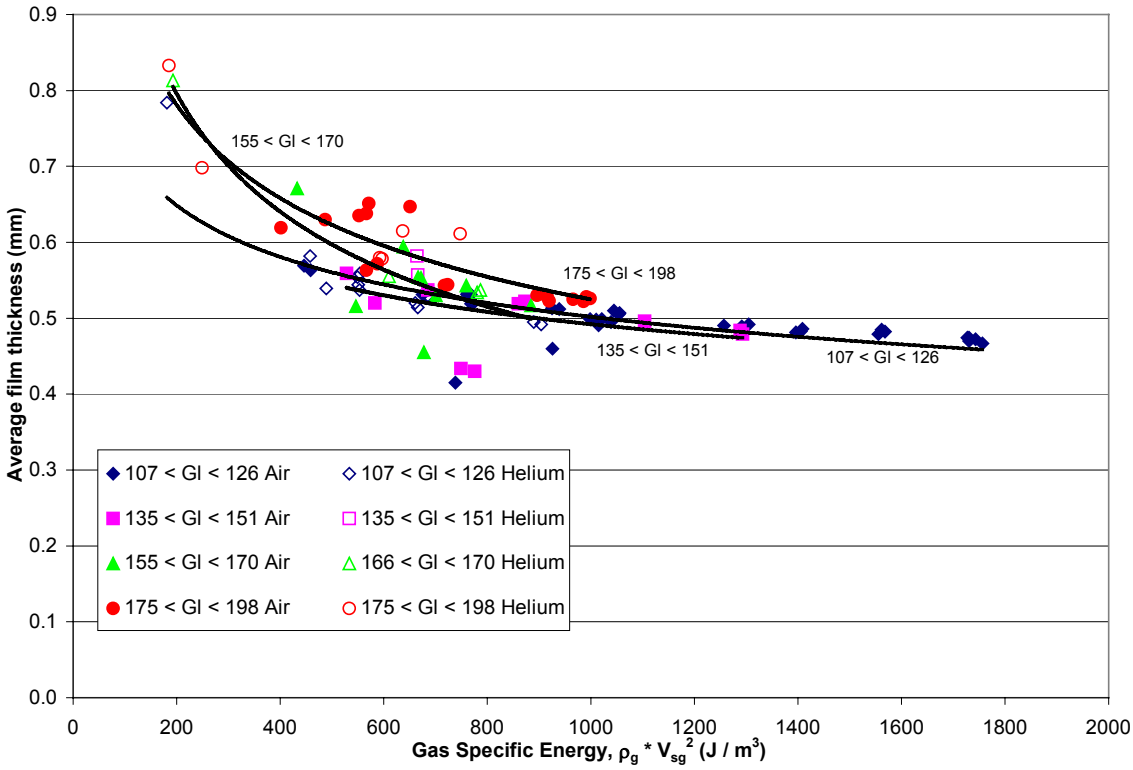

Figure 4.7. Air-water and helium-water average film thickness, microgravity.

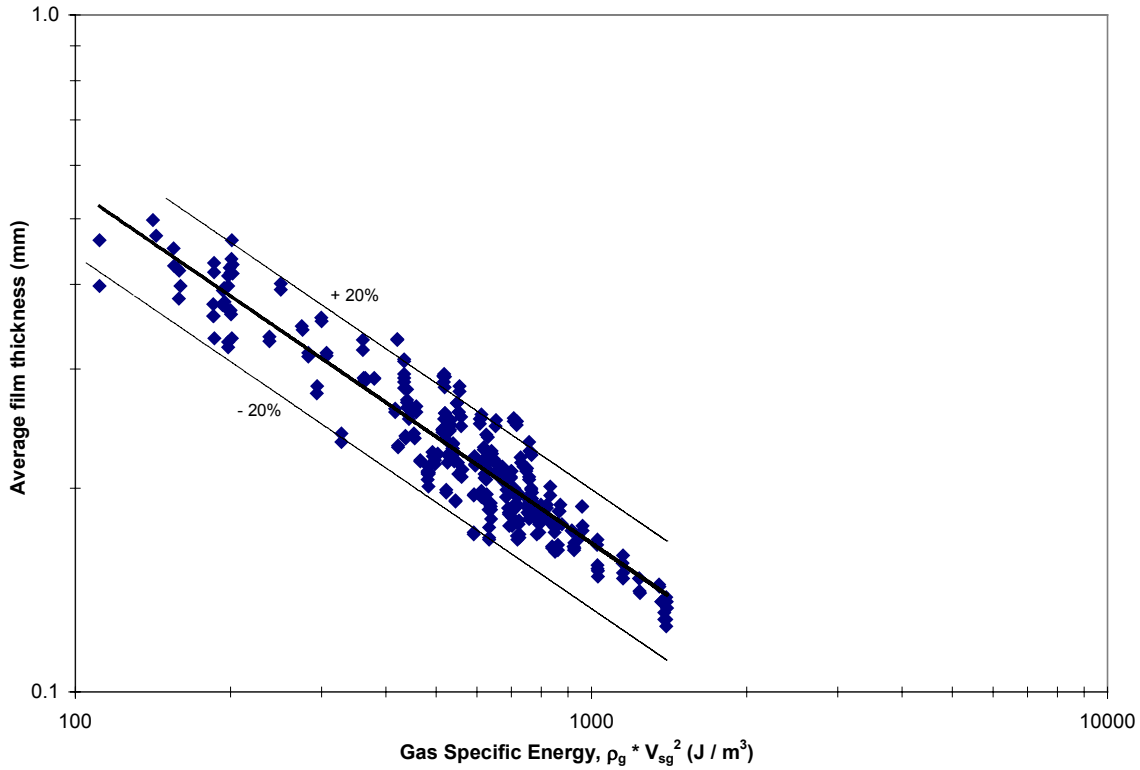

Figure 4.8. Air-water and helium-water average film thickness values, normal gravity.

4.1.3 Effect of Liquid Evaporation

Barbosa *et al.* (2002) concluded that the evaporation of the liquid could be significant at low liquid flow rates. This, along with uncertainties in the measurement of the liquid film flow rate, can account for most of the apparent entrainment. The largest amount of evaporation will occur during the largest gas flows. However, in order to saturate dry air at 30^o, approximately 28 g of water per kg of air, or 9.47 * 10^{-5} kg/s, is required. At the lowest liquid flow rates, (approximately 76 kg/m^{2}s), the liquid evaporation / air saturation represents less than 1.9% of the total liquid flow rate. The evaporation of water in the helium flow will be even less due to the reduced attraction between the helium and water molecules. Therefore, the effect of the liquid evaporation on the average film thickness can be neglected for the range of flow rates presently studied.

However, for smaller liquid flow rates this effect may become significant and should be further examined.

4.2 Average Frictional Pressure Drop

The average frictional pressure drop for the two-phase flow in is shown in Figures 4.9 and 4.10. The air-water data are presented at the top, and the helium-water data are shown at the bottom. The normal gravity data are shown on the left, with the microgravity data on the right. Figure 4.9 shows the effect of the gas mass flux on the frictional pressure drop, with the data separated by liquid flow rates. For all liquid flow rates, it can be seen that the frictional pressure drop varies directly with the gas flow rate. For a constant liquid flow rate, the pressure drop increases as the gas mass flux increases, and decreases if the gas mass flux decreases. Figure 4.10 shows the effect of the liquid mass flux on the frictional pressure drop for constant gas flux. As with the gas flow rate the pressure drop varies directly with the liquid mass flux. For all gas flow rates the pressure drop increases as the liquid mass flux increases. From Figures 4.9 and 4.10, it can be seen that for an increase in either the gas or the liquid mass flux, the frictional pressure drop increases.

4.2.1 Effect of Gravitational Acceleration

The comparison between the vertical upwards data and the microgravity data for the air-water flow is shown in Figure 4.11, which shows the pressure drop plotted versus the gas mass flux. The lines are the best-fit power lines to the range of liquid mass fluxes.

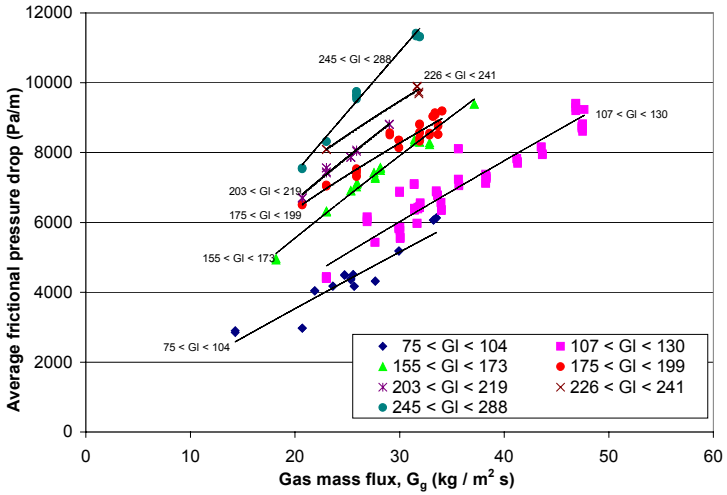

a) Air-water frictional pressure drop, normal gravity

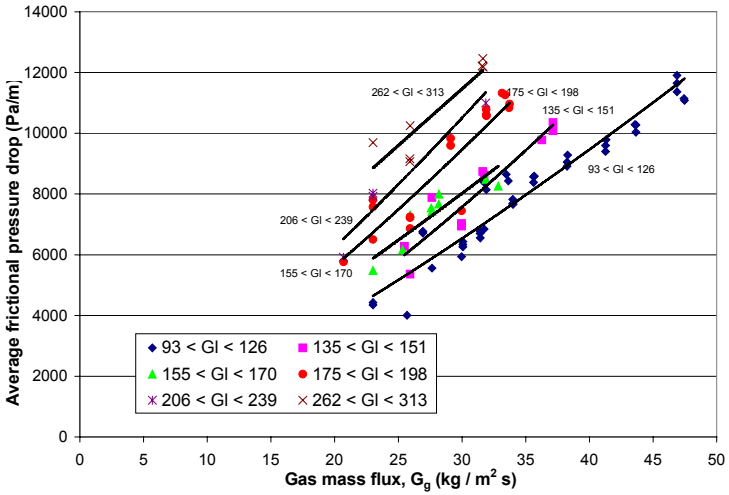

b) Air-water frictional pressure drop, microgravity

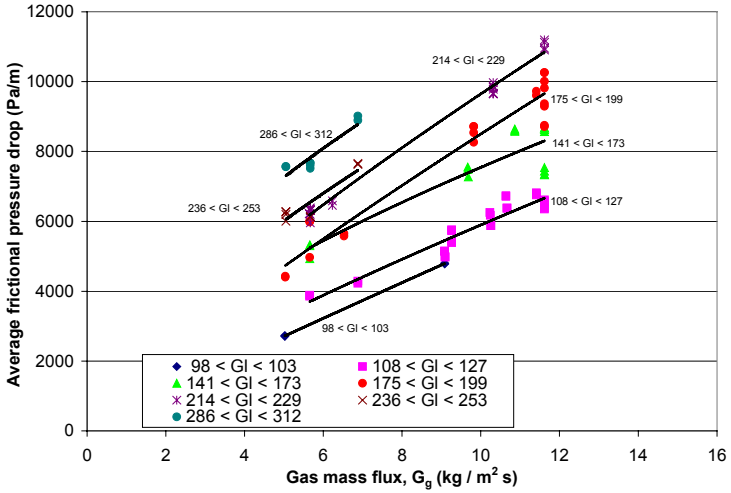

c) Helium-water frictional pressure drop, normal gravity

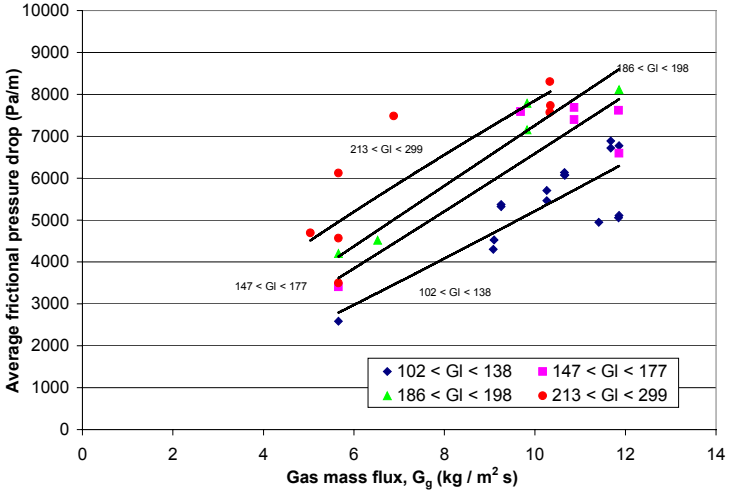

d) Helium-water frictional pressure drop, microgravity

Figure 4.9. Effect of gas mass flux on the average frictional pressure drop.

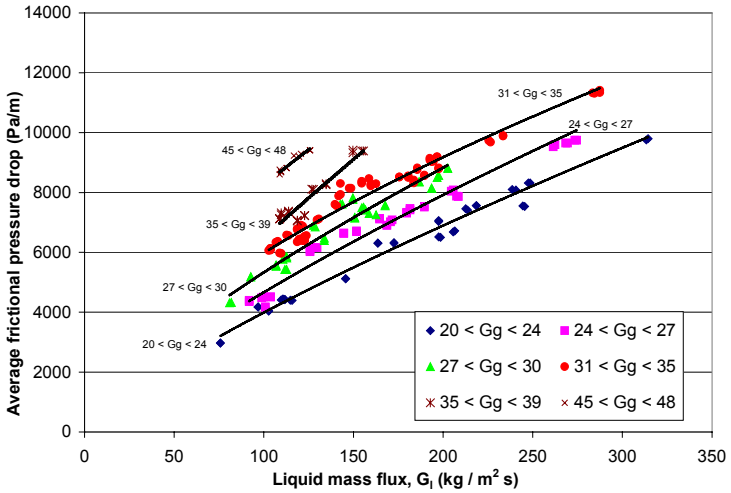

a) Air-water frictional pressure drop, normal gravity

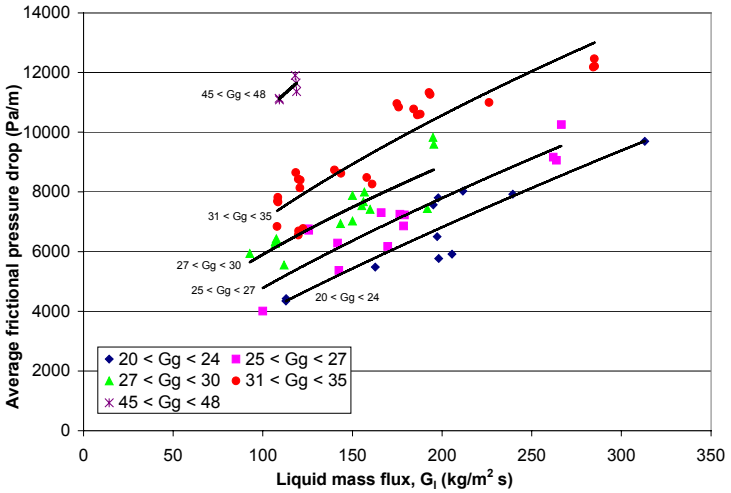

b) Air-water frictional pressure drop, microgravity

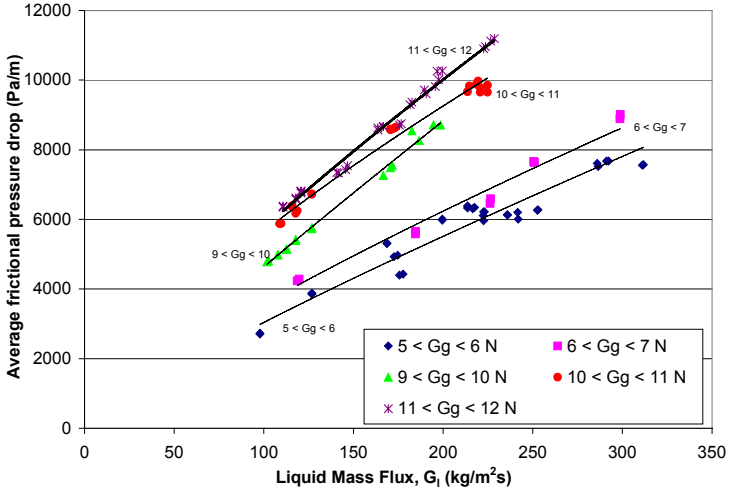

c) Helium-water frictional pressure drop, normal gravity

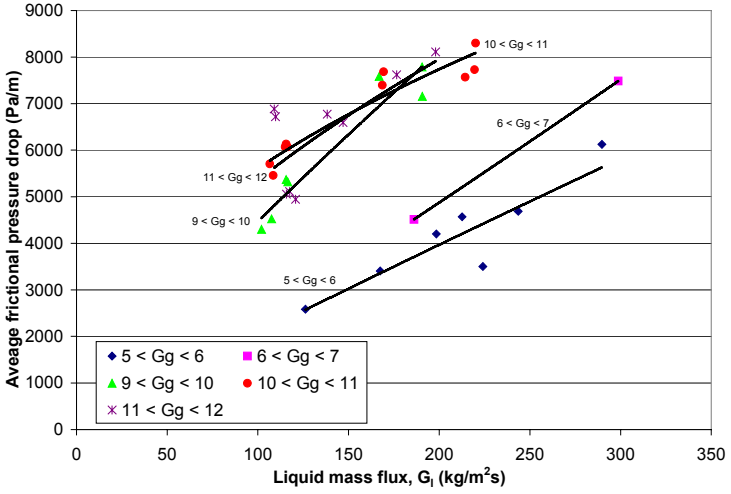

d) Helium-water frictional pressure drop, microgravity

Figure 4.10. Effect of liquid mass flux on the average frictional pressure drop.

The normal gravity data are shown with solid symbols and labeled "N", and the microgravity data are shown with open symbols and labeled "M". The dark lines represent the normal gravity data and the light lines represent the microgravity data. In Figure 4.11, the microgravity values for the low gas flow rates (less than 27 kg/m^{2}s) are equal to the normal gravity data. As the gas mass flux is increased, the microgravity pressure drop values become larger than the normal gravity values, by up to nearly 30% for the highest gas flow rates. For the same flow rate increases, the microgravity flow is influenced more by the increase in the gas mass flux than the normal gravity flow.

Figure 4.12 shows the effect of the reduction in gravity on the average frictional pressure drop for the helium-water data. The vertical upwards data are shown as solid symbols and labeled "N", while the microgravity data are shown with open symbols and labeled

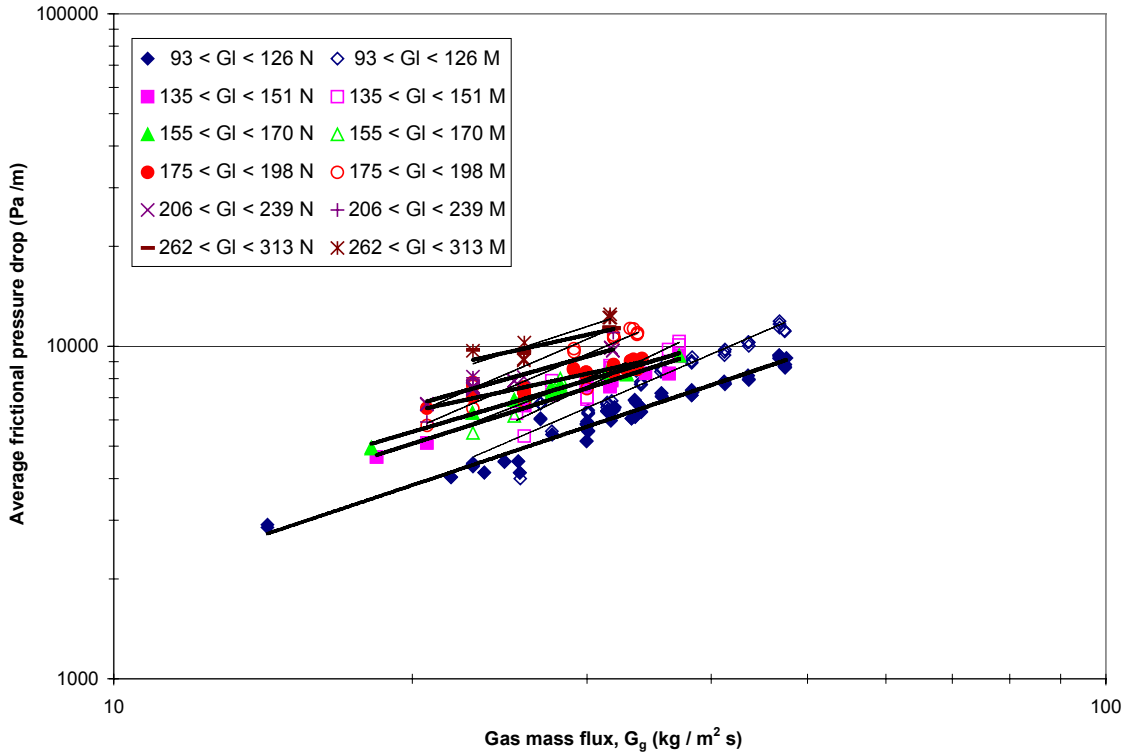

Figure 4.11. Effect of reduced gravity on air-water average frictional pressure drop.

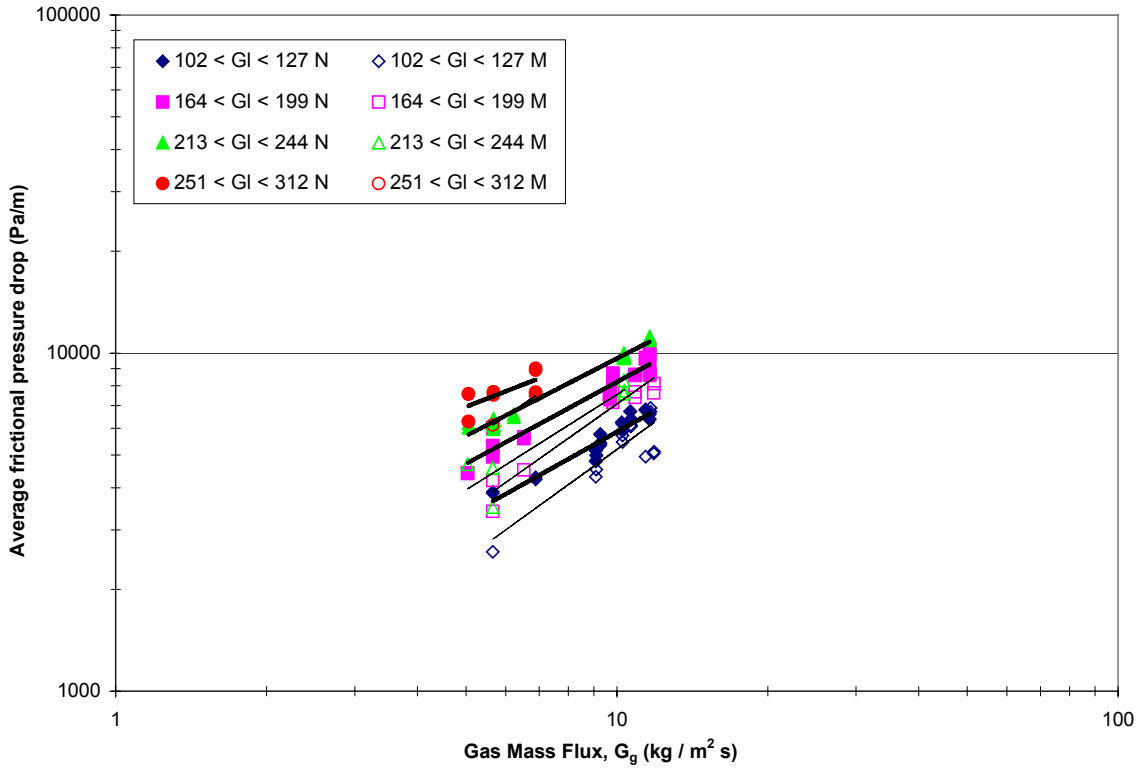

Figure 4.12. Effect of reduced gravity on helium-water average frictional pressure drop.

"M". For the helium-water data, the reduction in the gravity level causes the frictional pressure drop to decrease for all gas flows. As the gas mass flux is increased, the difference between the microgravity pressure drop and the normal gravity pressure drop is reduced. This is different from the absolute comparison of microgravity and normal gravity data for the air-water flows. However, for both air-water and helium-water, as the gas mass flux increases, the microgravity pressure drop increases more than the normal gravity pressure drop. If the gas mass flux is increased further and the same trend continues, the microgravity pressure drop would eventually be equal to and then larger than the normal gravity data. If the trend of the air-water data, shown in Figure 4.11, is continued to lower gas flow rates, the microgravity pressure drop would be less than the normal gravity data. Although the air water and the helium-water data

show different results due to the reduction in gravity, all the data follow the same trend. The frictional pressure drop increases more rapidly due to the gas mass flux at reduced gravity than at normal gravity.

4.2.2 Effect of Gas Density

The normal gravity average frictional pressure drop for air-water and helium-water is shown in Figure 4.13. The air-water data are shown with solid symbols and the helium-water data are shown with open symbols. The frictional pressure drop is plotted versus the gas specific energy, with the data separated by liquid mass flux. It can be seen that both the air-water and the helium-water data can be represented by one line based on a liquid flow rates. All of the ranges of liquid flow rates have approximately equal slopes in the figure. As with the film thickness, the frictional pressure drop is dependant on the liquid mass flux and the gas specific energy, but not directly on the gas density.

Figure 4.14 shows the pressure drop in microgravity versus the gas specific energy. This figure shows similar results as the normal gravity data. The lines of constant liquid mass flux can represent the combined air-water and helium-water frictional pressure drop, and all the lines have approximately equal slopes.

From the previous graphs, it can be seen that for vertical upwards co-current annular flow, both the average film thickness and the frictional pressure drop are affected by the change in the gravitational acceleration, but not significantly by the change in the gas density. The microgravity average film thickness values are larger than the normal gravity values by a ratio of approximately two to four. The data for the air-water flow

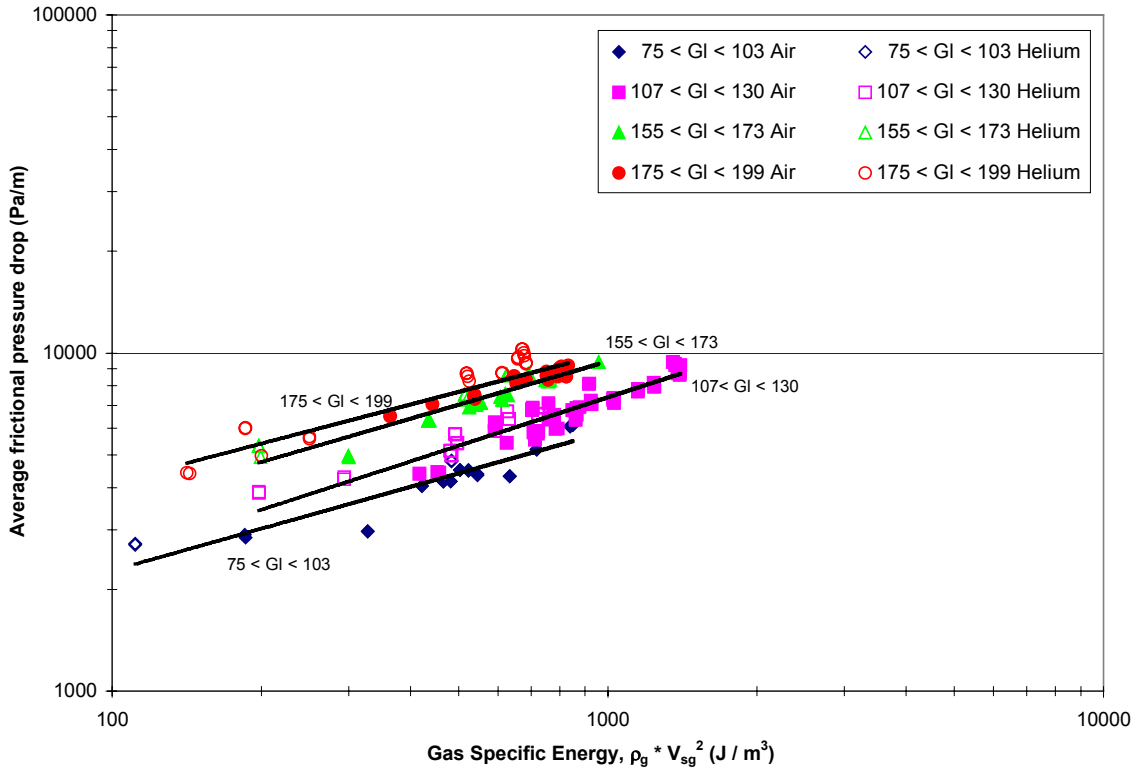

Figure 4.13. Air-water and helium-water average frictional pressure drop, normal gravity.

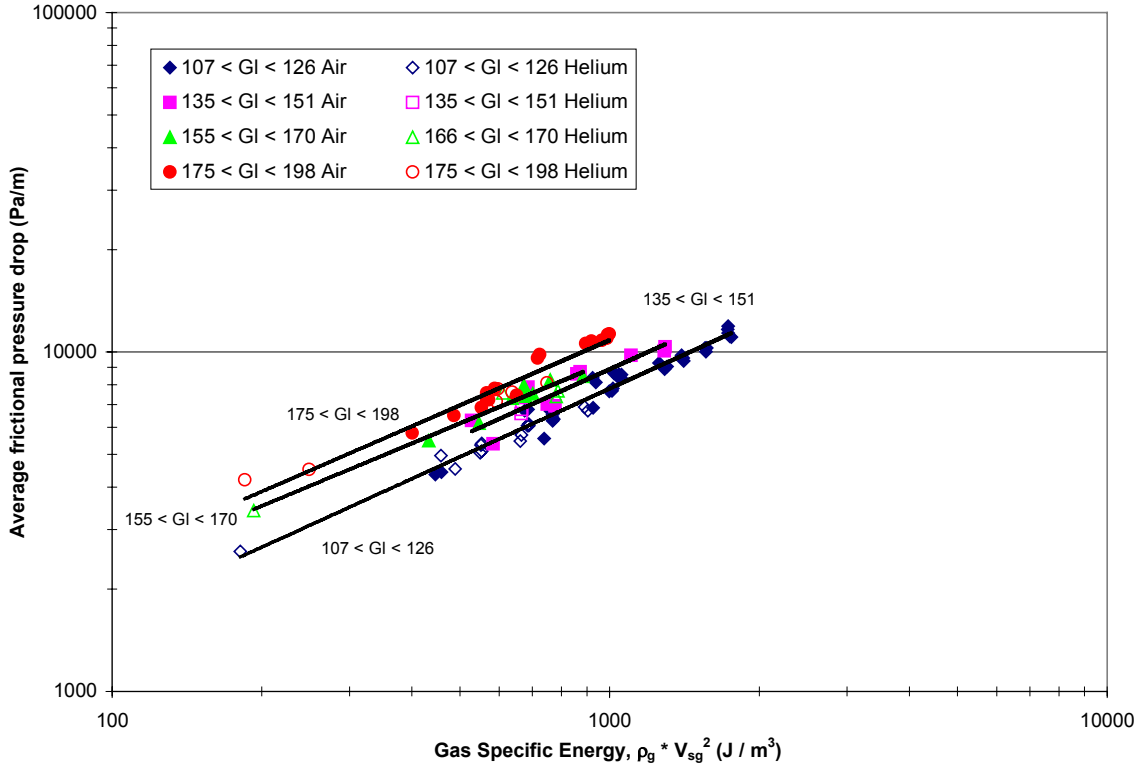

Figure 4.14. Air-water and helium-water average frictional pressure drop, microgravity.

and the helium-water flow can be combined into a common data set, based on gas specific energy. Over the range of liquid flow rates, all of the average film thickness values agree within approximately 20%.

The reduction in gravity causes the frictional pressure drop to increase its dependence on the gas mass flux. For low gas flow rates, the microgravity pressure drop is less than the normal gravity value, but as the gas flow is increased, the microgravity values exceed the normal gravity data. Similar to the film thickness results, both the air-water and the helium-water can be combined into a common data set, based on the gas specific energy. New correlations for the different gravity levels, based on the influence of the gas specific energy, will be presented in Chapter 6.

5.0 HYPERGRAVITY RESULTS

The results presented in Chapter 4 deal only with the data collected during the microgravity portions of the parabolic flights and the normal gravity data collected during ground testing. The Weber number range of these data is from 21 to 230. Using a flow regime map for co-current vertical upwards data (Figure 1.1), it can be determined that all of these data represent annular flow for both normal gravity and microgravity. Unfortunately, no such flow regime map has been developed for the hypergravity environment studied.

Matching the mass flow rates and the flow regimes between normal and microgravity allows a direct comparison to the effect of the reduced gravity. Matching only the mass flow rates between the normal gravity data and the hypergravity data can provide some conclusions to the effect of increased gravity on the average film thickness and frictional pressure drop. However, an understanding of the flow regime is necessary to ensure the data all represent the same flow.

In the increased gravity environment, the flow will be subject to an increased opposing force. The two-phase flow will therefore require greater driving energy to maintain the same characteristics as seen in normal gravity. The greater force opposing the flow may cause the flow to experience flooding or flow reversal, or even bring the flow into a

churn type of regime. An image of the hypergravity flow can be found in Appendix D. The following sections will present the collected hypergravity data, in a similar format to chapter 4, with the normal gravity results shown as a range for reference only. As in Chapter 4, the data are separated into ranges that represent results that are approximately constant.

5.1 Average Film Thickness

The annular flow average film thickness values for the hypergravity conditions are shown in Figures 5.1 and 5.2. The air-water data are shown on the top, and the helium-water data shown on the bottom. Figure 5.1 shows the effect of the gas mass flux, and the lines represent constant liquid velocity. Figure 5.2 has lines of constant gas mass flux and shows the effect of the liquid flow rate. The same trends discussed for Figures 4.1 and 4.2 are visible in 5.1 and 5.2. The film thickness varies inversely with the gas velocity and directly with the liquid velocity. As well, the average film thickness values show a large scatter, with the differences due to the various flow rates not as distinct as previously shown for normal or microgravity.

5.1.1 Effect of Gravitational Acceleration

The effect of the increased gravity on the air-water annular flow average film thickness is shown in Figure 5.3. The figure shows the average film thickness as a function of the liquid mass flux with the lines representing constant gas mass flux. From this figure, it can be seen that for the same gas and liquid flow rates, the hypergravity data are larger

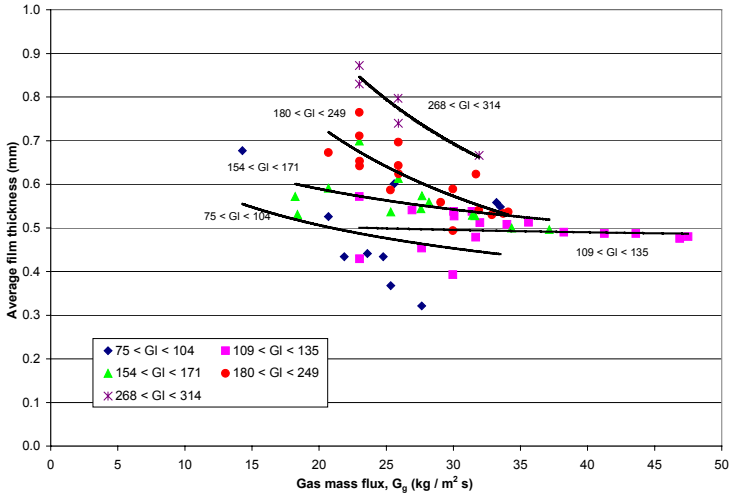

a) Air-water average film thickness

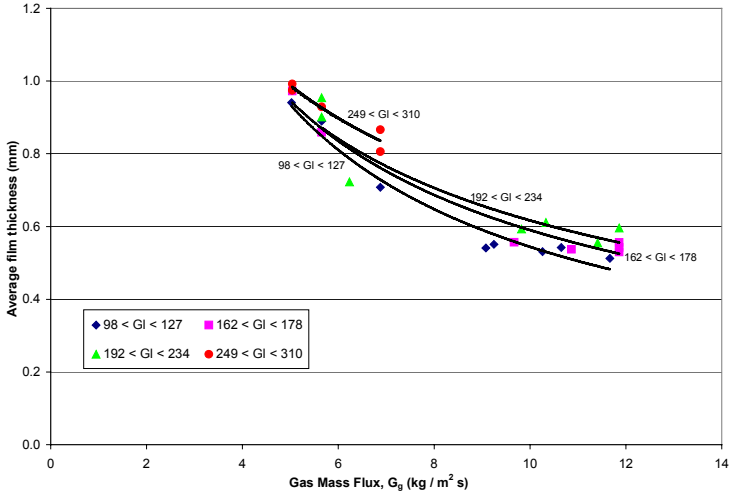

b) Helium-water average film thickness

Figure 5.1. Effect of gas mass flux on the average film thickness, hypergravity.

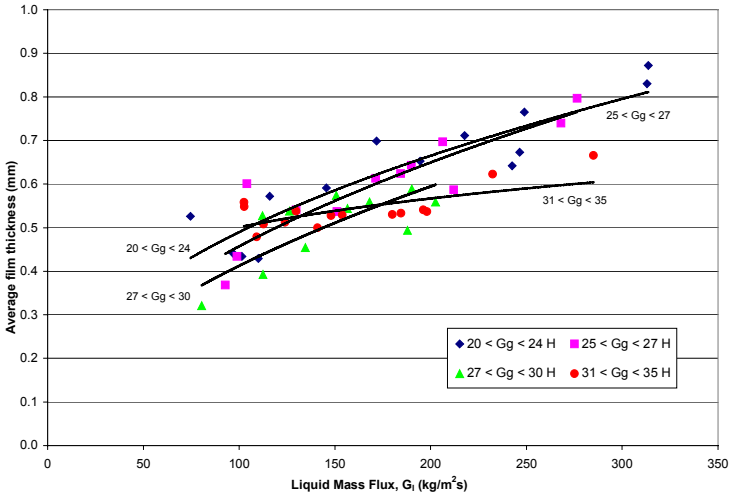

a) Air-water average film thickness

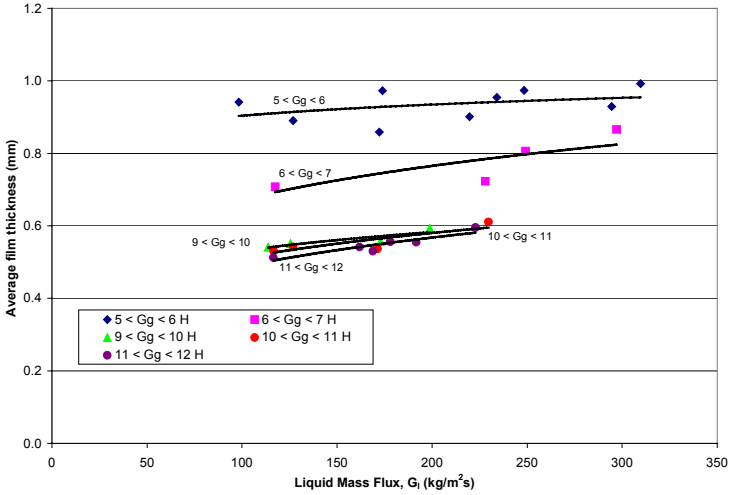

b) Helium-water average film thickness

Figure 5.2. Effect of liquid mass flux on the average film thickness, hypergravity.

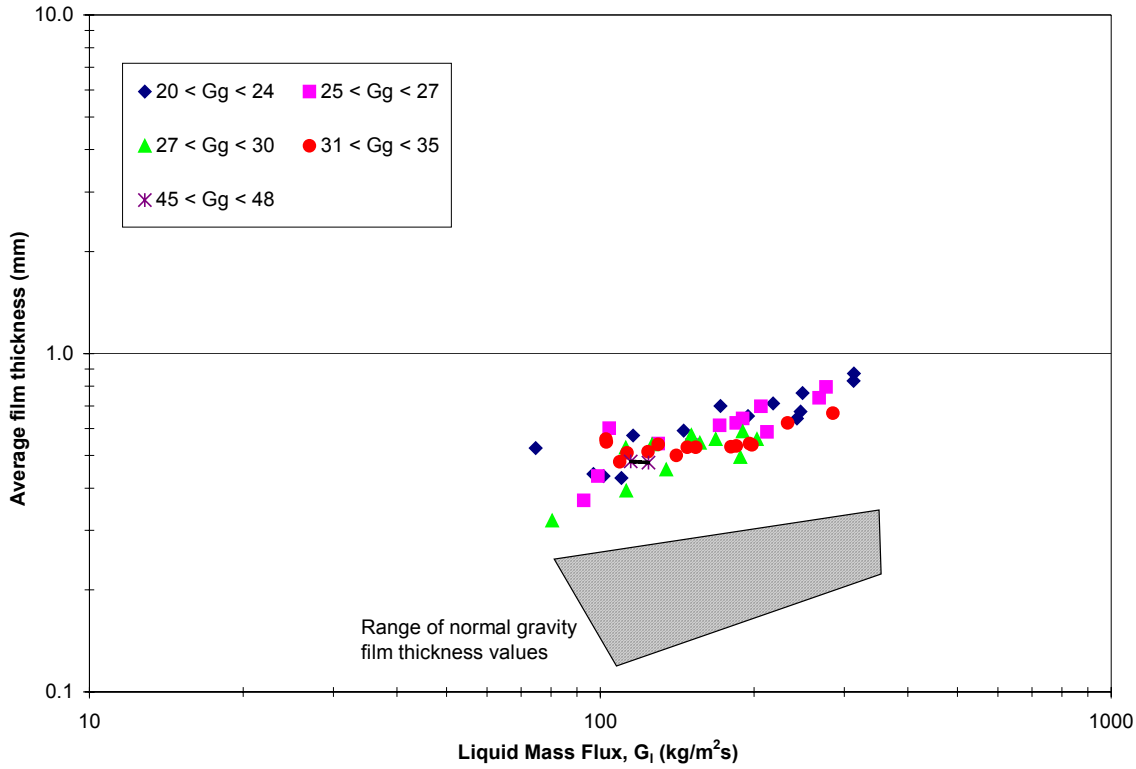

Figure 5.3. Air-water average film thickness for normal and hypergravity.

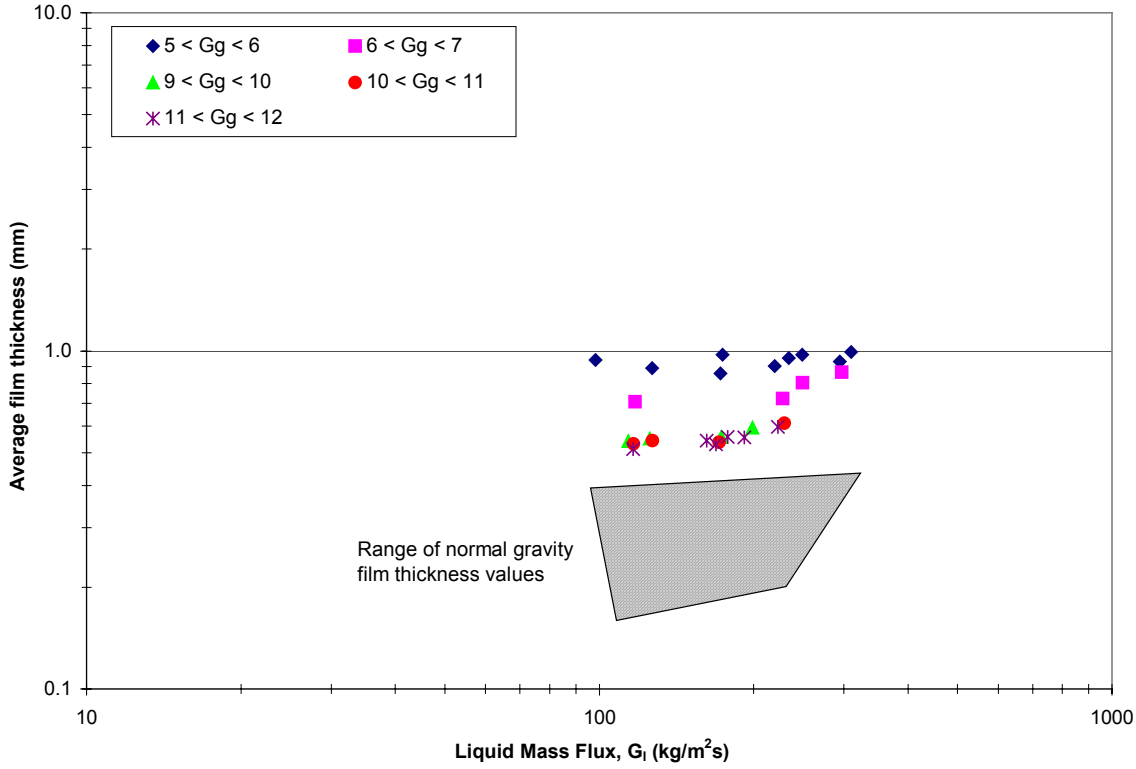

Figure 5.4. Helium-water average film thickness for normal and hypergravity.

than the normal gravity data. The range of the hypergravity data is 0.32 mm to 0.87 mm, with an average of 0.56 mm.

The effect of the increased gravity on the helium-water annular flow average film thickness is shown in Figure 5.4. As with the air-water data, the helium-water hypergravity film thickness values are larger than the normal gravity values. The hypergravity values range of 0.51 mm to 0.99 mm, with an average of 0.71 mm.

5.1.2 Effect of Gas Density

The hypergravity average film thickness values as a function of the gas energy for air-water and helium-water are plotted in Figure 5.5. Similar to the results for normal and microgravity, the hypergravity data do not show any difference in the trends due to the difference in the gas density. Both the air-water and the helium-water data can be represented by a single power series, based on the gas specific energy.

5.2 Average Frictional Pressure Drop

The hypergravity frictional pressure drop results are shown in Figures 5.6 and 5.7. Figure 5.6 shows the effect of the gas mass flux, with lines of constant liquid mass flux. Figure 5.7 shows the effect of changing the liquid flow rate, while maintaining the gas flow rate constant. The air- water flows are shown on the top, while the helium-water flows are shown on the bottom. With both figures, the same results can be seen as with

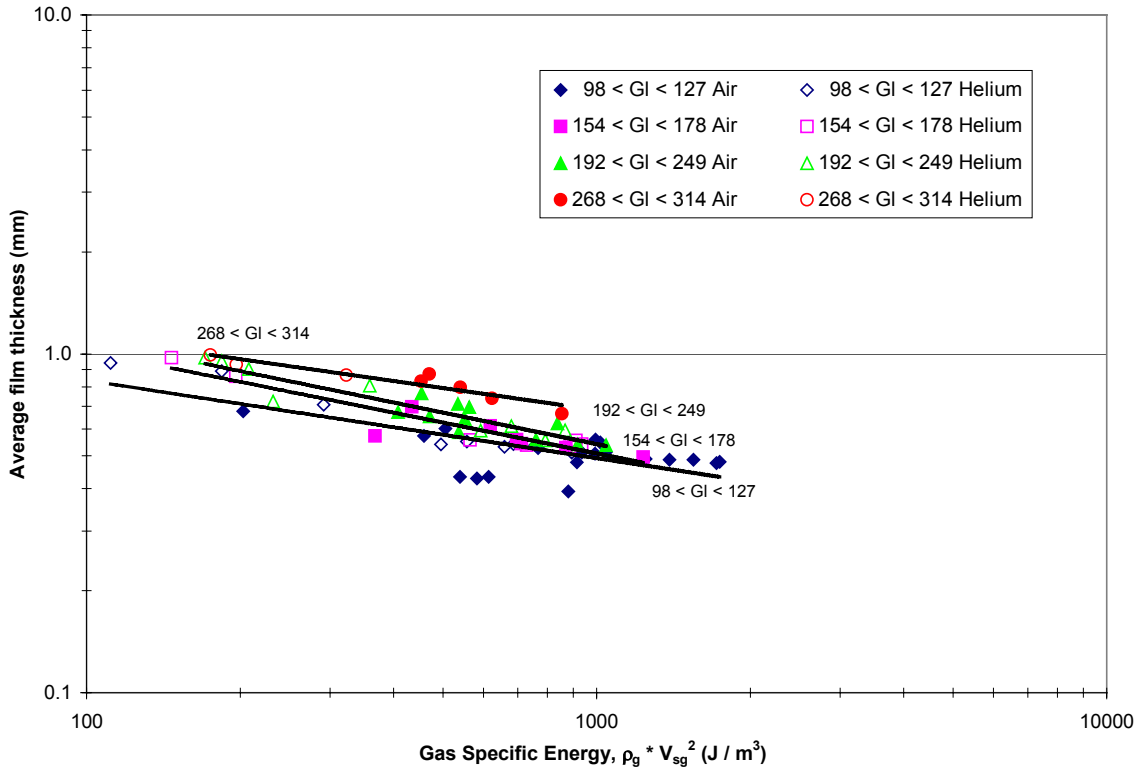

Figure 5.5. Air-water and helium-water average film thickness, hypergravity.

the normal and microgravity data. The frictional pressure drop increases with increasing liquid flow rate and with increasing gas flow rate.

5.2.1 Effect of Gravitational Acceleration

The effect of the increased gravity on the average frictional pressure drop is shown in Figures 5.8 and 5.9. Figure 5.8 shows the air-water data, and Figure 5.9 shows the helium-water data. For both figures, the power series representing the normal gravity data are shown as dashed lines, while the data points and the dark lines represent the hypergravity data.

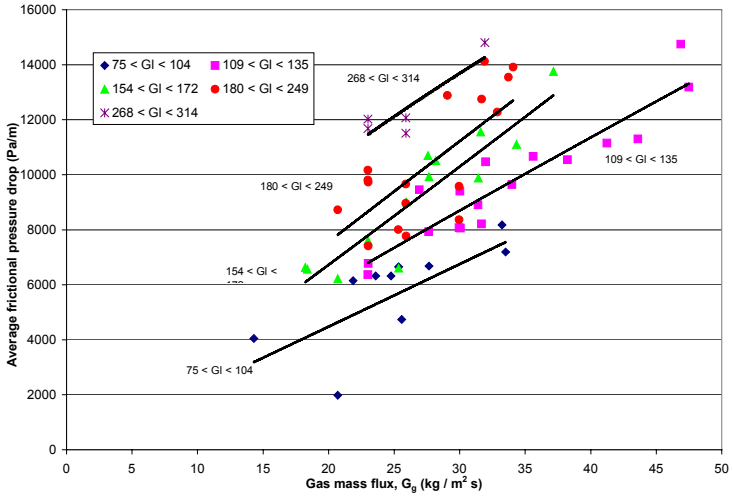

a) Air-water average frictional pressure drop

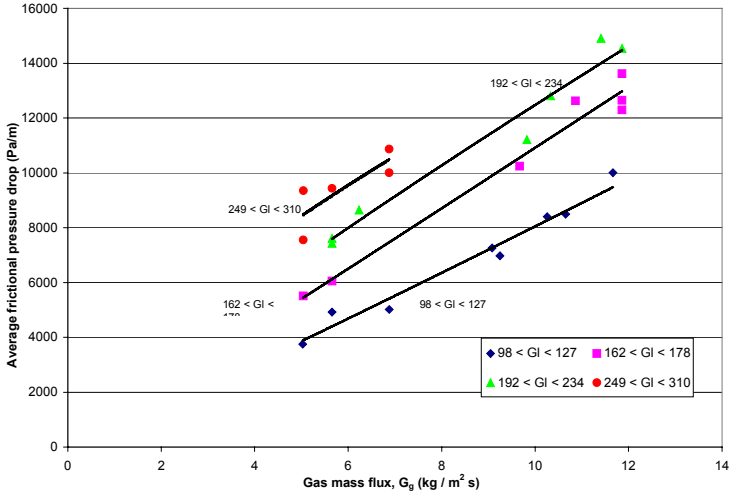

b) Helium-water average frictional pressure drop

Figure 5.6. Effect of gas mass flux on the average frictional pressure drop, hypergravity.

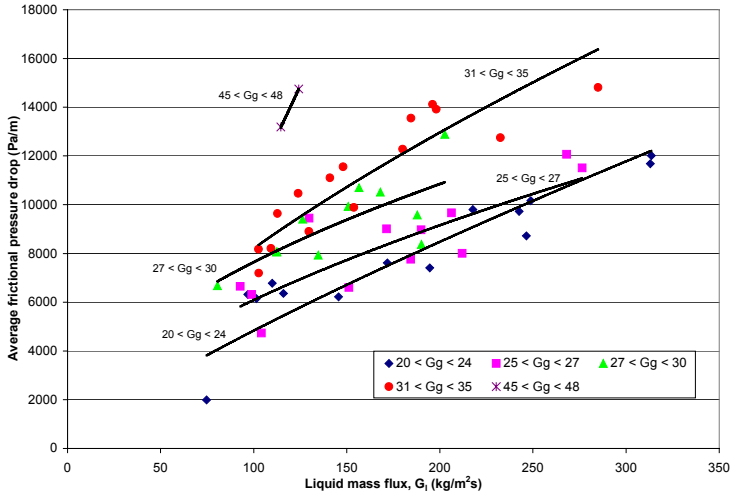

a) Air-water average frictional pressure drop

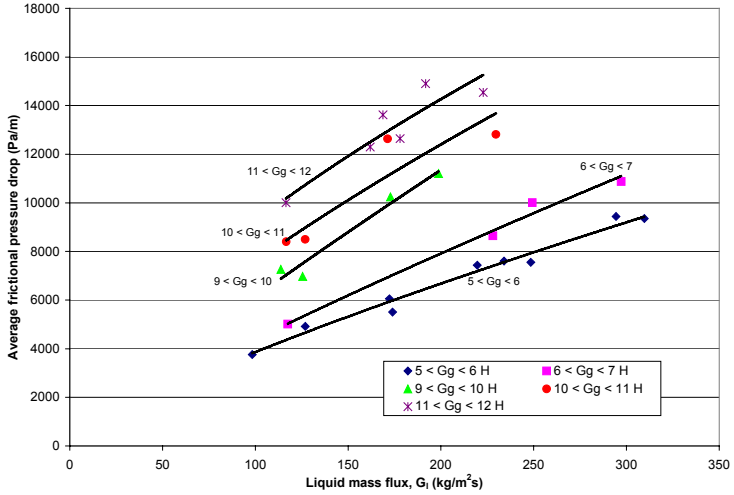

b) Helium-water average frictional pressure drop

Figure 5.7. Effect of liquid mass flux on the average frictional pressure drop, hypergravity.

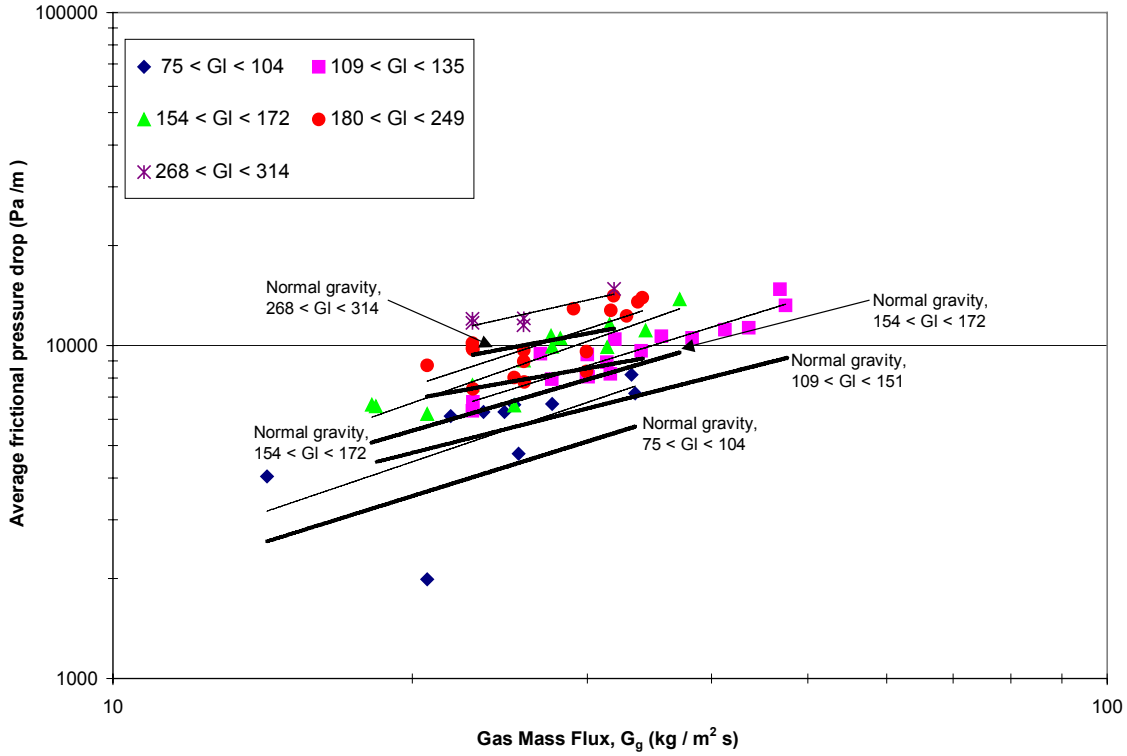

Figure 5.8. Air-water average frictional pressure drop for normal and hypergravity.

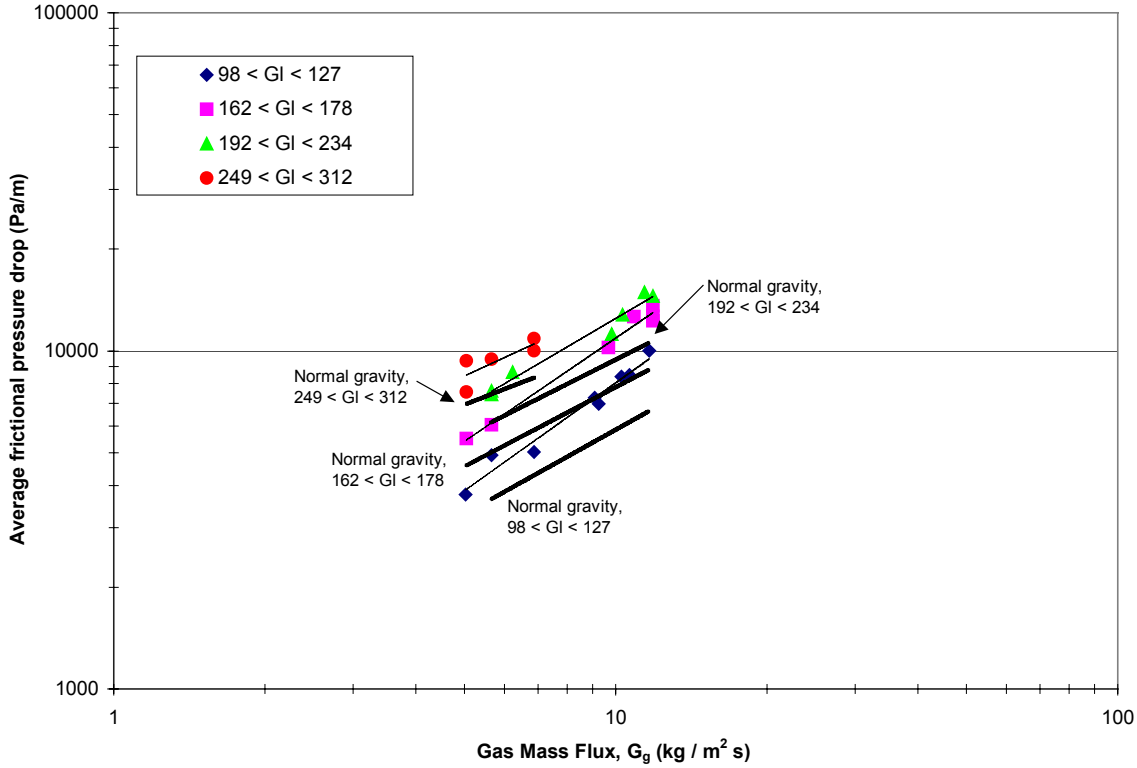

Figure 5.9. Helium-water average frictional pressure drop for normal and hypergravity.

For both air-water and helium-water flows, the increase in the gravity level causes the frictional pressure drop to increase. A change in the liquid mass flux causes approximately the same increase in the pressure drop for normal gravity and hypergravity. An increase in the gas mass flux causes the hypergravity data to increase more than the normal gravity data, giving the hypergravity data a larger slope than the normal gravity data. This trend is more visible with the helium-water flow in Figure 5.9, but is still present in the air-water flow. The increase in the frictional pressure drop can be attributed to the increase in the shear stress and interfacial friction factor associated with the rougher flow.

5.2.2 Effect of Gas Density

The combined frictional pressure drop data for helium-water and air-water flows are shown in Figure 5.10. The air-water data are shown with the solid symbols and the helium-water data are shown with open symbols. Similar to the normal gravity data presented earlier, the two data sets (with different gas densities) can be combined based on the gas specific energy and give comparable results.

For all of the hypergravity data presented, the general trends previously identified for vertical upwards co-current annular flow still apply. The average film thickness increases with an increase in the liquid mass flux, and decreases with an increase in the gas mass flux. An increase in either the liquid or the gas flow rates will cause the average frictional pressure drop to increase. For the same mass flow rates, a change

from normal gravity to hypergravity will cause both the film thickness and the frictional pressure drop to increase.

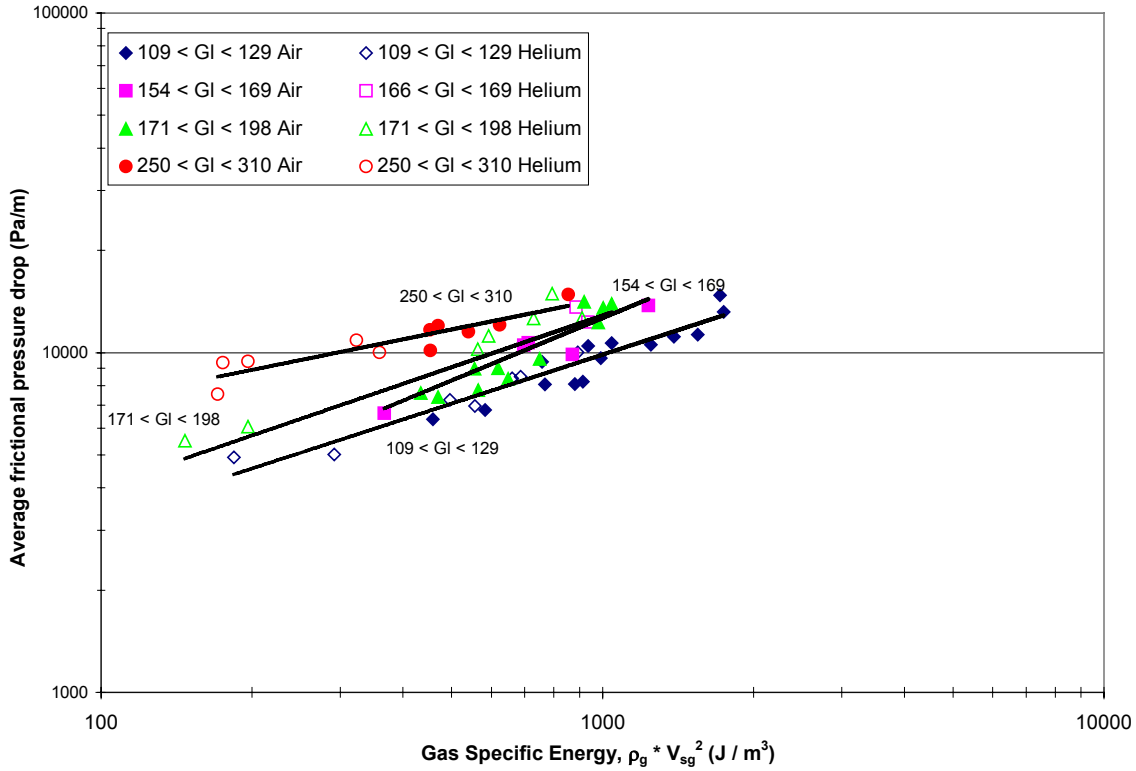

Figure 5.10. Air-water and helium-water average frictional pressure drop, hypergravity.

6.0 NON-DIMENSIONAL EQUATIONS

Using the same dimensionless groups as de Jong (1999), new correlations could be developed to represent the data presented in Chapters 4 and 5. The current set of data can be used to identify the exponents on the density ratio to modify the non-dimensional film thickness (equation 1-15) and the non-dimensional pressure drop (equation 1-23). Similar to the work of de Jong (1999), the following correlations are derived without including the effect of gravity in the analysis. Therefore, separate correlations are developed for the three gravity levels studied: normal gravity, microgravity, and hypergravity.

6.1 Film Thickness Equations

Figure 6.1 shows the non-dimensional film thickness values for the normal gravity data. The air-water and helium-water data are plotted together, as one data set. The predicted film thickness values are obtained from

$$\rho_l V_{sl} \delta / \mu_l = 39 \, Re_{sl}^{0.2} \, (x / (1-x))^{-1.0} \, (\rho_g / \rho_l)^{0.5} \, . \qquad (6\text{-}1)$$

The new powers were calculated by plotting the left hand side divided by two of the terms on the right hand side against the third term. The slope of the best-fit line is then the power on the third term. This process was repeated until they converged to the

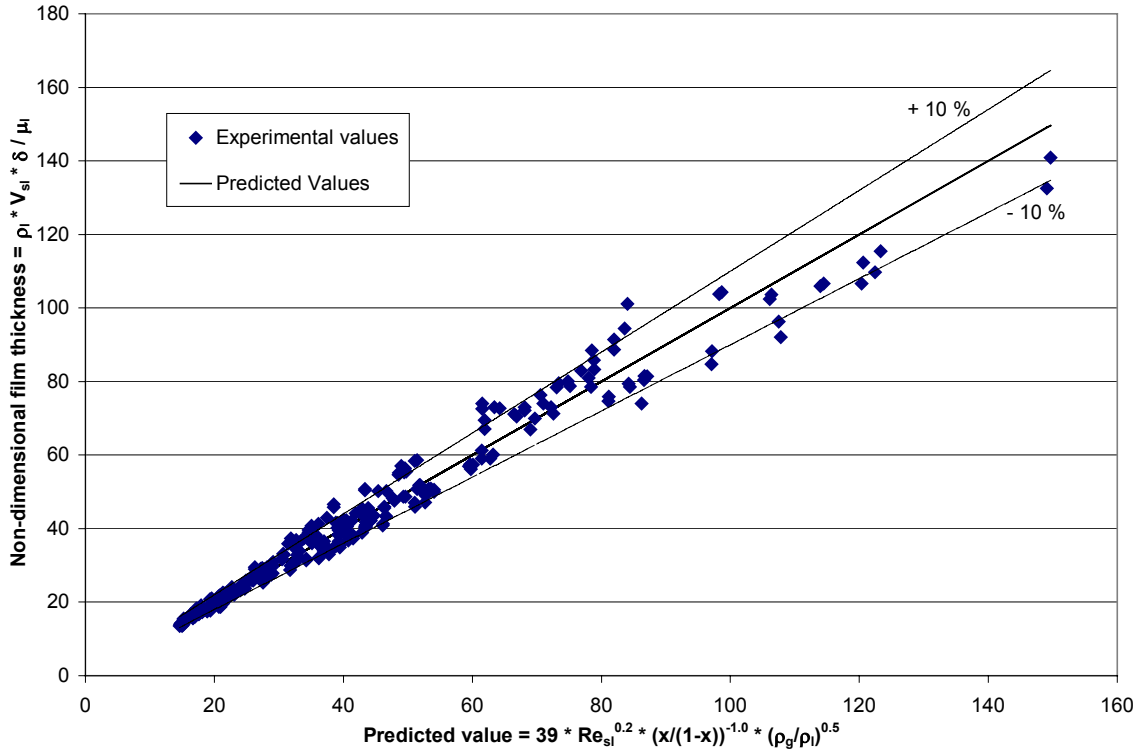

Figure 6.1. Measured and predicted non-dimensional film thickness for normal gravity (equation 6-1).

values shown. This modified equation is able to predict the majority of the film thickness data to within ± 10%, as shown by the light lines on the figure.

A comparison of the normal gravity film thickness values with previous correlations can be found in Figure 6.2. The film thickness values calculated based on the correlation of Willets (1987) and of Fukano and Furukawa (1998) are plotted against equation 6-1. Both of these correlations agree within the uncertainty of equation 6-1. Willets' theoretical development of the relationship between the pressure drop and the film thickness is applicable, even considering the different gas density. The correlation of Fukano and Furukawa (1998), which was developed based on two-phase flows with

air as the gas phase, does predict some change due the gas density. However, this change is minimal, with the values agreeing within the uncertainty.

Figure 6.3 shows the non-dimensional microgravity film thickness plotted against the calculated film thickness, using the equation

$$\rho_l V_{sl} \delta / \mu_l = 0.2 \, Re_{sl}^{0.9} \, (x / (1-x))^{-0.4} \, (\rho_g / \rho_l)^{0.2} \, . \qquad (6\text{-}3)$$

The powers on the Reynolds number and the quality ratio are close to the powers earlier identified by de Jong (1999). This equation shows that the microgravity average film thickness is more dependant on the liquid Reynolds number and less dependant on the gas quality and the density ratio than the normal gravity average film thickness. As with the normal gravity data, this equation can predict the majority of the film thickness data to within ± 10%, as shown by the light lines on the figure.

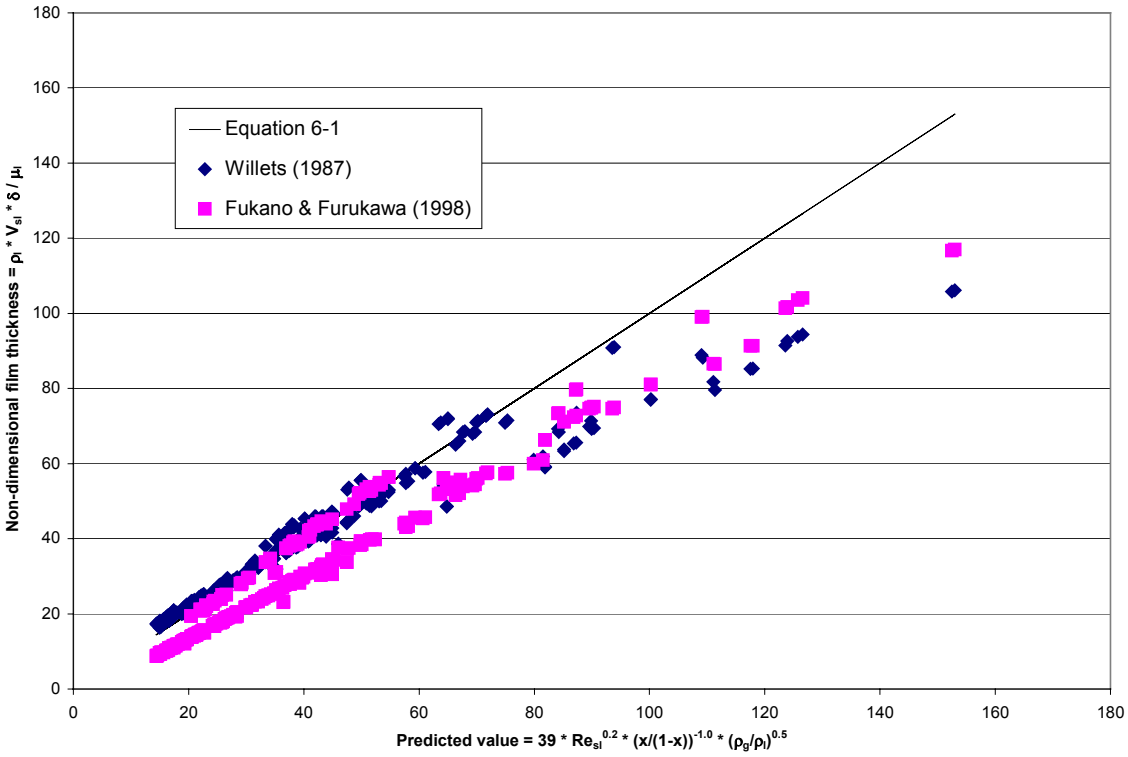

Figure 6.2. Comparison of normal gravity film thickness correlations.

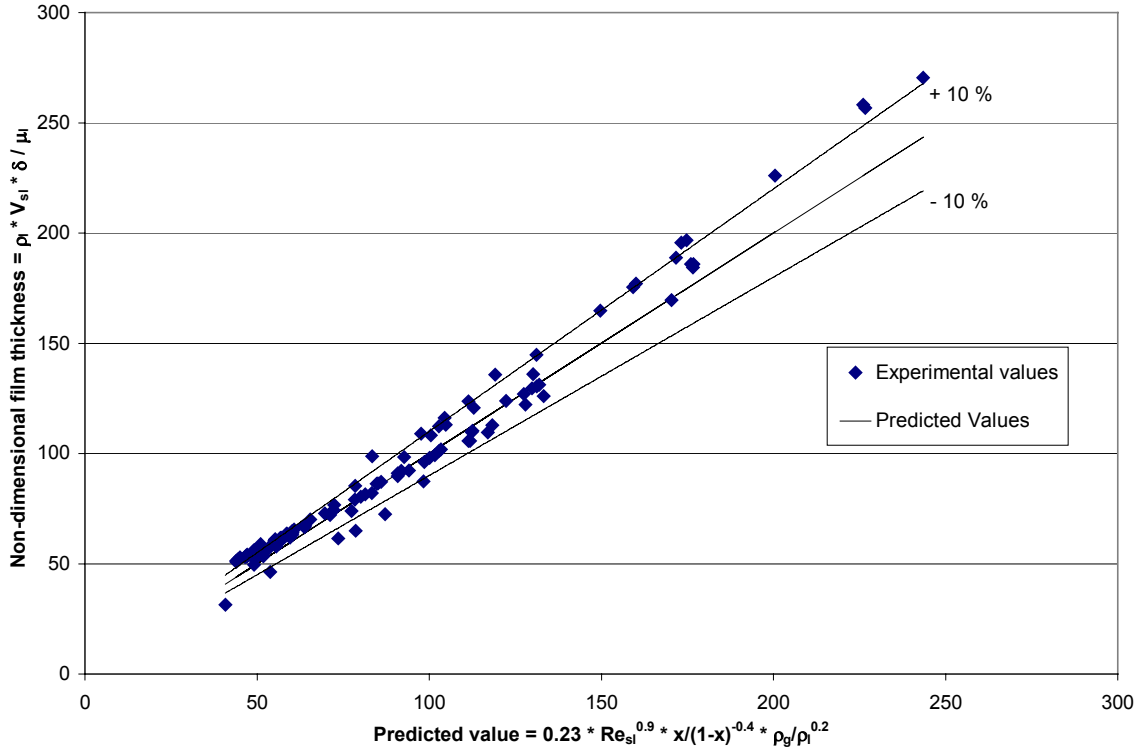

Figure 6.3. Measured and predicted non-dimensional film thickness for microgravity (equation 6-3).

The hypergravity data are plotted in Figure 6.4. The data can be represented by the equation

$$\rho_l V_{sl} \delta / \mu_l = 0.4 \, Re_{sl}^{0.8} \, (x / (1\text{-}x))^{-0.5} \, (\rho_g / \rho_l)^{0.2} \, . \qquad (6\text{-}4)$$

This equation can predict the hypergravity film thickness values to within ± 15%, as shown by the dashed lines. A summary of the average film thickness equations is shown in Table 6.1.

Table 6.1. Summary of average film thickness equations.

Gravity level	Coefficient	Exponent on Re_{sl}	Exponent on x / (1-x)	Exponent on ρ_g / ρ_l	Data scatter
Normal	39	0.2	-1.0	0.5	± 10 %
Microgravity	0.23	0.9	-0.4	0.2	± 10 %
Hypergravity	0.41	0.8	-0.5	0.2	± 15 %

Although the previous equations accurately represent the experimental data, they do not directly convey the dependence on the gas and liquid flow rates, as shown in Figures 4.1 and 4.7. From these figures, the film thickness is dependant mainly on the gas specific energy and the superficial liquid Reynolds number. The gas specific energy is represented in non-dimensional form as the gas Weber number. Figure 6.5 shows the normal gravity average film thickness based on the equation

$$\rho_l V_{sl} \delta / \mu_l = 0.047 \, Re_{sl}^{1.2} \, We_{sg}^{-0.5} \, . \qquad (6\text{-}5)$$

This equation also represents the normal gravity data to within ± 10%, however the influence of the gas and liquid properties is more obvious. The film thickness equations of this form for all gravity levels are shown in Table 6.2. From the exponents shown in the table, it can be seen that the influence of the liquid flow rate is approximately constant for all gravity levels.

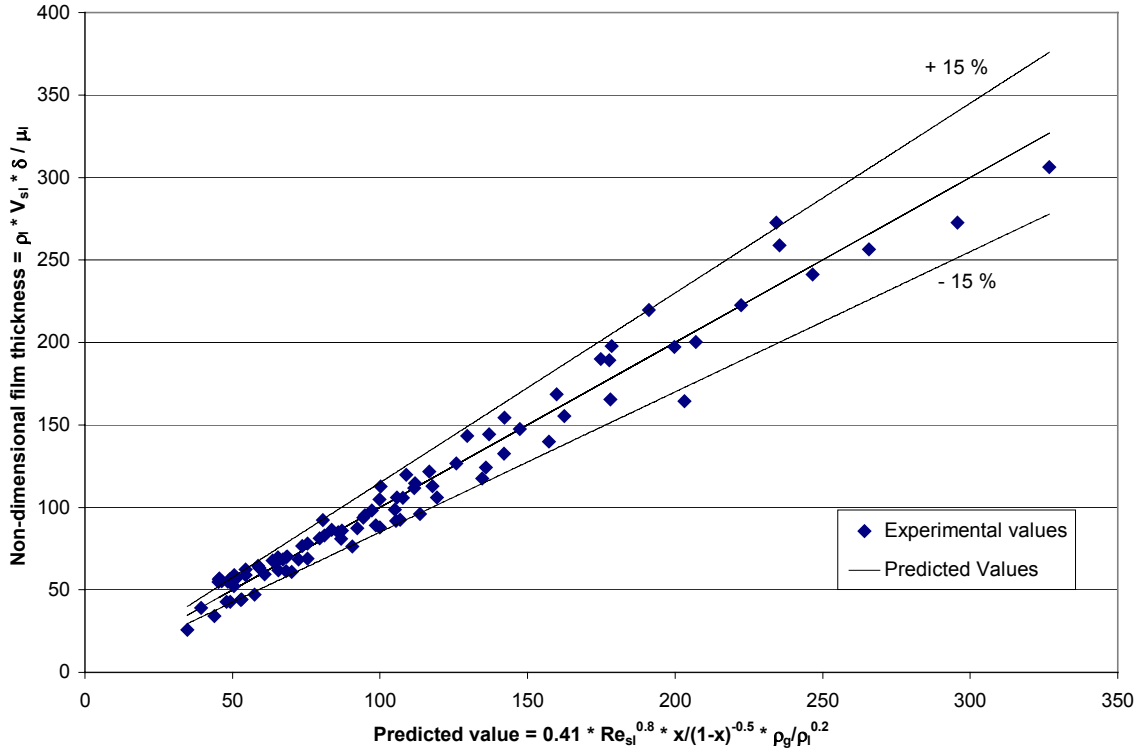

Figure 6.4. Measured and predicted non-dimensional film thickness for hypergravity (equation 6-4).

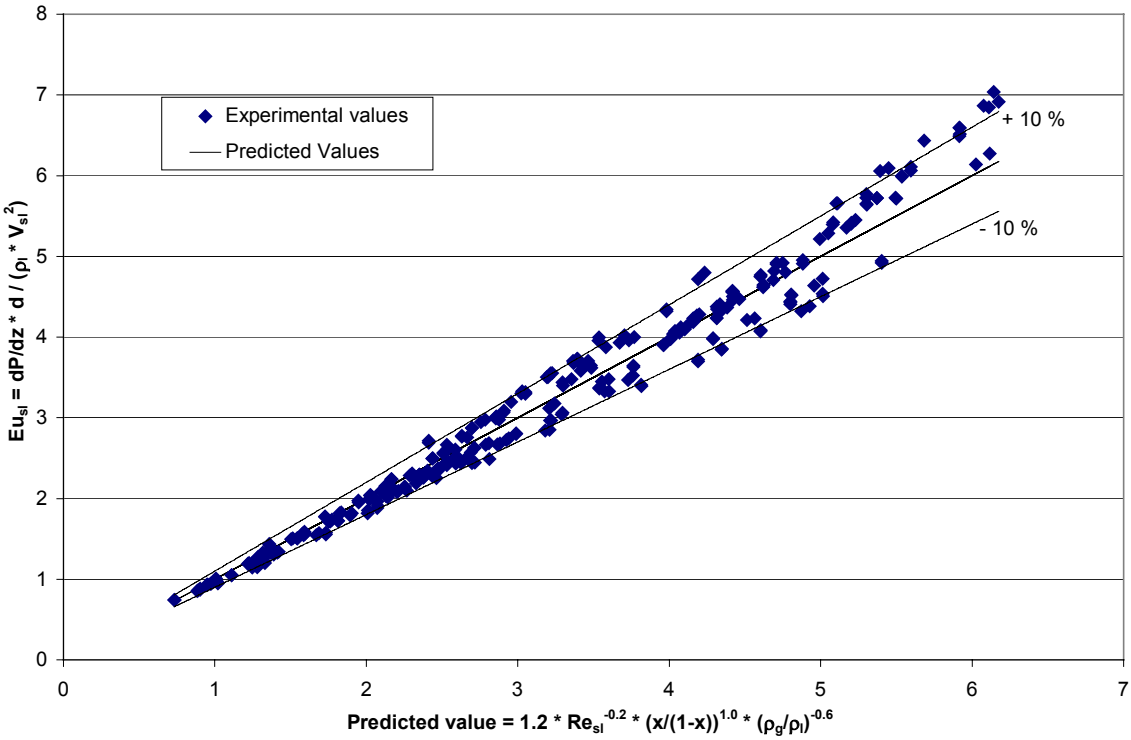

Figure 6.5. Measured and predicted non-dimensional film thickness for normal gravity (equation 6-5).

Table 6.2. Summary of average film thickness equations based on Re_{sl} and We_{sg}.

Gravity level	Coefficient	Exponent on Re_{sl}	Exponent on We_{sg}	Data Scatter
Normal	0.047	1.2	-0.5	± 10 %
Microgravity	0.016	1.3	-0.2	± 10 %
Hypergravity	0.025	1.3	-0.3	± 15 %

6.2 Pressure Drop Equations

The normal gravity non-dimensional frictional pressure drop is shown in Figure 6.6. The superficial liquid Euler number (the ratio of the pressure force to the inertia force) is calculated using equation 1-24. The predicted pressure drop is found using the same method as the film thickness equations, and for normal gravity, is calculated to be

$$dP/dz_f \, d / (\rho_l \, V_{sl}^2) = 1.20 \, Re_{sl}^{-0.2} \, (x / (1-x))^{1.0} \, (\rho_g / \rho_l)^{-0.6}. \qquad (6\text{-}6)$$

This modified equation can predict the majority of the experimental pressure drop date to within ± 10%, as shown by the light lines.

A comparison of the current frictional pressure drop, equation 6-6 and the pressure drop predicted by the Chisholm correlation is shown in Figure 6.7. The x-axis represents the new pressure drop correlation (equation 6-6), while the y-axis represents the Euler number based on the calculated pressure drop from the correlations. The majority of the current data are within about 20% of the air-water values predicted by Chisholm, assuming both phases are turbulent. This is within the approximate accuracy of most two-phase flow frictional pressure drop correlations. The predicted frictional pressure drops that are much higher than the current data set represent the results of the Chisholm correlation using the helium-water data. Due to the energy matching of the

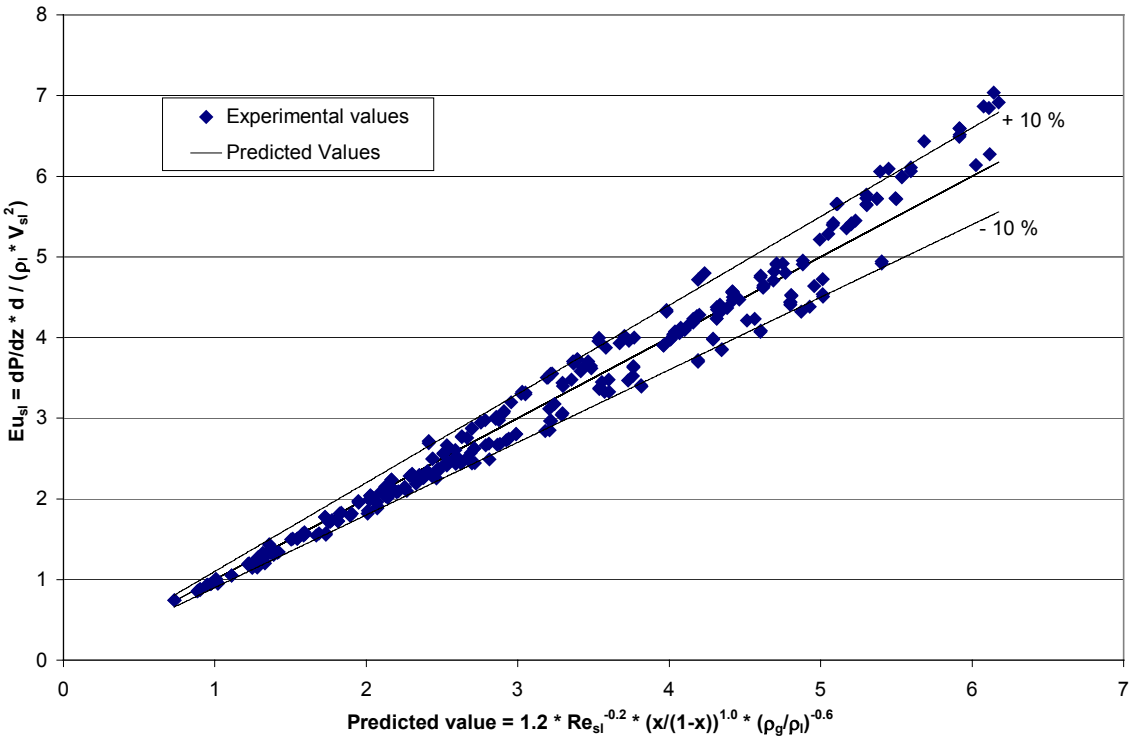

Figure 6.6. Measured and predicted non-dimensional frictional pressure drop for normal gravity (equation 6-6).

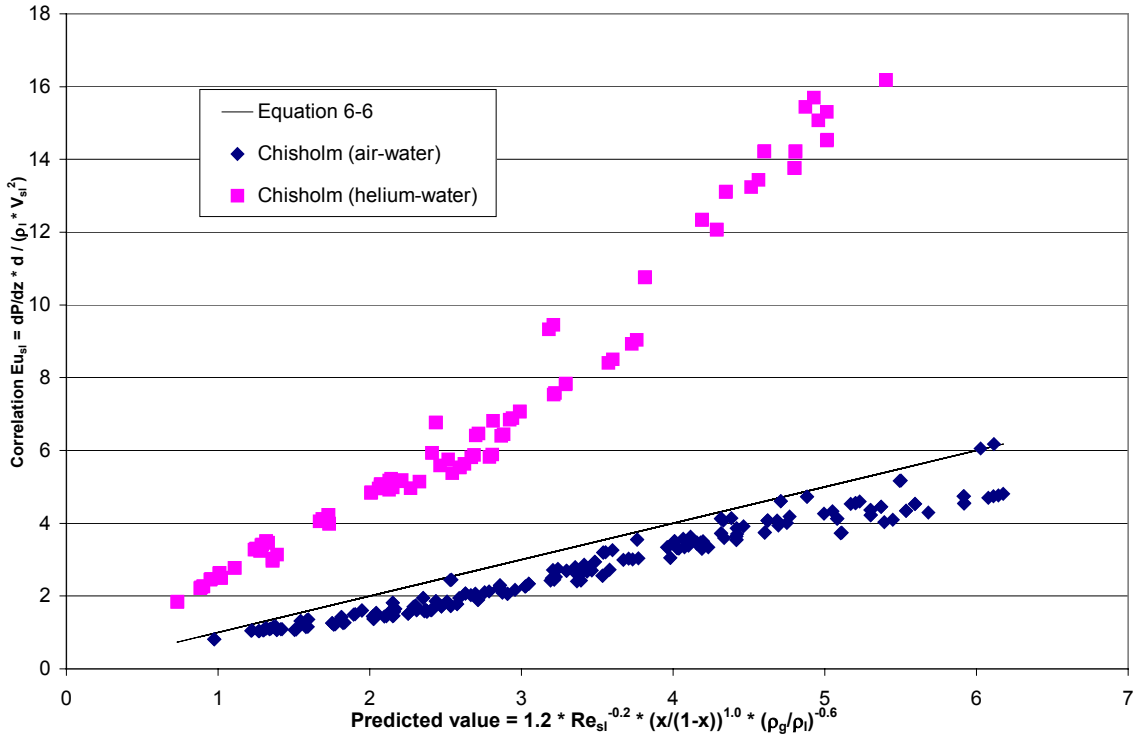

Figure 6.7. Comparison of normal gravity frictional pressure drop correlations.

gas phases, the helium is at a much lower Reynolds number compared to the air data, which corresponds to an increase in the single-phase friction factor. The single-phase friction factor is then used in the prediction of the two-phase flow pressure drop. This difference in the predicted two-phase frictional pressure drop suggests the Lockart-Martinelli-Chisholm correlation, which was developed solely based on two-phase flows with air as the gas phase, does not accurately account for the gas-liquid density ratio.

The microgravity frictional pressure drop is plotted in Figure 6.8. The microgravity data can be represented to within ± 10%, using the equation

$$dP/dz_f \, d / (\rho_l \, V_{sl}^2) = 0.96 \, Re_{sl}^{-0.1} \, (x / (1-x))^{1.3} \, (\rho_g / \rho_l)^{-0.6}, \qquad (6\text{-}7)$$

as shown by the light lines. A comparison of the newly developed equations for normal gravity and microgravity is shown in Figure 6.9. The correlation for normal gravity (equation 6-6) and for microgravity (equation 6-7) are plotted on the y-axis, with the normal gravity correlation used as the x-axis. The majority of the predicted microgravity data fall within ± 20% of the predicted frictional pressure drops of the same flow conditions at normal gravity.

The frictional pressure drop from the hypergravity data can be represented to within ± 15 % by

$$dP/dz_f \, d / (\rho_l \, V_{sl}^2) = 1.75 \, Re_{sl}^{-0.2} \, (x / (1-x))^{1.1} \, (\rho_g / \rho_l)^{-0.6}. \qquad (6\text{-}8)$$

The data and equation are plotted in Figure 6.10. A comparison of the normal gravity

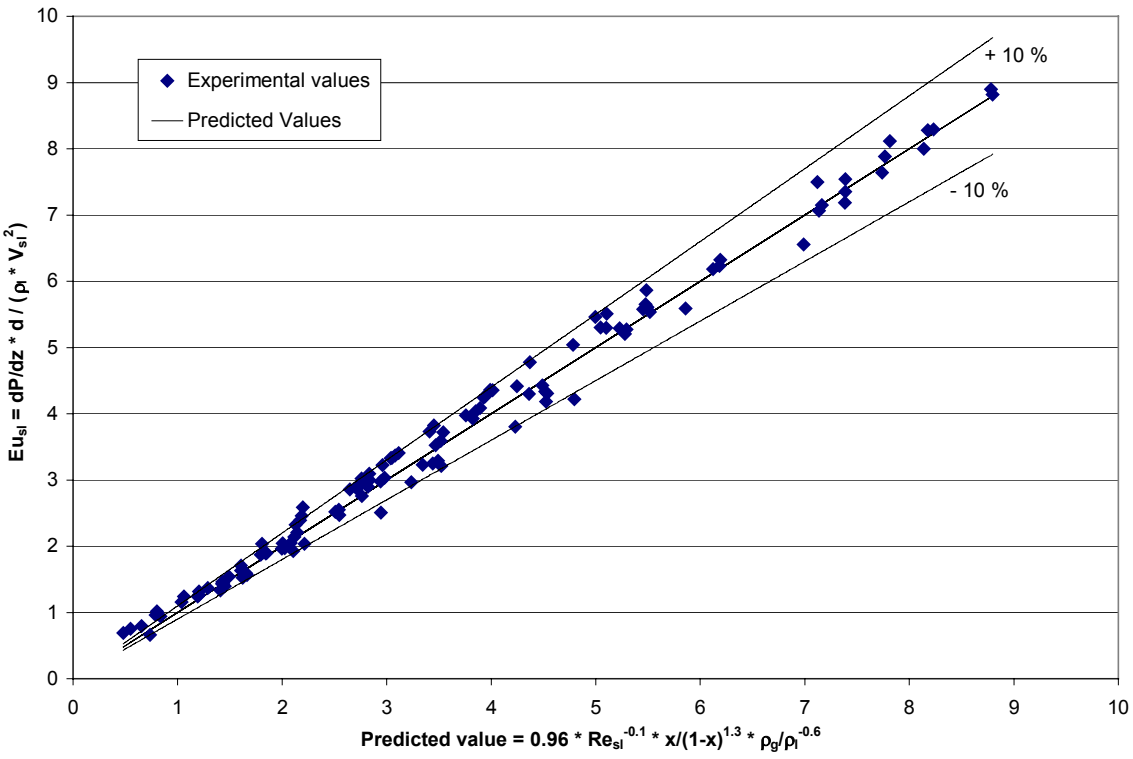

Figure 6.8. Measured and predicted non-dimensional frictional pressure drop for microgravity (equation 6-7).

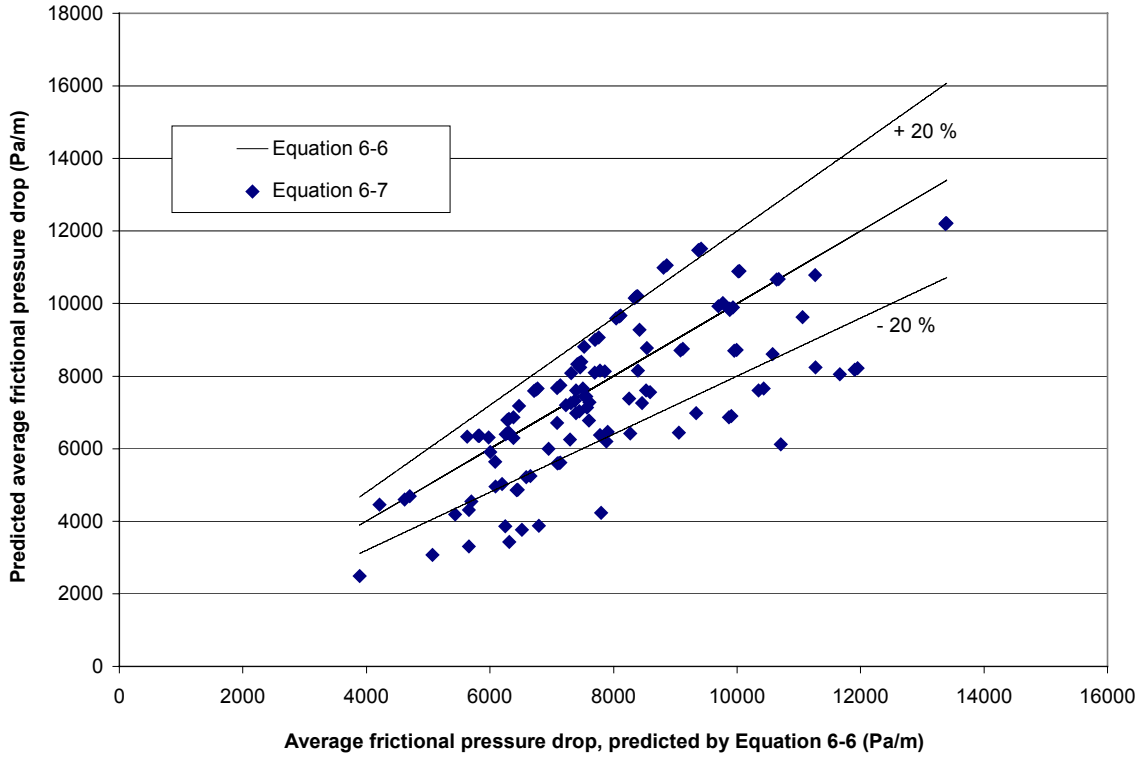

Figure 6.9. Comparison between normal and microgravity average frictional pressure drop equations.

predicted values and the hypergravity predicted values is shown in Figure 6.11. The normal gravity (equation 6-6) and hypergravity values (equation 6-8) are plotted on the y-axis, against the normal gravity values, on the x-axis. All of the hypergravity average frictional pressure drop data are larger than the normal gravity data at the same flow points. The predicted hypergravity pressure drop is larger by approximately 15 to 30 %, with an increase of 20% representing the majority of the data, as shown by the dotted line. A summary of the frictional pressure drop equations for the different gravity levels is shown in Table 6.3.

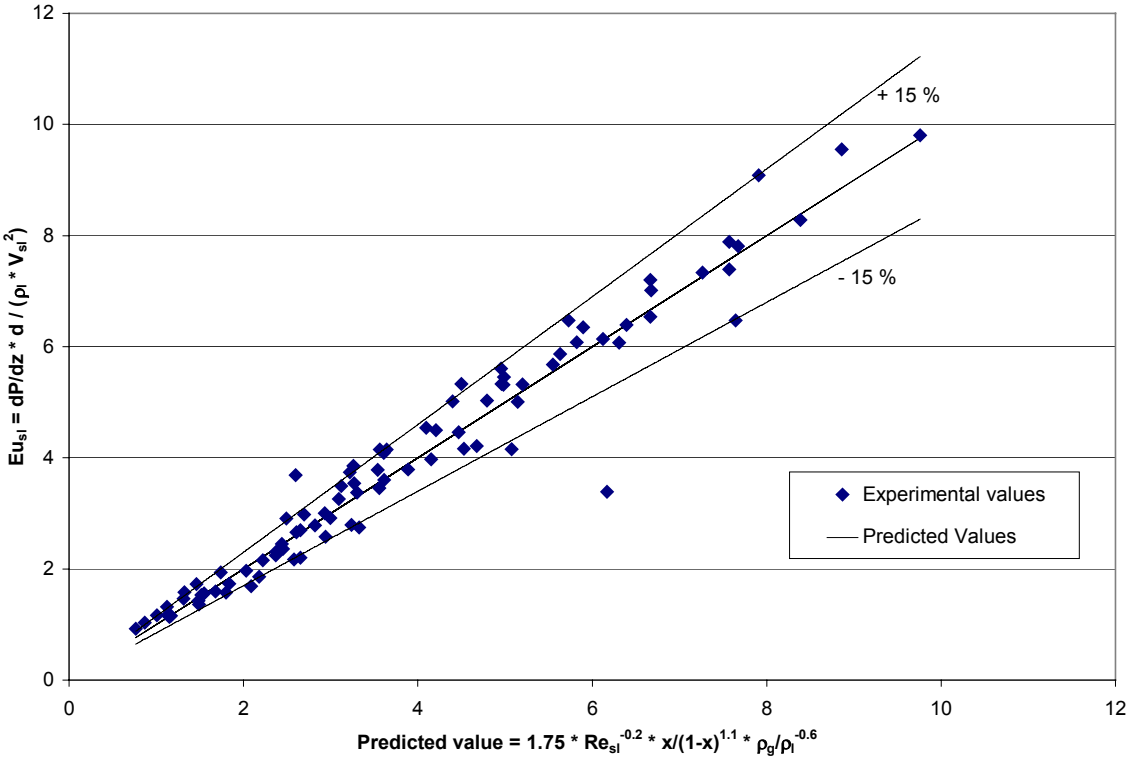

Figure 6.10. Measured and predicted non-dimensional frictional pressure drop for hypergravity (equation 6-8).

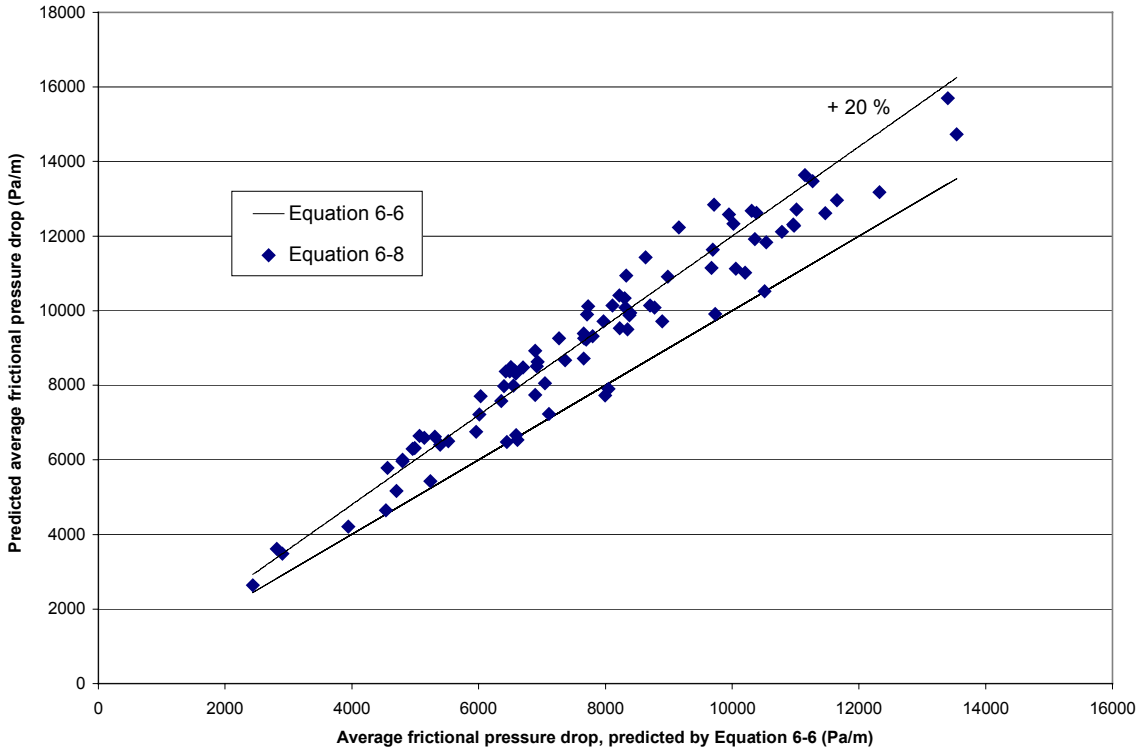

Figure 6.11. Comparison between normal and hypergravity average frictional pressure drop equations.

Table 6.3. Summary of average frictional pressure drop equations.

Gravity level	Coefficient	Exponent on Re_{sl}	Exponent on x / (1-x)	Exponent on ρ_g / ρ_l	Data scatter
Normal	1.20	-0.2	1.0	-0.6	± 10 %
Microgravity	0.96	-0.1	1.3	-0.6	± 10 %
Hypergravity	1.75	-0.2	1.1	-0.6	± 15 %

7.0 CONCLUSIONS AND RECOMMENDATIONS

This thesis presents an experimental study in the flow characteristics of annular flow. The average film thickness and the average frictional pressure drop for air-water and helium-water flows have been examined at normal gravity, microgravity, and hypergravity. Microgravity and hypergravity data were collected on board a parabolic aircraft, and normal gravity data were collected on ground to match the set points achieved on the flights. Non-dimensional equations are presented to predict the film thickness and frictional pressure drop to within ± 10 % for the normal gravity and microgravity, and to within ± 15 % for the hypergravity condition.

7.1 CONCLUSIONS

The following conclusions can be made based on the present work.

1) The film thickness increases with increasing liquid flow rate or decreasing gas flow rate at all gravity levels.
2) The average microgravity film thickness values are between two and four times larger than the average normal gravity film thickness values.
3) There is no noticeable difference in the average film thickness values for air-water and helium-water data, when plotted against the gas specific energy (density times velocity squared) and therefore, for the present data, against the

gas Weber number. For the data studied, the Weber number is directly proportional to the gas specific energy since the tube diameter and the surface tension are constant.

4) For a given gravity level, for a range of liquid mass fluxes of 75 – 199 kg/m^{2}s, the film thickness values can be represented by a power relationship based only on the gas specific Weber number.

5) The frictional pressure drop increases by increasing the liquid or gas flow rates at all gravity levels.

6) There is no noticeable difference in the average frictional pressure drop between the air-water and the helium-water data when plotted against the gas specific energy or gas specific Weber number.

7) The frictional pressure drop correlation of Lockart-Martinelli (modified by Chisholm) and developed for air-liquid flows, is not applicable to helium-water flow as it does not fully account for the change in the gas phase density.

8) The average frictional pressure drop for microgravity varies approximately within ± 20 % of the normal gravity pressure drop.

9) The average frictional pressure drop for hypergravity is approximately 20 % higher than for normal gravity.

10) For low liquid flow rates, the rate of evaporation of the liquid may be of concern.

7.2 RECOMMENDATIONS

Based on the present research, the following recommendations can be made:

1) Further research should be done to investigate the influence of the gas density on the film thickness and the frictional pressure drop, including more data using helium and with different gases, such as argon. As well, the applicability of the Lockart-Martinelli-Chisholm frictional pressure drop correlation for two-phase flows not involving air must be verified.

2) The film thickness dependence on the gas Weber number should be verified by using different combinations of gas density and surface tension.

3) The effect of other flow parameters, including tube diameter, tube material and roughness, and other gas-liquid combinations, needs to be verified on the annular flow and the correlations.

4) The present microgravity data was collected with some residual gravity levels, and the aircraft vibrations may have been transferred to the flow. The effect of the external vibration and varying direction of gravity should be examined on the annular flow, the wave generation and the flow stability.

5) Further two-phase flow studies in hypergravity should be conducted. This includes determining a flow regime map and the flow characteristics of all the flow regimes to determine the effect of variable gravity on all possible two-phase flow situations. Use of a void fraction sensor would be beneficial for an objective determination of the flow regime.

6) The amount of microgravity annular flow data is still limited. Further data should be collected to verify the current work.

7) The film thickness sensor electronics should be improved. The largest source of error in the film thickness measurements is the electronic noise present in the all-

water readings. If this is eliminated, the film thickness measurements can be improved.

8) Using the film thickness time trace data recorded by the two film thickness probes, further characteristics of the film can be examined. The wave velocity, frequency and shape can be studied.

REFERENCES

Ambrosini, W., P. Andreussi and B. J. Azzopardi. (1991). A physically based correlation for drop size in annular flow. International Journal of Multiphase Flow, Vol. 17, No. 4, pp. 497-507.

Ariyadasa, U. (2002). An Investigation of Film Thickness and Pressure in Upward and Downward Annular Two-Phase Flow. M.Sc. Thesis, Department of Mechanical Eng., University of Saskatchewan.

Ariyadasa, U. and K. S. Rezkallah. (2001). An Investigation of Pressure and Film Thickness in Co-Current Annular Upward and Downward Two-Phase Flow. Proc. Of 4th International Multiphase Flow Conference, paper no. 476 (cd).

Asali, J. C., T. J. Hanratty, and P. Andreussi. (1985). Interfacial Drag and Film Height for Veritcal Annular Flow. AIChE Journal, Vol. 31, No. 6, pp. 895-902.

Azzopardi, B. J. (1986). Disturbance Wave Frequencies, Velocities and Spacing in Vertical Annular Two-Phase Flow. Nuclear Engineering and Design, Vol. 92, pp. 121-133.

Azzopardi, B. J. and P. B. Whalley. (1980). Artificial Waves in Annular Two-Phase Flow. HDL-TR Basic Mechanisms in Two-Phase Flow and Heat Transfer, Presented at the ASME Winter Annual Meeting, ASME New York, pp. 1-8.

Barbosa, J. R., Jr., G. F. Hewitt, G. Konig, S. M. Richardson. (2002). Liquid entrainment, droplet concentration and pressure gradient at the onset of annular flow in a vertical pipe. International Journal of Multiphase Flow, Vol. 28, No. 6, pp. 943-961.

Bousman, W. S. (1995). Studies of Two-Phase Gas Liquid Flow in Microgravity. NASA Contractor Report 195434, also Ph.D. Dissertation, University of Houston, 1994.

Bousman, W. S., J. B. McQuillen, and L. C. Witte. (1996). Gas-liquid flow patterns in microgravity: effects of tube diameter, liquid viscosity and surface tension. International Journal of Multiphase Flow, Vol. 22, No. 6, pp. 1035-1053.

Brauner, N. (1991). Two-phase liquid-liquid annular flow. International Journal of Multiphase Flow, Vol. 17, No. 1, pp. 59-76.

Chen, I., R. Downing, E. Keshock, and M. Al-Sharif. (1991). Measurements and Correlation of Two-Phase Pressure Drop Under Microgravity Conditions. Journal of Thermophysics and Heat Transfer, Vol. 5, No. 4, pp. 514-523.

Chen, I. Y., K.-S. Yang. Y.-J. Chang and C.-C. Wang. (2001). Two-phase pressure drop of air-water and R-410A in small horizontal tubes. International Journal of Multiphase Flow, Vol. 27, No. 7, pp. 1293-1299.

Chisholm, D. (1973). Pressure gradients due to friction due to the flow of evaporating two-phase mixtures in smooth tubes and channels. International Journal of Heat and Mass Transfer, Vol. 16, pp. 347-358.

Coleman, H. W. and W. G. Steele. (1999). Experimentation and Uncertainty Analysis for Engineers, 2nd Ed. John Wiley & Sons, New York.

Colin, C., J. A. Fabre, and A. E. Dukler. (1991). Gas-Liquid Flow at Microgravity Conditions – 1. Disbursed Bubble and Slug Flow. International Journal of Multiphase Flow, Vol. 17, pp. 533-544.

de Jong, P. A., (1999). "An Investigation of Film Structure and Pressure Drop in Microgravity Annular Flow", M. Sc. Thesis, University of Saskatchewan, Saskatoon.

Dukler, A. E., J. B. Fabre, J. B. McQuillen, and R. Vernon. (1988). Gas-liquid flow at microgravity conditions: flow patterns and their transitions. International Journal of Multiphase Flow, Vol. 14, No. 4, pp. 389-400.

Durand, A., R. Hertz, D. Mitchell, and Rezkallah, K., 1990 (May). "The Design and Analysis of a Modular Microgravity Test Platform for use Aboard the NASA KC-135 Aircraft", *presented at the 2nd Canadian Workshop Experimentation Conference,* Ottawa.

Elkow, K. (1995). Void fraction measurement and analysis at normal gravity and microgravity conditions. M. Sc. Thesis, Department of Mechanical Engineering, University of Saskatchewan, Canada.

Fu, F. and J. F. Klausner. (1997). A Separated Flow Model for Predicting Two-Phase Pressure Drop and Evaporative Heat Transfer for Vertical Annular Flow. International Journal of Heat and Fluid Flow, Vol. 18, pp. 541-549.

Fujii, T., T Nakazawa, H. Asano, H. Yamada, and T. Yoshiyama. (1998). Flow Characteristics of Gas-Liquid Two-Phase Annular Flow Under Microgravity (Experimental Results Utilizing a Drop Tower). JSME International Journal, Series B, Vol. 41, No. 3, pp. 561-567.

Fukano, T. and T. Furukawa. (1998). Prediction of the effects of liquid viscosity on interfacial shear stress and frictional pressure drop in vertical upward gas-liquid annular flow. Int. J. Multiphase Flow, Vol. 24. No. 4, pp. 587-603.

Furukawa, T. and T. Fukano. (2001). Effects of liquid viscosity on flow patterns in vertical upward gas-liquid two-phase flow. International Journal of Multiphase Flow, Vol. 27, No. 6, pp. 1109-1126.

Henstock and Hanratty. (1976). The Interfacial Drag and the Height of the Wall Layer in Annular Flows. AIChE Journal, Vol. 22, no. 6, pp. 990-1000.

Heppner, D. B., C. D. King and J. W. Littles. (1975). Zero-gravity experiments in two-phase fluid flow regimes. Presented at the ICES Conf., San Francisco, Calif., ASME Paper No. 75-ENAs-24.

Hill, D., S. Downing, D. Rogers, D. Teske and R. Niggemann. (1987). A Study of Two-Phase Flow in a Reduced Gravity Environment. Final Report DRL No. T-1884, Sunstrand Energy Systems, Rockford, Ill.

Hori, K., M. Nakazatomi, K. Nishikawa, and K. Sekoguchi. (1979). On Ripple of Annular Two-Phase Flow – 3 Effect of Liquid Viscosity on Characteristics of Wave and Inter-Facial Friction Factor. JSME Bulletin, Vol. 22, No. 169, pp. 952-959.

Huckerby, C. S. (1992). Two-phase liquid-gas flow pattern abservations under microgravity conditions. M. Sc. Thesis, Department of Mechanical Engineering, University of Saskatchewan, Canada.

Iguchi, M. and Y. Terauchi. (2001). Boundaries among bubbly and slug flow regimes in air-water two-phase flows in vertical pipe of poor wettability. International Journal of Multiphase Flow, Vol. 27, No. 4, pp. 729-735.

Ishii, M. and K. Mishima. (1989). Droplet entrainment correlation in annular two-phase flow. International Journal of Heat and Mass Transfer, Vol. 32. No. 10, pp. 1835-1846.

Jepson, D. M., B. J. Assopardi and P. B. Whalley. (1989). The effect of gas properties on drops in annular flow. International Journal of Multiphase Flow, Vol. 15, No. 3, pp. 327-339.

Keshock, E. G. and C. S. Lin. (1996). Two-Phase Annular Flow in Helical Coil Flow Channels in a Reduced Gravity Environment. Proceedings of the 1996 3rd Microgravity Fluid Physics Conference, NASA Conference Publication, No. 3338, pp. 115-120.

Klausner, J. F., B. T. Chao and S. L. Soo. (1991). An improved correlation for two-phase frictional pressure drop in boiling and adiabatic downflow in the annular flow regime. Proceedings of the Institution of Mechanical Engineers, Part C: Mechanical Engineering Science, Vol. 205, No. C5, pp. 317-328.

Kosky. (1971). Thin Liquid Films Under Simultaneous Shear and Gravity Forces. International Journal of Heat and Mass Transfer, Vol. 14, pp. 1220-1224.

Laurinat, J. E., T. J. Hanratty and J. C. Dallman. (1984). Pressure drop and film height measurements for annular gas-liquid flow. International Journal of Multiphase Flow, Vol. 10, No. 3, pp. 341-356.

Lockart, R. W. and R. C. Martinelli. (1949). Proposed correlation of data of isothermal two-phase, two component flow in pipes. Chem. Engng. Prog., 45, pp. 39-48.

Lopez de Bertodano, M. A., A. Assad, and S. G. Beus. (2001). Experiments for entrainment rate of droplets in the annular regime. International Journal of Multiphase Flow, Vol. 27, No. 4, pp. 685-699.

Lowe, D. C. (1997). A study on flow regime identification in microgravity gas-liquid flows using a capacitance sensor. M. Sc. Thesis, Department of Mechanical Engineering, University of Saskatchewan, Canada.

Lowe, D. C. and K. S. Rezkallah. (1999). Flow regime identification in microgravity two-phase flows using void fraction signals. International Journal of Multiphase Flow, Vol. 25. pp 433-457.

Matsui, G. (1984). Identification of flow regimes in vertical gas-liquid two-phase flow using differential pressure fluctuations. International Journal of Multiphase Flow, Vol. 10, No. 6, pp. 711-720.

Mori, K., Y. Kondo, M. Kaji, and T. Yagishita. (1999). Effects of Liquid Viscosity on Characteristics of Waves in Gas-Liquid Two-Phase Flow (Characteristics of Huge Waves and Disturbance Waves). JSME International Journal, Series B, Vol. 42, No. 4, pp. 658-666.

Novespace, 1999 (July). "Parabolic Flight with A300 Zero-G – User's Manual", Ed. 5.2, Paris.

Pan, L. and T. J. Hanratty. (2002). Correlation of entrainment for annular flow in vertical pipes. International Journal of Multiphase Flow, Vol. 28, No. 3, pp. 363-384.

Reinarts, T. R. (1993). Adiabatic two phase flow regime data and modeling for zero and reduced (horizontal flow) acceleration fields. Ph. D. dissertation, Texax A&M University, U.S.A.

Rezkallah, K. S. (1988). Two-Phase Flow and Heat Transfer at Reduced Gravity: A Literature Survey". Proc. American Nuclear Soc., Vol. 3, pp. 435-444.

Rezkallah, K. S. (1990). A Comparison of Existing Flow Pattern Predictions During Forced-Convective Two-Phase Flow Under Microgravity Conditions. International Journal of Multiphase Flow, Vol. 16, No. 2, pp. 243-259.

Rezkallah, K. S. (1996). Weber number based flow-pattern maps for liquid-gas flows at microgravity. International Journal of Multiphase Flow, Vol. 22, No. 6, pp. 1265-1270.

Rite, R. W. (1995). Heat transfer in gas-liquid flows through a vertical, circular tube under microgravity conditions. Ph. D. Dissertation, Department of Mechanical Engineering, University of Saskatchewan, Canada.

Rite, R. W. and K. S. Rezkallah. (1993). An investigation of transient effects on heat transfer measurements in two-phase, gas-liquid flows under microgravity conditions. HTD-Vol. 235, Heat Transfer in Microgravity Systems. S. S. Sadhal and A. Hashemi, editors.

Sridhar, K. R., B. T. Chao, S. L. Soo. (1992). Pressure drop in fully developed, turbulent, liquid-vapour annular flows in zero gravity. AIAA Journal, Vol. 30, No. 4, pp. 1016-1026.

Vassallo, P. F., T. A. Trabold, R. Kumar, and D. M. Considine. (2001). Slug-to-annular regime transitions in R-134a flowing through a vertical duct. International Journal of Multiphase Flow, Vol. 27, No. 1, pp. 119-145.

Whalley, P. B. (1987). Boiling, Condensation and Gas-Liquid Flow. Oxford University Press, New York.

Whalley, P. B. (1996). Two-Phase Flow and Heat Transfer. Oxford University Press, New York.

White, F. M. (1994). Fluid Mechanics, 3rd Ed. McGraw-Hill, Inc. Toronto.

Willets, I. P. (1987). Non-aqueous annular two-phase flow. D. Phil. Thesis, Univ. of Oxford, U. K.

Witte, L. C., W. S. Bousman and L. B. Fore, (1996). "Studies of Two-Phase Flow Dynamics and Heat Transfer at Reduced Gravity Conditions", NASA Contractor Report 198459.

Wolf, A., S. Jayanti and G. F. Hewitt. (2001). Flow development in vertical annular flow. Chemical Engineering Science, Vol. 56, No. 10, pp. 3221-3235.

Wu, Haojiang, F. Zhou, and Y. Wu. (2001). Intelligent identification system of flow regime of oil-gas-water multiphase flow. International Journal of Multiphase Flow, Vol. 27, No. 3, pp. 459-475.

Yang, C.-Y. and C.-C. Shieh. (2001). Flow pattern of air-water and two-phase R-134a in small circular tubes. International Journal of Multiphase Flow, Vol. 27, No. 7, pp. 1163-1177.

Zhao, J. F., J. C. Xie, H. Lin, W. R. Hu, A. V. Ivanov, A. Yu. Belyaev. (2001). Experimental studies on two-phase flow patterns aboard the Mir Space Station. International Journal of Multiphase Flow, Vol. 27, No. 11, pp. 1931-1944.

Zhao, L. and K. S. Rezkallah. (1993). Gas-liquid flow patterns at microgravity conditions. International Journal of Multiphase Flow, Vol. 19, No. 5, pp. 751-763.

Zhao, T. S. and Q. C. Bi. (2001). Co-current air-water two-phase flow patterns in vertical triangular microchannels. International Journal of Multiphase Flow, Vol. 27, No. 5, pp. 765-782.

Zhu, Zhenfeng. (2004). A study of the interfacial features of gas-liquid annular two-phase flow. M. Sc. Thesis, Department of Mechanical Engineering, University of Saskatchewan, Canada.

APPENDIX A: INSTRUMENT CALIBRATION

The calibration graphs and equations of the equipment used for the data collection are presented in the following sections. All equipment was calibrated prior to each flight campaign and the ground data collection. As well, the calibrations were checked periodically during the data collection procedure.

A.1 GAS FLOW RATE

The gas mass flow rate was measured using a MKS 200 SLM gas mass flow controller, calibrated for the flow of both air and helium. Figure A.1 shows the calibration of the MKS gas flow meter for the flow of air. Figure A.2 shows the calibration of the MKS gas flow meter with helium.

A.2 LIQUID FLOW RATE

The liquid mass flow rate was measured using an Omega FTB601 turbine flow meter. The calibration of the liquid flow meter is shown in Figure A.3.

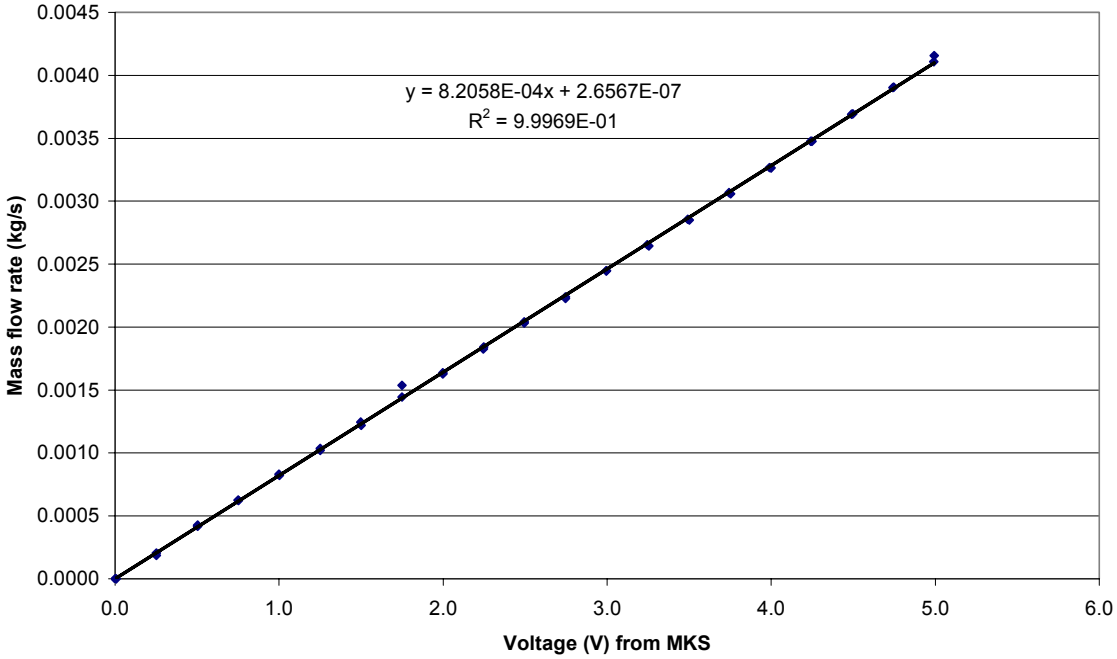

Figure A.1. Calibration of air mass flow rate.

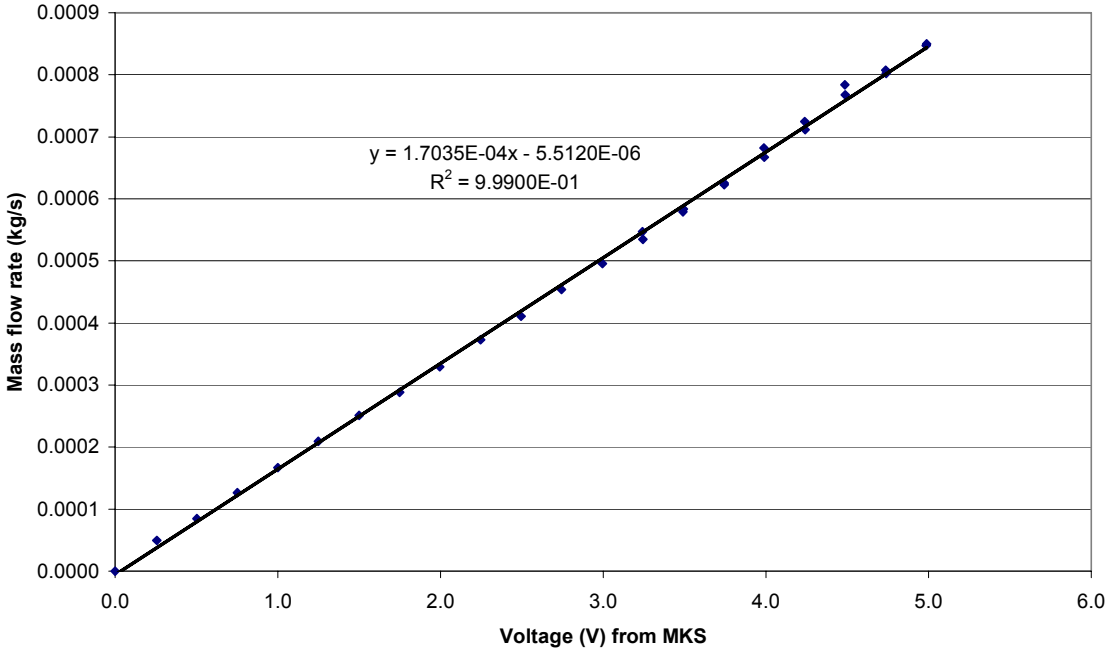

Figure A.2. Calibration of helium mass flow rate.

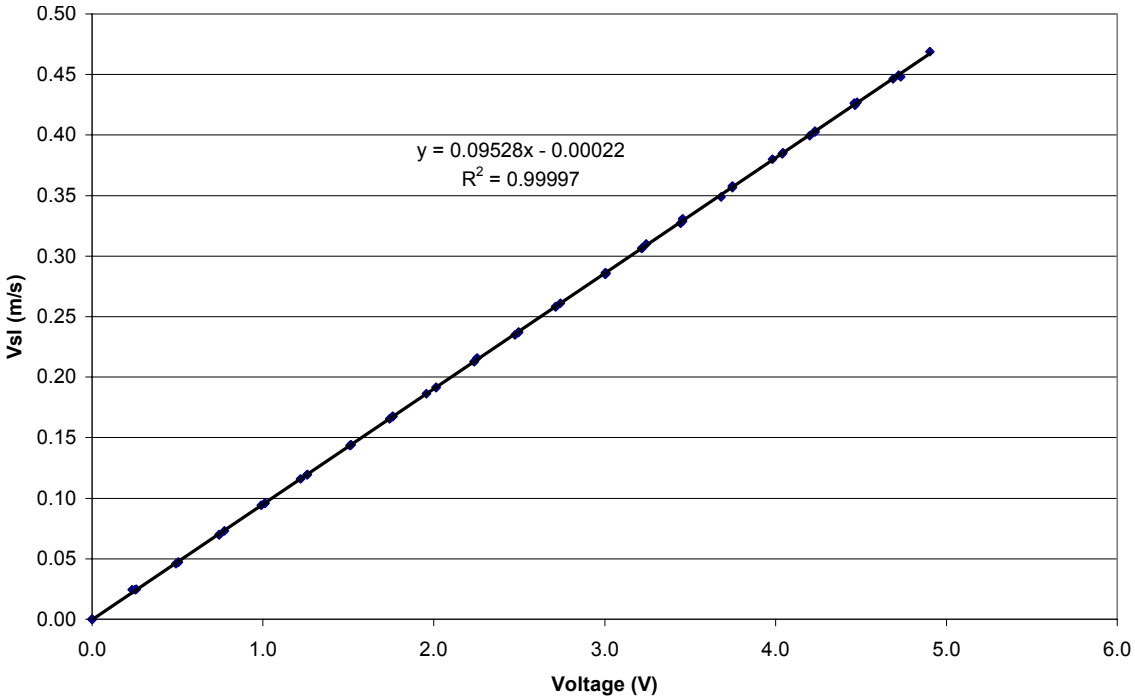

Figure A.3. Calibration of FTB601 liquid flow meter.

A.3 DIFFERENTIAL PRESSURE

The differential pressure was measured using a Validyne ± 13.8 kPa diaphragm type pressure transducer. Figure A.4 shows the calibration of the differential pressure transducer.

A.4 ABSOLUTE PRESSURE

The system pressure is measured in two locations; in the all-water flow prior to the heat exchanger and flow venturies, and in the test section of the two-phase flow mixture. The all-water flow pressure is measured using an Omega gauge pressure transducer, measured in reference to the surrounding air. The calibration equation for the all-water

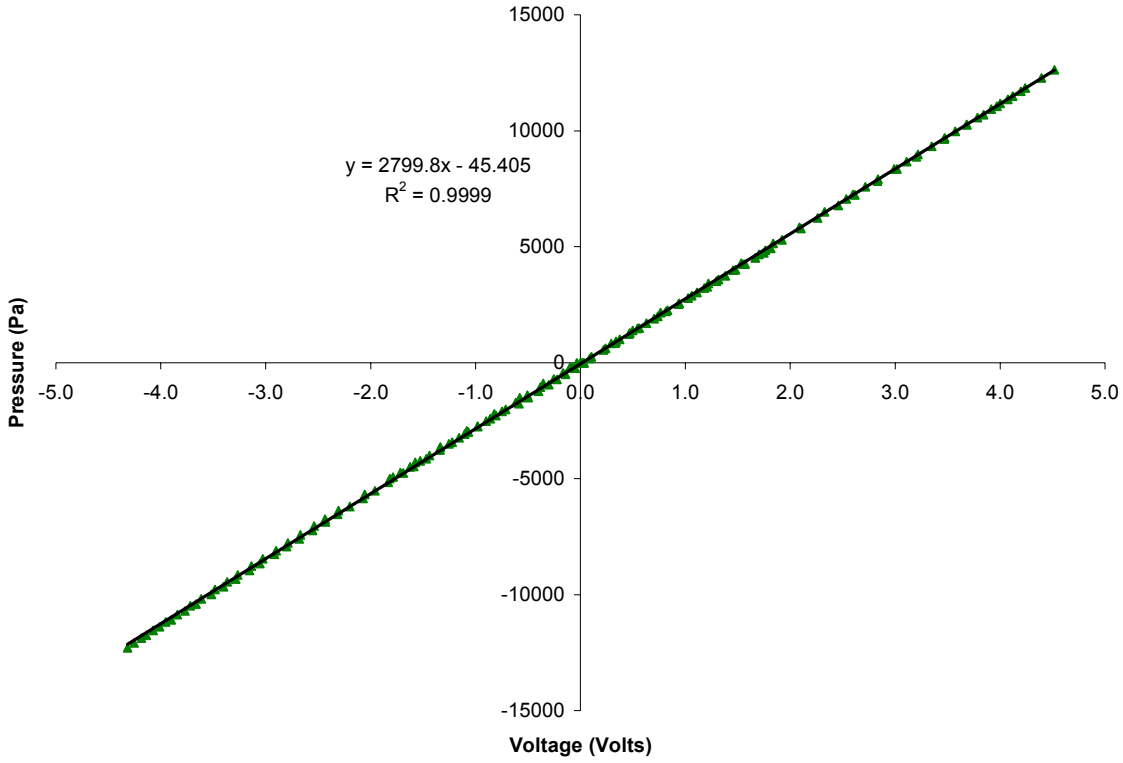

Figure A.4. Calibration of Validyne differential pressure transducer.

(gauge) system pressure is shown in Figure A.5. The two-phase pressure is measured using an Omega absolute pressure transducer, with the calibration shown in Figure A.6.

A.5 FILM THICKNESS

The liquid film thickness is calculated by normalizing the voltage output of the film thickness sensor. The normalization equation is:

$$V^* = \frac{V - V_a}{V_w - V_a}, \qquad \text{(A-1)}$$

where V* is the normalized voltage, V is the two-phase voltage recorded by the film thickness sensor, V_a is the all-air voltage reading, and V_w is the all-water voltage reading. The all-air readings are taken when the system is completely dry, and the all-

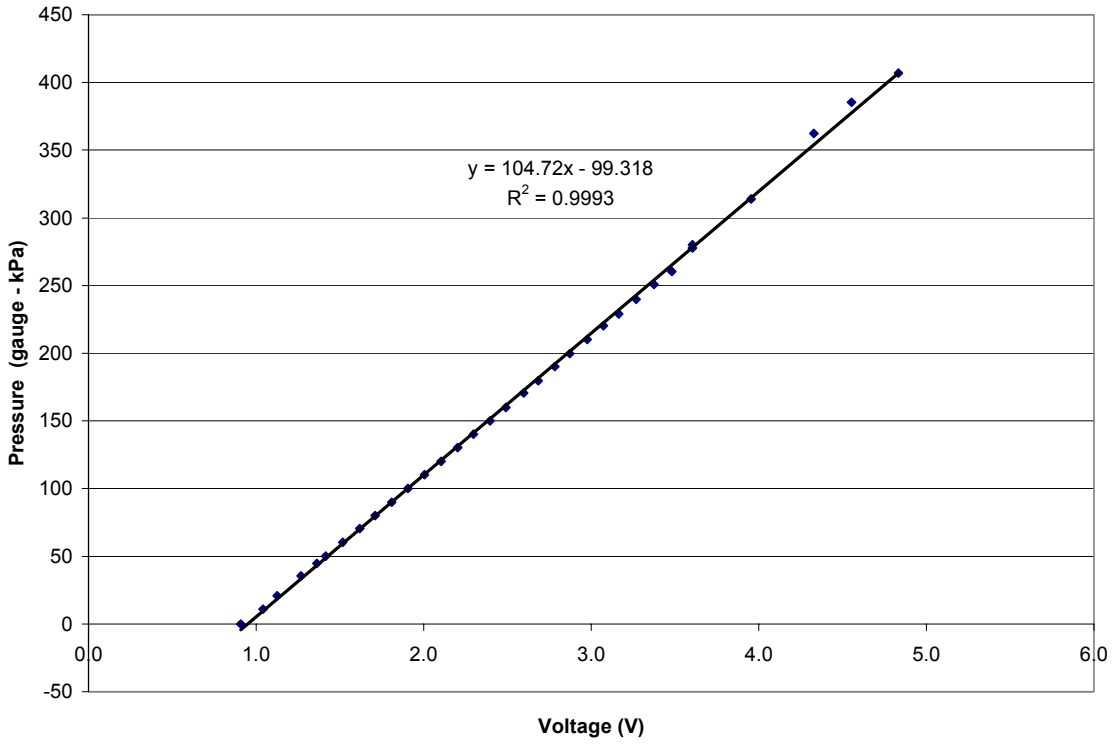

Figure A.5. Calibration of Omega gauge pressure transducer.

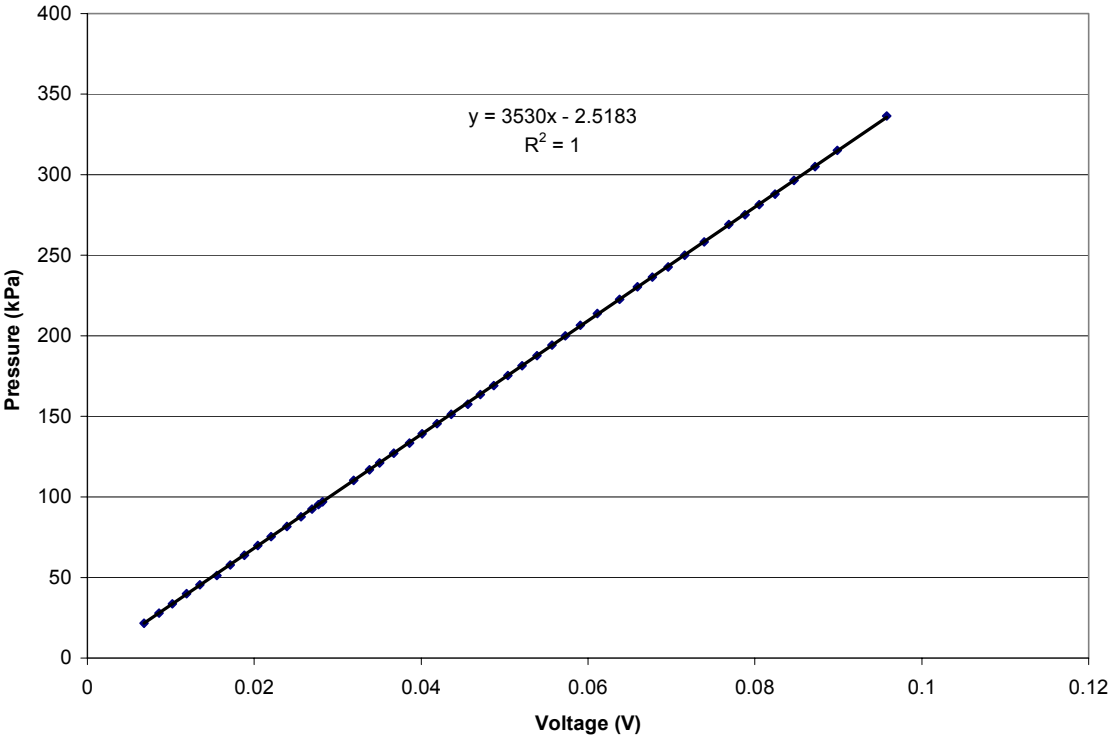

Figure A.6. Calibration of Omega absolute pressure transducer.

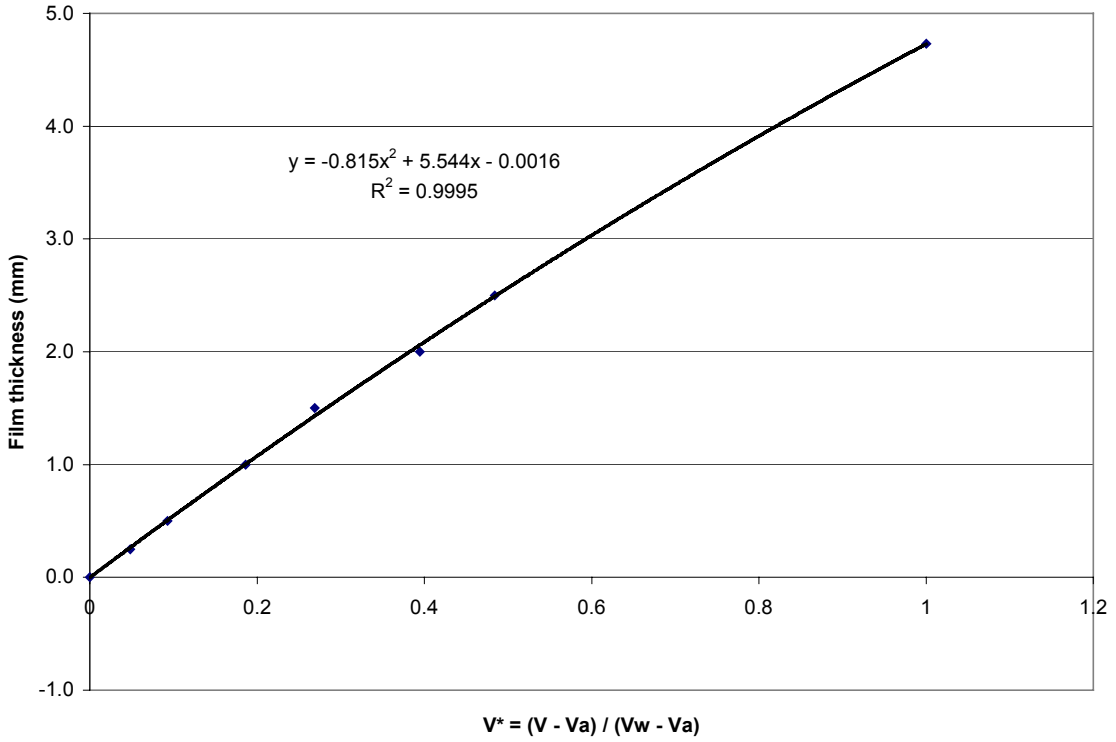

Figure A.7. Calibration of film thickness sensor.

water readings are taken when only water is flowing in the experimental loop. The resulting calibration equation for the film thickness and the normalized voltage is shown in Figure A.7.

A.6 SYSTEM TEMPERATURE

The system temperature is measured using Type T (Copper – Constantine) thermocouples. In order to record the small output of the thermocouples on the data acquisition system, the signal is amplified. The calibration equation for the thermocouple amplifier is shown in Figure A.8. After the amplified signal is read, the calibration equation is applied to return the signal to the correct thermocouple output, which is then converted to the temperature based on the Type T thermocouple.

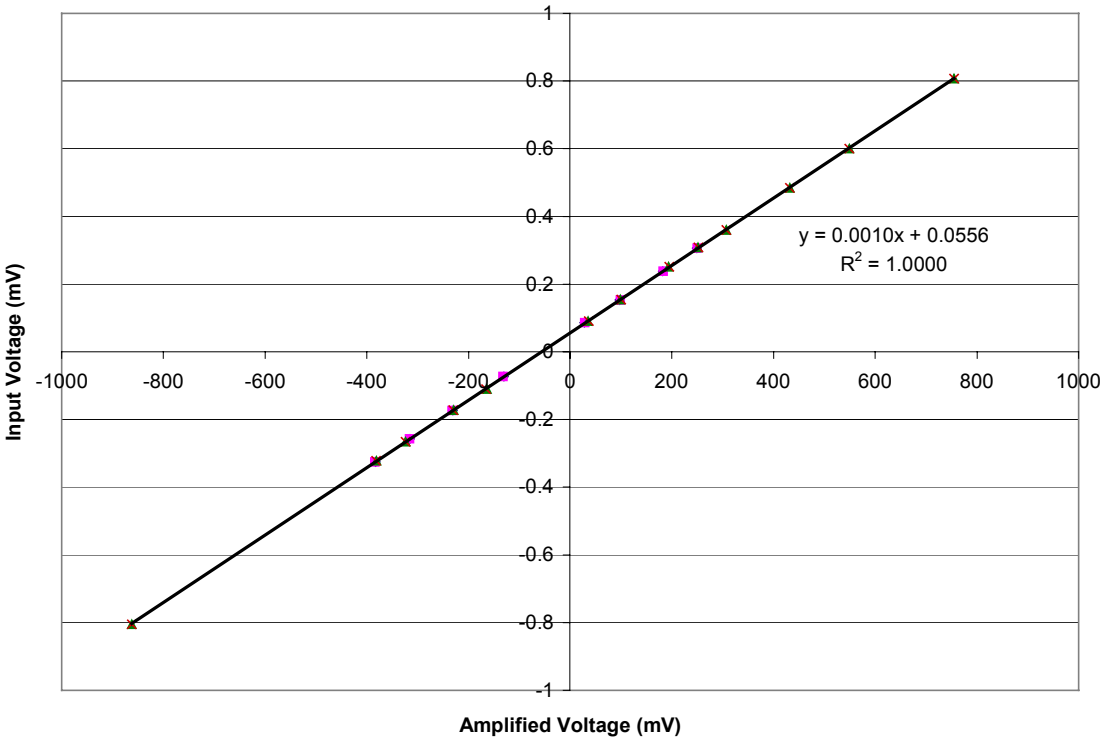

Figure A.8. Calibration equation for thermocouple amplifier.

APPENDIX B: AIR-WATER DATA

The air-water data collected during this investigation is presented in the following sections.

B.1 AIR-WATER NORMAL GRAVITY DATA

Vsl (m/s)	$\dot{m}_g$ (kg/s)	Pabs (kPa)	Ave. film height (mm)	ρ_{gas} (kg/m^3)	$\Delta P/\Delta z$, fric (Pa/m)	Vsg (m/s)	Specific Energy (J/m^3)	G_l (kg/m^{2}s)	G_g (kg/m^{2}s)
0.076	0.001474	109.9	0.234	1.306	2967	15.8	328	75.8	20.7
0.076	0.001474	109.9	0.241	1.306	2976	15.8	328	75.8	20.7
0.081	0.001972	101.7	0.168	1.209	4314	22.9	634	80.8	27.7
0.082	0.001972	101.7	0.169	1.209	4324	22.9	634	81.8	27.7
0.092	0.001806	99.1	0.191	1.178	4354	21.5	545	91.8	25.3
0.092	0.001806	99.1	0.192	1.178	4392	21.5	545	91.8	25.3
0.093	0.002134	105.2	0.170	1.250	5190	24.0	717	92.8	29.9
0.093	0.002134	105.0	0.168	1.248	5180	24.0	719	92.8	29.9
0.097	0.001683	97.4	0.210	1.158	4174	20.4	482	96.8	23.6
0.097	0.001683	97.4	0.211	1.158	4178	20.4	482	96.8	23.6
0.099	0.001764	98.5	0.199	1.171	4483	21.1	523	98.8	24.8
0.100	0.001764	98.5	0.197	1.171	4507	21.1	523	99.8	24.8
0.101	0.001829	119.0	0.220	1.414	4173	18.1	466	100.8	25.7
0.101	0.001829	118.9	0.219	1.413	4166	18.2	466	100.8	25.7
0.102	0.001018	92.7	0.359	1.102	2904	13.0	185	101.8	14.3
0.102	0.001018	92.3	0.333	1.097	2848	13.0	186	101.8	14.3
0.103	0.001559	95.5	0.231	1.135	4036	19.3	422	102.8	21.9
0.103	0.001559	95.5	0.230	1.135	4048	19.3	422	102.8	21.9
0.103	0.002369	110.8	0.163	1.317	6061	25.2	839	102.8	33.2
0.104	0.001821	109.2	0.224	1.298	4505	19.7	503	103.8	25.6
0.104	0.001821	109.1	0.225	1.297	4513	19.7	504	103.8	25.6
0.104	0.002369	110.8	0.164	1.317	6070	25.2	839	103.8	33.2
0.104	0.002389	111.2	0.163	1.322	6136	25.4	850	103.8	33.5
0.104	0.002389	111.2	0.161	1.322	6124	25.4	850	103.8	33.5
0.107	0.002142	106.7	0.187	1.268	5537	23.7	713	106.8	30.1
0.107	0.002142	106.6	0.188	1.267	5575	23.7	713	106.8	30.1
0.107	0.002142	106.6	0.190	1.267	5564	23.7	713	106.8	30.1
0.107	0.002424	113.1	0.162	1.344	6338	25.3	861	106.8	34.0
0.108	0.002424	113.1	0.165	1.344	6371	25.3	861	107.8	34.0

Vsl (m/s)	$\dot{m}_g$ (kg/s)	Pabs (kPa)	Ave. film height (mm)	ρ_{gas} (kg/m^3)	$\Delta P/\Delta z$, fric (Pa/m)	Vsg (m/s)	Specific Energy (J/m^3)	G_l (kg/m^{2}s)	G_g (kg/m^{2}s)
0.108	0.003111	129.3	0.141	1.537	7932	28.4	1240	107.8	43.7
0.108	0.003111	129.2	0.140	1.536	7962	28.4	1241	107.8	43.7
0.109	0.002258	106.6	0.172	1.267	5982	25.0	793	108.8	31.7
0.109	0.002725	119.5	0.151	1.420	7123	26.9	1030	108.8	38.2
0.109	0.002725	119.5	0.148	1.420	7122	26.9	1030	108.8	38.2
0.109	0.00338	136.8	0.128	1.626	8758	29.2	1384	108.8	47.4
0.109	0.003384	135.9	0.125	1.615	8609	29.4	1396	108.8	47.5
0.110	0.00164	98.1	0.237	1.166	4412	19.7	454	109.8	23.0
0.110	0.002258	107.7	0.171	1.280	5967	24.8	784	109.8	31.7
0.110	0.002729	120.2	0.152	1.429	7257	26.8	1027	109.8	38.3
0.110	0.002729	120.2	0.154	1.429	7314	26.8	1027	109.8	38.3
0.110	0.002942	124.6	0.150	1.481	7745	27.9	1151	109.8	41.3
0.110	0.002942	124.6	0.147	1.481	7687	27.9	1151	109.8	41.3
0.110	0.00338	136.8	0.131	1.626	8704	29.2	1384	109.8	47.4
0.110	0.003384	135.8	0.128	1.614	8676	29.4	1397	109.8	47.5
0.111	0.00164	98.4	0.241	1.170	4450	19.7	453	110.8	23.0
0.111	0.002141	105.0	0.195	1.248	5770	24.1	723	110.8	30.0
0.112	0.00164	97.4	0.259	1.158	4430	19.9	458	111.8	23.0
0.112	0.00164	97.4	0.264	1.158	4420	19.9	458	111.8	23.0
0.112	0.001971	102.9	0.206	1.223	5426	22.6	626	111.8	27.7
0.112	0.002141	104.8	0.196	1.246	5865	24.1	725	111.8	30.0
0.113	0.001971	103.0	0.214	1.224	5427	22.6	625	112.8	27.7
0.113	0.002134	106.6	0.199	1.267	5856	23.6	708	112.8	29.9
0.113	0.002134	106.5	0.200	1.266	5815	23.7	709	112.8	29.9
0.113	0.00242	112.0	0.185	1.331	6578	25.5	866	112.8	34.0
0.113	0.003384	135.8	0.138	1.614	8826	29.4	1397	112.8	47.5
0.113	0.003384	135.7	0.136	1.613	8818	29.4	1398	112.8	47.5
0.114	0.00242	112.3	0.185	1.335	6561	25.4	864	113.8	34.0
0.114	0.002724	119.8	0.165	1.424	7346	26.8	1026	113.8	38.2
0.114	0.002725	119.8	0.168	1.424	7381	26.9	1027	113.8	38.2
0.114	0.003104	129.1	0.147	1.535	8155	28.4	1237	113.8	43.6
0.114	0.003104	129.1	0.147	1.535	8164	28.4	1237	113.8	43.6
0.115	0.00164	106.9	0.259	1.271	4402	18.1	417	114.8	23.0
0.115	0.002937	124.3	0.155	1.477	7829	27.9	1150	114.8	41.2
0.115	0.002937	124.2	0.159	1.476	7819	27.9	1151	114.8	41.2
0.116	0.00164	106.9	0.262	1.271	4393	18.1	417	115.8	23.0
0.117	0.003396	136.3	0.133	1.620	9231	29.4	1402	116.8	47.7
0.119	0.002239	109.0	0.182	1.296	6350	24.3	762	118.8	31.4
0.119	0.002397	112.2	0.175	1.334	6784	25.2	849	118.8	33.6
0.119	0.002397	112.2	0.172	1.334	6763	25.2	849	118.8	33.6
0.119	0.002543	115.6	0.166	1.374	7046	26.0	927	118.8	35.7
0.119	0.002543	115.5	0.163	1.373	7076	26.0	928	118.8	35.7
0.120	0.002239	108.9	0.181	1.294	6387	24.3	763	119.8	31.4
0.120	0.002262	109.7	0.190	1.304	6436	24.3	773	119.8	31.7
0.120	0.003339	135.1	0.136	1.606	9195	29.2	1367	119.8	46.9
0.121	0.002274	109.9	0.183	1.306	6458	24.4	780	120.8	31.9
0.121	0.002274	109.9	0.186	1.306	6419	24.4	780	120.8	31.9
0.121	0.002388	107.7	0.177	1.280	6910	26.2	877	120.8	33.5

Vsl (m/s)	$\dot{m}_g$ (kg/s)	Pabs (kPa)	Ave. film height (mm)	ρ_{gas} (kg/m^3)	$\Delta P/\Delta z$, fric (Pa/m)	Vsg (m/s)	Specific Energy (J/m^3)	G_l (kg/m^{2}s)	G_g (kg/m^{2}s)
0.121	0.003339	135.2	0.136	1.607	9296	29.2	1366	120.8	46.9
0.122	0.002262	109.6	0.187	1.303	6383	24.4	774	121.8	31.7
0.122	0.002388	109.4	0.177	1.300	6872	25.8	864	121.8	33.5
0.123	0.002239	109.3	0.189	1.299	6407	24.2	760	122.8	31.4
0.123	0.002239	109.3	0.188	1.299	6386	24.2	760	122.8	31.4
0.123	0.002278	110.3	0.185	1.311	6534	24.4	780	122.8	32.0
0.123	0.002539	115.6	0.164	1.374	7232	25.9	924	122.8	35.6
0.123	0.002539	115.5	0.162	1.373	7231	26.0	925	122.8	35.6
0.124	0.002278	110.2	0.187	1.310	6562	24.4	780	123.8	32.0
0.126	0.001918	102.5	0.217	1.218	6070	22.1	595	125.7	26.9
0.126	0.001918	102.4	0.216	1.217	6020	22.1	595	125.7	26.9
0.126	0.003339	136.6	0.144	1.624	9405	28.9	1352	125.7	46.9
0.126	0.003339	136.3	0.143	1.620	9411	28.9	1355	125.7	46.9
0.127	0.002538	116.3	0.173	1.382	8111	25.8	918	126.7	35.6
0.128	0.001918	102.7	0.220	1.221	6155	22.1	594	127.7	26.9
0.128	0.002138	107.4	0.197	1.277	6902	23.5	705	127.7	30.0
0.128	0.002538	116.5	0.173	1.385	8101	25.7	916	127.7	35.6
0.129	0.002138	107.4	0.200	1.277	6851	23.5	705	128.7	30.0
0.130	0.001918	102.6	0.223	1.220	6163	22.1	594	129.7	26.9
0.130	0.002238	109.2	0.187	1.298	7080	24.2	760	129.7	31.4
0.131	0.002238	109.3	0.191	1.299	7119	24.2	759	130.7	31.4
0.134	0.001972	104.1	0.219	1.237	6471	22.4	619	133.7	27.7
0.134	0.001972	104.0	0.221	1.236	6397	22.4	620	133.7	27.7
0.135	0.002586	117.6	0.170	1.398	8293	26.0	942	134.7	36.3
0.135	0.002586	117.6	0.168	1.398	8256	26.0	942	134.7	36.3
0.140	0.002254	109.7	0.193	1.304	7606	24.3	767	139.7	31.6
0.141	0.002254	109.8	0.197	1.305	7555	24.2	767	140.7	31.6
0.142	0.002262	111.0	0.199	1.319	7882	24.1	764	141.7	31.7
0.143	0.002134	108.0	0.208	1.284	7614	23.3	699	142.7	29.9
0.143	0.002262	111.0	0.200	1.319	7932	24.1	764	142.7	31.7
0.143	0.002449	114.2	0.189	1.357	8299	25.3	870	142.7	34.4
0.144	0.001312	93.0	0.317	1.105	4638	16.7	307	143.7	18.4
0.144	0.001312	93.0	0.314	1.105	4636	16.7	307	143.7	18.4
0.144	0.002134	108.0	0.207	1.284	7612	23.3	699	143.7	29.9
0.145	0.001849	101.3	0.247	1.204	6647	21.6	559	144.7	25.9
0.145	0.001849	101.3	0.255	1.204	6626	21.6	559	144.7	25.9
0.146	0.001474	94.8	0.291	1.127	5120	18.4	380	145.7	20.7
0.146	0.001474	94.8	0.290	1.127	5125	18.4	380	145.7	20.7
0.148	0.00225	110.8	0.206	1.317	8142	24.0	757	147.7	31.6
0.149	0.00225	110.7	0.208	1.316	8145	24.0	758	148.7	31.6
0.150	0.002134	107.9	0.212	1.283	7770	23.4	699	149.7	29.9
0.150	0.002134	107.9	0.212	1.283	7825	23.4	699	149.7	29.9
0.150	0.002647	120.9	0.176	1.437	9326	25.8	960	149.7	37.1
0.150	0.002648	120.8	0.173	1.436	9413	25.9	962	149.7	37.2
0.151	0.001972	104.2	0.228	1.239	7171	22.3	618	150.7	27.7
0.151	0.001972	104.2	0.230	1.239	7144	22.3	618	150.7	27.7
0.152	0.001806	101.8	0.243	1.210	6695	20.9	531	151.7	25.3
0.152	0.001806	101.7	0.244	1.209	6717	21.0	531	151.7	25.3

Vsl (m/s)	$\dot{m}_g$ (kg/s)	Pabs (kPa)	Ave. film height (mm)	ρ_{gas} (kg/m^3)	$\Delta P/\Delta z$, fric (Pa/m)	Vsg (m/s)	Specific Energy (J/m^3)	G_l (kg/m^{2}s)	G_g (kg/m^{2}s)
0.155	0.001296	92.9	0.357	1.104	4965	16.5	300	154.7	18.2
0.155	0.001296	92.8	0.353	1.103	4920	16.5	300	154.7	18.2
0.155	0.002007	106.0	0.238	1.260	7487	22.4	630	154.7	28.2
0.155	0.002239	111.0	0.212	1.319	8307	23.8	748	154.7	31.4
0.155	0.002239	110.7	0.214	1.316	8374	23.9	750	154.7	31.4
0.155	0.002647	121.1	0.188	1.439	9385	25.8	959	154.7	37.1
0.156	0.002001	106.0	0.240	1.260	7507	22.3	626	155.7	28.1
0.156	0.002647	121.1	0.188	1.439	9386	25.8	959	155.7	37.1
0.157	0.001964	105.2	0.249	1.250	7425	22.0	608	156.7	27.6
0.157	0.001964	105.2	0.253	1.250	7415	22.0	608	156.7	27.6
0.159	0.001972	105.3	0.257	1.252	7300	22.1	612	158.7	27.7
0.159	0.002274	112.3	0.226	1.335	8469	23.9	763	158.7	31.9
0.160	0.002342	120.0	0.234	1.426	8224	23.0	757	159.7	32.9
0.160	0.002343	119.8	0.227	1.424	8285	23.1	759	159.7	32.9
0.163	0.001972	105.2	0.254	1.250	7254	22.1	613	162.7	27.7
0.163	0.002274	112.0	0.224	1.331	8291	24.0	765	162.7	31.9
0.164	0.001639	102.7	0.310	1.221	6307	18.8	433	163.7	23.0
0.164	0.001639	102.7	0.308	1.221	6308	18.8	433	163.7	23.0
0.165	0.001849	102.1	0.283	1.214	7110	21.4	555	164.7	25.9
0.165	0.001849	102.0	0.278	1.212	7133	21.4	555	164.7	25.9
0.168	0.002007	107.5	0.207	1.278	7581	22.0	621	167.7	28.2
0.168	0.002007	107.4	0.210	1.277	7550	22.1	621	167.7	28.2
0.169	0.001805	102.7	0.224	1.221	6898	20.8	526	168.7	25.3
0.169	0.001805	102.7	0.218	1.221	6911	20.8	526	168.7	25.3
0.171	0.001845	104.0	0.225	1.236	7018	20.9	542	170.7	25.9
0.172	0.001845	104.0	0.219	1.236	7080	20.9	542	171.7	25.9
0.173	0.00164	102.2	0.239	1.215	6326	18.9	436	172.7	23.0
0.173	0.00164	102.0	0.237	1.212	6298	19.0	437	172.7	23.0
0.176	0.0024	115.8	0.179	1.376	8517	24.5	824	175.6	33.7
0.176	0.0024	115.7	0.181	1.375	8520	24.5	825	175.6	33.7
0.180	0.001845	104.6	0.225	1.243	7335	20.8	539	179.6	25.9
0.180	0.001845	104.5	0.233	1.242	7309	20.8	540	179.6	25.9
0.181	0.002343	114.7	0.178	1.363	8498	24.1	793	180.6	32.9
0.181	0.002343	114.7	0.177	1.363	8551	24.1	793	180.6	32.9
0.182	0.001845	104.9	0.232	1.247	7414	20.8	538	181.6	25.9
0.182	0.001845	104.8	0.232	1.246	7468	20.8	538	181.6	25.9
0.184	0.002274	113.1	0.183	1.344	8322	23.7	758	183.6	31.9
0.184	0.002274	113.1	0.180	1.344	8416	23.7	758	183.6	31.9
0.186	0.0024	116.3	0.189	1.382	8759	24.4	821	185.6	33.7
0.186	0.0024	116.3	0.187	1.382	8823	24.4	821	185.6	33.7
0.187	0.002133	110.3	0.211	1.311	8362	22.8	683	186.6	29.9
0.187	0.002133	110.3	0.211	1.311	8351	22.8	683	186.6	29.9
0.190	0.001845	104.8	0.229	1.246	7539	20.8	538	189.6	25.9
0.190	0.001845	104.7	0.229	1.245	7508	20.8	539	189.6	25.9
0.190	0.002274	113.9	0.184	1.354	8579	23.6	752	189.6	31.9
0.190	0.002274	113.8	0.187	1.353	8559	23.6	753	189.6	31.9
0.193	0.00238	116.3	0.183	1.382	9143	24.2	807	192.6	33.4
0.193	0.002381	116.0	0.183	1.379	9081	24.2	810	192.6	33.4

Vsl (m/s)	$\dot{m}_g$ (kg/s)	Pabs (kPa)	Ave. film height (mm)	ρ_{gas} (kg/m^3)	$\Delta P/\Delta z$, fric (Pa/m)	Vsg (m/s)	Specific Energy (J/m^3)	G_l (kg/m^{2}s)	G_g (kg/m^{2}s)
0.194	0.002134	115.4	0.211	1.372	8140	21.8	654	193.6	29.9
0.194	0.002134	114.7	0.209	1.363	8143	22.0	658	193.6	29.9
0.194	0.002365	116.1	0.189	1.380	9029	24.1	798	193.6	33.2
0.195	0.002365	116.1	0.185	1.380	9039	24.1	798	194.6	33.2
0.197	0.002072	110.1	0.219	1.309	8499	22.2	646	196.6	29.1
0.197	0.002427	117.4	0.201	1.395	9180	24.4	831	196.6	34.1
0.197	0.002427	117.3	0.195	1.394	9196	24.4	832	196.6	34.1
0.198	0.001474	98.8	0.291	1.174	6514	17.6	364	197.6	20.7
0.198	0.00164	100.6	0.256	1.196	7068	19.2	443	197.6	23.0
0.198	0.00164	100.6	0.253	1.196	7032	19.2	443	197.6	23.0
0.198	0.002072	110.0	0.221	1.307	8568	22.2	647	197.6	29.1
0.198	0.002274	113.9	0.189	1.354	8792	23.6	752	197.6	31.9
0.198	0.002274	113.9	0.193	1.354	8822	23.6	752	197.6	31.9
0.199	0.001474	99.0	0.289	1.177	6499	17.6	364	198.6	20.7
0.203	0.002068	110.6	0.227	1.315	8804	22.1	641	202.6	29.0
0.203	0.002068	110.5	0.225	1.313	8816	22.1	641	202.6	29.0
0.205	0.001845	105.7	0.248	1.256	8036	20.6	534	204.6	25.9
0.206	0.001474	99.2	0.287	1.179	6686	17.5	363	205.6	20.7
0.206	0.001845	105.7	0.252	1.256	8081	20.6	534	205.6	25.9
0.207	0.001474	99.4	0.291	1.182	6715	17.5	362	206.6	20.7
0.208	0.001805	104.7	0.245	1.245	7871	20.4	516	207.6	25.3
0.209	0.001805	104.7	0.244	1.245	7866	20.4	516	208.6	25.3
0.213	0.00164	101.5	0.268	1.206	7453	19.1	439	212.6	23.0
0.214	0.00164	101.5	0.263	1.206	7410	19.1	439	213.6	23.0
0.219	0.00164	101.4	0.280	1.205	7565	19.1	440	218.6	23.0
0.219	0.00164	101.4	0.270	1.205	7559	19.1	440	218.6	23.0
0.226	0.00227	115.5	0.216	1.373	9734	23.2	739	225.5	31.9
0.227	0.00227	115.6	0.215	1.374	9684	23.2	739	226.5	31.9
0.234	0.002258	115.9	0.222	1.378	9880	23.0	729	233.5	31.7
0.234	0.002258	115.7	0.218	1.375	9903	23.0	730	233.5	31.7
0.239	0.00164	102.8	0.281	1.222	8103	18.8	434	238.5	23.0
0.241	0.00164	102.7	0.291	1.221	8086	18.9	434	240.5	23.0
0.245	0.001474	99.8	0.331	1.186	7553	17.4	361	244.5	20.7
0.246	0.001474	99.8	0.320	1.186	7532	17.4	361	245.5	20.7
0.248	0.00164	102.7	0.295	1.221	8317	18.9	434	247.5	23.0
0.249	0.00164	102.8	0.287	1.222	8316	18.8	434	248.5	23.0
0.262	0.001845	108.4	0.292	1.288	9532	20.1	520	261.5	25.9
0.263	0.001845	108.6	0.282	1.291	9597	20.1	519	262.5	25.9
0.269	0.001845	108.9	0.292	1.294	9646	20.0	518	268.5	25.9
0.270	0.001845	108.7	0.295	1.292	9649	20.0	519	269.5	25.9
0.274	0.001845	109.1	0.293	1.297	9748	20.0	517	273.5	25.9
0.275	0.001845	109.0	0.287	1.296	9745	20.0	517	274.5	25.9
0.284	0.002274	119.4	0.251	1.419	11330	22.5	718	283.4	31.9
0.285	0.002274	119.7	0.248	1.423	11308	22.4	716	284.4	31.9
0.288	0.00225	118.7	0.251	1.411	11416	22.4	707	287.4	31.6
0.288	0.00225	118.7	0.254	1.411	11338	22.4	707	287.4	31.6
0.314	0.00164	106.0	0.331	1.260	9755	18.3	420	313.4	23.0
0.315	0.00164	106.0	0.332	1.260	9799	18.3	420	314.4	23.0

B.2 AIR-WATER MICROGRAVITY DATA

Vsl (m/s)	$\dot{m}_g$ (kg/s)	Pabs (kPa)	Ave. film height (mm)	ρ_{gas} (kg/m^3)	$\Delta P/\Delta z$, fric (Pa/m)	Vsg (m/s)	Specific Energy (J/m^3)	G_l (kg/m^{2}s)	G_g (kg/m^{2}s)
0.093	0.002136	85.8	0.340	1.020	5937	29.4	881	92.8	30.0
0.100	0.001830	118.9	0.591	1.413	4003	18.2	467	100.0	25.7
0.107	0.002143	98.6	0.519	1.172	6340	25.7	772	106.9	30.1
0.107	0.002142	98.9	0.519	1.176	6264	25.6	769	106.9	30.1
0.108	0.002143	99.3	0.524	1.180	6432	25.5	766	107.5	30.1
0.108	0.002262	91.6	0.460	1.089	6845	29.2	926	107.9	31.7
0.109	0.002422	96.2	0.498	1.143	7689	29.7	1010	108.3	34.0
0.109	0.002422	95.8	0.491	1.139	7822	29.8	1015	108.4	34.0
0.109	0.002728	98.1	0.490	1.166	9280	32.8	1257	108.5	38.3
0.109	0.003111	102.3	0.482	1.216	10273	35.9	1568	108.5	43.7
0.109	0.002423	97.4	0.499	1.158	7665	29.4	999	108.6	34.0
0.109	0.003105	102.7	0.479	1.221	10284	35.7	1555	108.7	43.6
0.109	0.003380	108.6	0.472	1.291	11141	36.7	1743	109.1	47.4
0.109	0.003111	102.7	0.485	1.221	10034	35.8	1561	109.2	43.7
0.110	0.003383	108.0	0.467	1.284	11083	37.0	1756	109.3	47.5
0.110	0.002725	95.3	0.489	1.133	8911	33.8	1291	109.5	38.2
0.110	0.002726	94.4	0.492	1.122	9050	34.1	1304	109.7	38.3
0.111	0.002943	102.8	0.481	1.222	9789	33.8	1396	111.1	41.3
0.112	0.002940	101.9	0.483	1.211	9603	34.1	1406	111.4	41.3
0.112	0.002940	101.7	0.486	1.209	9406	34.1	1408	111.6	41.3
0.112	0.001970	87.1	0.415	1.035	5555	26.7	738	111.9	27.6
0.113	0.001640	99.9	0.569	1.187	4349	19.4	446	112.8	23.0
0.113	0.001640	97.1	0.563	1.154	4427	19.9	459	113.0	23.0
0.118	0.003340	106.8	0.470	1.269	11906	36.9	1731	118.1	46.9
0.119	0.002386	92.4	0.499	1.098	8648	30.5	1021	118.4	33.5
0.119	0.003340	107.0	0.474	1.272	11653	36.9	1728	118.5	46.9
0.119	0.003341	106.9	0.474	1.271	11366	36.9	1730	118.9	46.9
0.120	0.002240	108.3	0.531	1.287	6551	24.4	768	119.9	31.4
0.120	0.002397	91.6	0.495	1.089	8428	30.9	1039	119.9	33.6
0.120	0.002238	109.0	0.533	1.296	6697	24.2	761	119.9	31.4
0.120	0.002538	101.3	0.505	1.204	8384	29.6	1054	120.0	35.6
0.120	0.002542	102.5	0.510	1.218	8590	29.3	1045	120.2	35.7
0.121	0.002538	101.1	0.507	1.202	8566	29.6	1056	120.5	35.6
0.121	0.002273	91.2	0.512	1.084	8138	29.4	939	120.8	31.9
0.121	0.002260	91.5	0.513	1.088	8393	29.2	925	120.8	31.7
0.123	0.002239	109.2	0.531	1.298	6776	24.2	761	122.4	31.4
0.126	0.001919	89.1	0.537	1.059	6765	25.4	685	125.5	26.9
0.126	0.001919	90.4	0.531	1.075	6716	25.1	675	125.7	26.9
0.136	0.002584	100.2	0.496	1.191	9780	30.4	1104	135.8	36.3
0.140	0.002254	96.5	0.522	1.147	8741	27.6	872	139.9	31.6
0.142	0.001815	103.4	0.559	1.229	6281	20.7	528	141.8	25.5
0.143	0.001847	97.0	0.520	1.153	5365	22.5	583	142.5	25.9
0.144	0.002136	97.4	0.430	1.158	6938	25.9	776	143.3	30.0

Vsl (m/s)	$\dot{m}_g$ (kg/s)	Pabs (kPa)	Ave. film height (mm)	ρ_{gas} (kg/m^3)	$\Delta P/\Delta z$, fric (Pa/m)	Vsg (m/s)	Specific Energy (J/m^3)	G_l (kg/m^{2}s)	G_g (kg/m^{2}s)
0.144	0.002262	98.6	0.519	1.172	8622	27.1	860	143.6	31.7
0.150	0.002136	100.9	0.434	1.199	7025	25.0	749	150.0	30.0
0.150	0.001969	93.8	0.537	1.115	7882	24.8	685	150.0	27.6
0.151	0.002647	89.8	0.479	1.067	10351	34.8	1293	151.2	37.1
0.152	0.002647	90.1	0.484	1.071	10077	34.7	1289	151.3	37.1
0.155	0.001966	91.4	0.530	1.086	7540	25.4	701	155.1	27.6
0.156	0.002008	100.3	0.554	1.192	7669	23.6	666	156.0	28.2
0.157	0.002009	99.5	0.553	1.183	7992	23.8	672	156.7	28.2
0.158	0.002272	96.7	0.517	1.149	8482	27.7	885	158.0	31.9
0.160	0.001970	94.9	0.455	1.128	7421	24.5	678	159.9	27.6
0.161	0.002341	119.6	0.543	1.422	8265	23.1	759	161.0	32.9
0.163	0.001640	102.9	0.671	1.223	5484	18.8	433	162.8	23.0
0.166	0.001847	88.7	0.594	1.054	7306	24.6	637	166.1	25.9
0.170	0.001805	98.8	0.516	1.174	6172	21.6	546	169.7	25.3
0.175	0.002404	97.1	0.522	1.154	10964	29.2	986	174.8	33.7
0.176	0.002401	98.9	0.525	1.176	10843	28.7	966	175.9	33.7
0.177	0.001847	99.8	0.638	1.186	7252	21.9	566	176.6	25.9
0.179	0.001847	102.4	0.635	1.217	6861	21.3	552	178.5	25.9
0.179	0.001847	98.9	0.651	1.176	7224	22.0	571	179.0	25.9
0.185	0.002274	93.2	0.523	1.108	10781	28.8	919	184.3	31.9
0.187	0.002275	93.7	0.528	1.114	10581	28.7	915	186.2	31.9
0.188	0.002274	95.6	0.530	1.136	10607	28.1	896	187.9	31.9
0.192	0.002136	116.2	0.647	1.381	7448	21.7	651	191.8	30.0
0.193	0.002362	92.6	0.526	1.101	11326	30.1	998	192.7	33.1
0.194	0.002380	94.7	0.528	1.126	11266	29.7	991	193.3	33.4
0.195	0.002074	98.5	0.544	1.171	9830	24.9	724	195.0	29.1
0.195	0.001640	78.7	0.563	0.935	7572	24.6	566	195.1	23.0
0.196	0.002074	99.4	0.543	1.182	9603	24.6	717	195.3	29.1
0.198	0.001640	91.6	0.630	1.089	6505	21.1	487	197.2	23.0
0.198	0.001640	75.9	0.572	0.902	7802	25.5	587	197.8	23.0
0.199	0.001475	89.8	0.619	1.067	5768	19.4	401	198.2	20.7
0.206	0.001474	86.8	0.615	1.032	5915	20.0	415	205.5	20.7
0.212	0.001640	82.0	0.686	0.975	8030	23.6	543	211.5	23.0
0.227	0.002271	98.2	0.603	1.167	10996	27.3	870	226.2	31.9
0.240	0.001640	99.3	0.742	1.180	7923	19.5	449	239.4	23.0
0.263	0.001846	103.9	0.749	1.235	9160	21.0	543	262.0	25.9
0.264	0.001846	104.2	0.748	1.239	9063	20.9	542	263.7	25.9
0.267	0.001847	89.3	0.711	1.061	10255	24.4	633	266.5	25.9
0.285	0.002256	98.9	0.656	1.176	12184	26.9	853	284.3	31.7
0.286	0.002255	99.0	0.649	1.177	12465	26.9	851	285.0	31.6
0.286	0.002250	98.9	0.654	1.176	12214	26.9	848	285.1	31.6
0.314	0.001640	97.8	0.827	1.162	9697	19.8	456	313.0	23.0

B.3 AIR-WATER HYPERGRAVITY DATA

Vsl (m/s)	$\dot{m}_g$ (kg/s)	Pabs (kPa)	Ave. film height (mm)	ρ_{gas} (kg/m^3)	$\Delta P/\Delta z$, fric (Pa/m)	Vsg (m/s)	Specific Energy (J/m^3)	G_l (kg/m^{2}s)	G_g (kg/m^{2}s)
0.075	0.001475	109.9	0.526	1.306	1984	15.8	328	74.6	20.7
0.081	0.001970	73.9	0.321	0.878	6677	31.5	870	80.5	27.6
0.093	0.001805	75.5	0.368	0.897	6648	28.2	715	92.8	25.3
0.097	0.001681	74.7	0.441	0.888	6315	26.6	627	96.9	23.6
0.099	0.001765	84.0	0.434	0.998	6316	24.8	614	98.9	24.8
0.102	0.001018	84.7	0.677	1.007	4045	14.2	203	101.4	14.3
0.102	0.001558	74.6	0.434	0.887	6150	24.7	539	101.4	21.9
0.103	0.002367	93.4	0.558	1.110	8179	29.9	994	102.6	33.2
0.103	0.002387	92.9	0.548	1.104	7191	30.3	1016	102.8	33.5
0.104	0.001823	109.1	0.601	1.297	4737	19.7	505	104.1	25.6
0.109	0.002256	92.2	0.479	1.096	8212	28.9	915	109.2	31.7
0.110	0.001640	76.5	0.429	0.909	6775	25.3	583	110.0	23.0
0.112	0.002142	99.1	0.527	1.178	8058	25.5	767	112.2	30.1
0.113	0.002135	85.8	0.393	1.020	8075	29.4	880	112.4	30.0
0.113	0.002724	98.5	0.490	1.171	10539	32.7	1248	112.7	38.2
0.113	0.002422	98.0	0.508	1.165	9645	29.2	992	112.8	34.0
0.114	0.003106	103.3	0.487	1.228	11298	35.5	1547	113.9	43.6
0.115	0.003383	108.8	0.480	1.293	13186	36.7	1743	114.6	47.5
0.116	0.001639	97.0	0.572	1.153	6364	19.9	459	116.0	23.0
0.117	0.002939	103.1	0.487	1.225	11146	33.7	1388	116.5	41.2
0.124	0.002279	92.0	0.512	1.094	10467	29.2	935	124.0	32.0
0.125	0.003339	107.6	0.476	1.279	14752	36.6	1717	124.3	46.9
0.127	0.002139	100.1	0.538	1.190	9410	25.2	757	126.3	30.0
0.127	0.002537	102.3	0.513	1.216	10665	29.3	1043	126.4	35.6
0.130	0.002237	108.4	0.538	1.288	8908	24.4	765	129.7	31.4
0.130	0.001918	90.7	0.541	1.078	9450	25.0	672	129.8	26.9
0.135	0.001969	87.1	0.454	1.035	7931	26.7	738	134.6	27.6
0.141	0.002447	100.1	0.500	1.190	11102	28.9	991	140.9	34.3
0.144	0.001310	73.5	0.531	0.874	6567	21.0	387	144.1	18.4
0.146	0.001475	75.7	0.591	0.900	6226	23.0	476	145.6	20.7
0.148	0.002252	95.1	0.528	1.130	11558	28.0	884	148.0	31.6
0.151	0.001971	101.8	0.574	1.210	9925	22.9	632	150.8	27.7
0.151	0.001805	96.6	0.537	1.148	6603	22.1	559	151.1	25.3
0.154	0.002239	95.4	0.529	1.134	9885	27.7	871	153.8	31.4
0.154	0.001298	76.0	0.572	0.903	6636	20.2	367	154.1	18.2
0.155	0.002647	94.1	0.496	1.119	13757	33.2	1234	154.9	37.1
0.157	0.001965	89.9	0.544	1.069	10698	25.8	712	156.5	27.6
0.168	0.002008	95.9	0.559	1.140	10518	24.7	697	168.1	28.2
0.172	0.001846	91.2	0.613	1.084	9006	23.9	619	171.3	25.9
0.172	0.001639	102.6	0.699	1.220	7605	18.9	434	171.8	23.0
0.180	0.002342	92.7	0.530	1.102	12282	29.8	980	180.0	32.9
0.185	0.001847	100.0	0.624	1.189	7764	21.8	565	184.4	25.9
0.185	0.002403	95.4	0.533	1.134	13549	29.7	1003	184.5	33.7
0.188	0.002135	100.8	0.494	1.198	9577	25.0	749	187.8	30.0
0.190	0.001845	101.6	0.643	1.208	8965	21.4	555	189.9	25.9
0.191	0.002135	116.6	0.589	1.386	8366	21.6	648	190.1	30.0

Vsl (m/s)	$\dot{m}_g$ (kg/s)	Pabs (kPa)	Ave. film height (mm)	ρ_{gas} (kg/m^3)	$\Delta P/\Delta z$, fric (Pa/m)	Vsg (m/s)	Specific Energy (J/m^3)	G_l (kg/m^{2}s)	G_g (kg/m^{2}s)
0.195	0.001640	94.8	0.653	1.127	7411	20.4	470	194.5	23.0
0.197	0.002273	93.2	0.541	1.108	14121	28.8	919	196.1	31.9
0.198	0.002429	93.7	0.537	1.114	13918	30.6	1043	198.1	34.1
0.203	0.002071	93.4	0.559	1.110	12886	26.2	761	202.6	29.1
0.207	0.001846	100.4	0.697	1.193	9667	21.7	562	206.3	25.9
0.212	0.001804	100.6	0.587	1.196	8005	21.2	536	212.0	25.3
0.218	0.001639	83.3	0.711	0.990	9806	23.2	534	217.8	23.0
0.233	0.002258	100.8	0.623	1.198	12748	26.4	838	232.4	31.7
0.243	0.001640	80.8	0.642	0.960	9730	24.0	552	242.6	23.0
0.247	0.001475	88.4	0.673	1.051	8721	19.7	408	246.4	20.7
0.249	0.001639	98.2	0.765	1.167	10164	19.7	453	248.9	23.0
0.269	0.001845	90.5	0.740	1.076	12071	24.1	623	268.1	25.9
0.277	0.001845	104.4	0.797	1.241	11507	20.9	540	276.4	25.9
0.286	0.002274	100.3	0.666	1.192	14810	26.8	854	285.0	31.9
0.314	0.001639	98.3	0.830	1.168	11684	19.7	453	313.0	23.0
0.314	0.001639	94.8	0.872	1.127	12018	20.4	470	313.6	23.0

APPENDIX C: HELIUM-WATER DATA

The helium water data collected during this investigation is presented in the following sections.

C.1 HELIUM-WATER NORMAL GRAVITY DATA

Vsl (m/s)	$\dot{m}_g$ (kg/s)	Pabs (kPa)	Ave. film height (mm)	ρ_{gas} (kg/m^3)	$\Delta P/\Delta z$, fric (Pa/m)	Vsg (m/s)	Specific Energy (J/m^3)	G_l (kg/m^{2}s)	G_g (kg/m^{2}s)
0.098	0.000358	138.0	0.398	0.2267	2706	22.2	111	97.8	5.0
0.098	0.000358	138.0	0.465	0.2267	2732	22.2	111	97.8	5.0
0.102	0.000647	103.8	0.201	0.1705	4777	53.3	484	101.8	9.1
0.103	0.000647	103.8	0.215	0.1705	4806	53.3	484	102.8	9.1
0.108	0.000648	104.1	0.211	0.1710	4974	53.2	484	107.8	9.1
0.108	0.000648	104.0	0.210	0.1708	4991	53.2	484	107.8	9.1
0.109	0.000731	108.3	0.172	0.1779	5876	57.7	592	108.8	10.3
0.110	0.000731	108.3	0.171	0.1779	5880	57.7	592	109.8	10.3
0.111	0.000828	113.4	0.169	0.1863	6384	62.4	725	110.8	11.6
0.111	0.000828	113.4	0.171	0.1863	6352	62.4	725	110.8	11.6
0.113	0.000647	104.3	0.212	0.1713	5141	53.0	481	112.8	9.1
0.113	0.000647	104.2	0.206	0.1711	5156	53.1	482	112.8	9.1
0.116	0.000760	109.5	0.186	0.1798	6386	59.3	633	115.8	10.7
0.116	0.000760	109.4	0.175	0.1797	6368	59.4	633	115.8	10.7
0.118	0.000660	105.1	0.217	0.1726	5393	53.7	497	117.8	9.3
0.118	0.000660	105.0	0.220	0.1725	5427	53.7	497	117.8	9.3
0.118	0.000730	107.8	0.196	0.1771	6175	57.9	593	117.8	10.2
0.118	0.000828	113.7	0.177	0.1867	6617	62.2	723	117.8	11.6
0.118	0.000828	113.6	0.179	0.1866	6575	62.3	724	117.8	11.6
0.119	0.000490	98.0	0.276	0.1610	4231	42.7	294	118.8	6.9
0.119	0.000729	107.7	0.195	0.1769	6250	57.8	592	118.8	10.2
0.120	0.000490	97.9	0.283	0.1608	4288	42.8	294	119.8	6.9
0.121	0.000813	112.8	0.176	0.1853	6759	61.6	703	120.8	11.4
0.121	0.000813	112.8	0.181	0.1853	6799	61.6	703	120.8	11.4
0.121	0.000813	112.8	0.185	0.1853	6813	61.6	703	120.8	11.4
0.127	0.000403	98.5	0.329	0.1618	3854	35.0	198	126.7	5.7
0.127	0.000403	98.4	0.323	0.1616	3883	35.0	198	126.7	5.7
0.127	0.000660	106.1	0.226	0.1743	5761	53.2	492	126.7	9.3
0.127	0.000660	106.0	0.223	0.1741	5730	53.2	493	126.7	9.3

Vsl (m/s)	$\dot{m}_g$ (kg/s)	Pabs (kPa)	Ave. film height (mm)	ρ_{gas} (kg/m^3)	$\Delta P/\Delta z$, fric (Pa/m)	Vsg (m/s)	Specific Energy (J/m^3)	G_l (kg/m^{2}s)	G_g (kg/m^{2}s)
0.127	0.000758	109.9	0.196	0.1805	6733	58.9	627	126.7	10.6
0.127	0.000758	109.9	0.191	0.1805	6716	58.9	627	126.7	10.6
0.141	0.000828	128.6	0.180	0.2112	7343	55.0	639	140.7	11.6
0.142	0.000828	128.6	0.186	0.2112	7328	55.0	639	141.7	11.6
0.146	0.000828	128.8	0.188	0.2115	7432	54.9	638	145.7	11.6
0.147	0.000828	128.8	0.190	0.2115	7539	54.9	638	146.7	11.6
0.164	0.000828	118.8	0.183	0.1951	8569	59.6	692	163.7	11.6
0.164	0.000828	118.5	0.176	0.1946	8626	59.7	694	163.7	11.6
0.167	0.000690	109.8	0.258	0.1803	7268	53.7	520	166.7	9.7
0.167	0.000828	119.2	0.187	0.1958	8671	59.4	690	166.7	11.6
0.167	0.000828	118.7	0.184	0.1950	8673	59.6	693	166.7	11.6
0.169	0.000403	98.5	0.412	0.1618	5322	35.0	198	168.7	5.7
0.169	0.000403	98.5	0.398	0.1618	5306	35.0	198	168.7	5.7
0.171	0.000689	110.7	0.244	0.1818	7485	53.2	514	170.7	9.7
0.171	0.000774	114.6	0.211	0.1882	8577	57.7	627	170.7	10.9
0.171	0.000774	114.6	0.217	0.1882	8594	57.7	627	170.7	10.9
0.172	0.000689	110.6	0.242	0.1817	7558	53.2	515	171.7	9.7
0.173	0.000403	97.7	0.423	0.1605	4929	35.2	199	172.7	5.7
0.173	0.000774	115.0	0.222	0.1889	8613	57.5	625	172.7	10.9
0.174	0.000774	114.8	0.217	0.1886	8647	57.6	626	173.7	10.9
0.175	0.000403	97.4	0.416	0.1600	4967	35.4	200	174.7	5.7
0.176	0.000359	107.7	0.472	0.1769	4400	28.5	143	175.6	5.0
0.176	0.000828	134.2	0.198	0.2204	8708	52.7	613	175.6	11.6
0.177	0.000828	134.3	0.194	0.2206	8748	52.7	612	176.6	11.6
0.178	0.000359	109.2	0.498	0.1794	4428	28.1	142	177.6	5.0
0.182	0.000828	120.3	0.194	0.1976	9295	58.8	683	181.6	11.6
0.183	0.000700	112.6	0.242	0.1849	8541	53.1	522	182.6	9.8
0.183	0.000828	120.1	0.199	0.1973	9364	58.9	685	182.6	11.6
0.185	0.000465	103.7	0.393	0.1703	5652	38.3	250	184.6	6.5
0.185	0.000465	103.7	0.401	0.1703	5580	38.3	250	184.6	6.5
0.187	0.000700	111.9	0.235	0.1838	8265	53.5	525	186.6	9.8
0.190	0.000813	120.2	0.212	0.1974	9722	57.8	659	189.6	11.4
0.191	0.000813	120.4	0.212	0.1977	9606	57.7	658	190.6	11.4
0.195	0.000700	113.0	0.258	0.1856	8718	52.9	520	194.6	9.8
0.196	0.000828	121.2	0.204	0.1991	9815	58.4	678	195.6	11.6
0.197	0.000828	122.2	0.215	0.2007	10256	57.9	673	196.6	11.6
0.198	0.000828	121.3	0.205	0.1992	10007	58.3	678	197.6	11.6
0.199	0.000700	113.3	0.253	0.1861	8708	52.8	519	198.6	9.8
0.200	0.000403	104.9	0.417	0.1723	5981	32.8	186	199.6	5.7
0.200	0.000403	104.8	0.430	0.1721	6007	32.9	186	199.6	5.7
0.200	0.000828	122.5	0.211	0.2012	10265	57.8	671	199.6	11.6
0.214	0.000404	97.0	0.428	0.1593	6385	35.6	202	213.6	5.7
0.214	0.000404	97.0	0.415	0.1593	6326	35.6	202	213.6	5.7
0.214	0.000735	117.0	0.259	0.1922	9665	53.7	554	213.6	10.3
0.215	0.000735	117.1	0.259	0.1923	9834	53.6	553	214.6	10.3
0.217	0.000404	97.5	0.436	0.1601	6307	35.4	201	216.6	5.7
0.218	0.000404	97.4	0.465	0.1600	6348	35.4	201	217.6	5.7
0.219	0.000735	117.9	0.267	0.1936	9872	53.3	549	218.6	10.3

Vsl (m/s)	$\dot{m}_g$ (kg/s)	Pabs (kPa)	Ave. film height (mm)	ρ_{gas} (kg/m^3)	$\Delta P/\Delta z$, fric (Pa/m)	Vsg (m/s)	Specific Energy (J/m^3)	G_l (kg/m^{2}s)	G_g (kg/m^{2}s)
0.220	0.000735	118.2	0.267	0.1941	9975	53.1	548	219.6	10.3
0.221	0.000735	115.6	0.208	0.1899	9654	54.3	560	220.8	10.3
0.221	0.000735	115.3	0.213	0.1894	9784	54.5	562	220.8	10.3
0.223	0.000404	97.3	0.333	0.1598	6113	35.5	201	222.3	5.7
0.223	0.000828	124.6	0.217	0.2046	10901	56.8	660	222.6	11.6
0.223	0.000403	97.4	0.366	0.1600	6214	35.4	200	222.6	5.7
0.223	0.000404	97.7	0.361	0.1605	5961	35.3	200	222.6	5.7
0.224	0.000402	97.4	0.365	0.1600	6217	35.3	199	223.1	5.6
0.224	0.000828	124.5	0.213	0.2045	10957	56.8	660	223.6	11.6
0.225	0.000735	117.6	0.218	0.1931	9652	53.4	551	224.7	10.3
0.225	0.000735	117.2	0.210	0.1925	9854	53.6	553	224.8	10.3
0.227	0.000444	99.5	0.330	0.1634	6455	38.1	238	226.3	6.2
0.227	0.000444	99.5	0.335	0.1634	6588	38.1	238	226.5	6.2
0.227	0.000828	125.9	0.252	0.2068	11128	56.2	653	226.5	11.6
0.229	0.000828	126.0	0.247	0.2069	11196	56.2	652	228.5	11.6
0.236	0.000404	105.8	0.359	0.1738	6138	32.6	185	235.8	5.7
0.236	0.000404	105.8	0.374	0.1738	6128	32.6	185	235.9	5.7
0.242	0.000360	97.9	0.381	0.1608	6200	31.4	159	241.6	5.1
0.242	0.000360	97.2	0.398	0.1596	6007	31.6	160	241.8	5.1
0.251	0.000490	101.9	0.317	0.1674	7662	41.1	283	250.6	6.9
0.252	0.000490	101.8	0.313	0.1672	7627	41.1	283	251.0	6.9
0.253	0.000360	98.7	0.422	0.1621	6262	31.2	157	252.7	5.1
0.253	0.000360	97.8	0.419	0.1606	6279	31.5	159	252.8	5.1
0.286	0.000404	101.4	0.373	0.1665	7605	34.0	193	285.9	5.7
0.287	0.000404	101.3	0.392	0.1664	7519	34.1	193	286.6	5.7
0.292	0.000404	100.5	0.377	0.1651	7674	34.3	195	291.1	5.7
0.293	0.000404	100.8	0.395	0.1656	7672	34.2	194	292.3	5.7
0.299	0.000490	104.5	0.343	0.1716	8887	40.1	276	298.7	6.9
0.299	0.000490	104.8	0.347	0.1721	9018	40.0	275	298.9	6.9
0.312	0.000360	100.1	0.426	0.1644	7559	30.7	155	311.1	5.1
0.312	0.000360	100.3	0.452	0.1647	7568	30.7	155	311.7	5.1

C.2 HELIUM-WATER MICROGRAVITY DATA

Vsl (m/s)	$\dot{m}_g$ (kg/s)	Pabs (kPa)	Ave. film height (mm)	ρ_{gas} (kg/m^3)	$\Delta P/\Delta z$, fric (Pa/m)	Vsg (m/s)	Specific Energy (J/m^3)	G_l (kg/m^{2}s)	G_g (kg/m^{2}s)
0.102	0.000647	102.2	0.525	0.1679	4301	54.1	491	102.0	9.1
0.107	0.000731	96.3	0.514	0.1582	5705	64.9	665	106.6	10.3
0.108	0.000648	102.9	0.539	0.1690	4525	53.8	489	107.6	9.1
0.109	0.000731	97.0	0.520	0.1593	5460	64.4	661	108.4	10.3
0.109	0.000832	93.3	0.495	0.1532	6885	76.2	890	109.0	11.7
0.110	0.000832	91.8	0.492	0.1508	6719	77.4	904	109.8	11.7
0.115	0.000759	100.5	0.526	0.1651	6069	64.5	687	115.1	10.7
0.116	0.000759	100.5	0.528	0.1651	6132	64.5	687	115.6	10.7
0.116	0.000659	94.1	0.537	0.1546	5372	59.8	553	115.6	9.2
0.116	0.000844	155.6	0.554	0.2556	5056	46.3	549	115.7	11.8
0.117	0.000760	101.2	0.529	0.1662	6070	64.2	684	116.4	10.7
0.117	0.000659	94.5	0.544	0.1552	5317	59.6	551	116.4	9.2
0.118	0.000845	154.6	0.559	0.2539	5110	46.7	554	117.4	11.9
0.121	0.000813	173.0	0.582	0.2841	4947	40.2	458	120.8	11.4
0.126	0.000403	107.5	0.784	0.1766	2587	32.0	181	126.2	5.7
0.139	0.000845	128.6	0.557	0.2112	6775	56.1	666	138.3	11.9
0.147	0.000845	128.9	0.582	0.2117	6593	56.0	664	147.0	11.9
0.167	0.000690	93.6	0.555	0.1537	7586	63.0	610	166.9	9.7
0.168	0.000403	101.1	0.813	0.1660	3406	34.1	193	167.5	5.7
0.169	0.000774	92.0	0.534	0.1511	7395	71.9	781	168.6	10.9
0.170	0.000774	91.3	0.537	0.1500	7685	72.4	787	169.3	10.9
0.177	0.000844	134.2	0.615	0.2204	7618	53.7	637	176.6	11.8
0.187	0.000465	104.2	0.698	0.1711	4516	38.1	249	186.2	6.5
0.191	0.000700	98.5	0.578	0.1618	7785	60.7	597	190.6	9.8
0.191	0.000700	99.2	0.580	0.1629	7156	60.3	592	190.6	9.8
0.198	0.000845	114.5	0.611	0.1881	8111	63.1	748	198.1	11.9
0.199	0.000403	105.4	0.833	0.1731	4201	32.7	185	198.4	5.7
0.213	0.000403	91.3	0.827	0.1500	4571	37.7	213	212.7	5.7
0.215	0.000736	95.5	0.594	0.1569	7570	65.9	680	214.3	10.3
0.220	0.000737	94.8	0.596	0.1557	7730	66.4	687	219.5	10.3
0.220	0.000736	95.5	0.598	0.1569	8302	65.9	680	220.0	10.3
0.225	0.000403	91.4	0.759	0.1501	3499	37.7	213	224.1	5.7
0.244	0.000359	95.1	0.931	0.1562	4689	32.3	163	243.5	5.0
0.290	0.000403	102.3	0.936	0.1680	6124	33.7	190	289.7	5.7
0.299	0.000490	87.0	0.862	0.1429	7482	48.1	331	298.6	6.9

C.3 HELIUM-WATER HYPERGRAVITY DATA

Vsl (m/s)	$\dot{m}_g$ (kg/s)	Pabs (kPa)	Ave. film height (mm)	ρ_{gas} (kg/m^3)	$\Delta P/\Delta z$, fric (Pa/m)	Vsg (m/s)	Specific Energy (J/m^3)	G_l (kg/m^{2}s)	G_g (kg/m^{2}s)
0.099	0.000358	138.0	0.941	0.2267	3756	22.2	111	98.3	5.0
0.114	0.000647	101.3	0.541	0.1664	7263	54.6	496	113.8	9.1
0.117	0.000831	92.8	0.512	0.1524	10003	76.5	892	116.5	11.7
0.117	0.000731	97.1	0.531	0.1595	8401	64.3	660	116.6	10.3
0.118	0.000490	98.8	0.708	0.1623	5019	42.4	291	117.5	6.9
0.126	0.000659	93.5	0.551	0.1536	6978	60.2	557	125.5	9.2
0.127	0.000403	105.8	0.890	0.1738	4920	32.5	184	126.8	5.7
0.127	0.000759	100.7	0.542	0.1654	8492	64.4	686	126.9	10.7
0.162	0.000845	91.6	0.542	0.1504	12299	78.8	935	161.8	11.9
0.169	0.000845	96.7	0.530	0.1588	13614	74.7	885	168.8	11.9
0.172	0.000774	98.6	0.537	0.1619	12629	67.1	729	171.3	10.9
0.173	0.000403	99.3	0.859	0.1631	6051	34.7	196	172.3	5.7
0.173	0.000689	100.9	0.557	0.1657	10244	58.3	564	172.9	9.7
0.174	0.000359	105.3	0.973	0.1729	5507	29.1	147	173.9	5.0
0.178	0.000845	94.0	0.556	0.1544	12647	76.8	911	178.0	11.9
0.192	0.000813	99.9	0.555	0.1641	14906	69.5	793	191.7	11.4
0.199	0.000700	99.2	0.593	0.1629	11212	60.3	592	198.8	9.8
0.220	0.000403	93.6	0.901	0.1537	7431	36.8	208	219.7	5.7
0.223	0.000845	98.7	0.596	0.1621	14536	73.2	868	222.8	11.9
0.228	0.000444	101.9	0.723	0.1674	8642	37.2	232	228.0	6.2
0.230	0.000736	95.5	0.611	0.1569	12810	65.9	680	229.6	10.3
0.235	0.000403	105.8	0.954	0.1738	7611	32.5	184	234.1	5.7
0.249	0.000359	90.5	0.974	0.1486	7553	33.9	171	248.5	5.0
0.250	0.000490	80.2	0.806	0.1317	10009	52.2	359	249.3	6.9
0.295	0.000403	99.1	0.929	0.1628	9439	34.7	196	294.5	5.7
0.298	0.000490	89.1	0.866	0.1463	10870	47.0	323	297.1	6.9
0.310	0.000359	88.5	0.992	0.1454	9354	34.7	175	309.6	5.0

APPENDIX D: SAMPLE OF FLOW IMAGES

Digital images of the two-phase flows were recorded using a digital video camera. The camera was set to a shutter speed of $^{1}/_{4000}{}^{th}$ of a second, with frame rate of 30 images per second. Due to the slow frame rate and the large flow rate, the flow cannot be continuously examined. Many features of the flow may be present in one frame, but not in subsequent frame. However, the images do provide a general indication of the flow.

The viewing section through which the flow images were recorded is made of solid acrylic. Solid blocks of acrylic were bored to the correct tube diameter in order to attempt to reduce the distortion caused by viewing through a solid-liquid interface, as previously seen with glycerol-water solution filled viewing sections. However, by observing the flow perpendicular to the direction of flow, the distortion caused by the interfaces cannot be eliminated. The different interfaces present in annular flow (tube wall – liquid annulus, liquid annulus – gas core, gas core – liquid annulus and liquid annulus – tube wall) all can cause the image to distort.

The images presented here are typical for the range of flow rates. Changes in the flow due to the change of the gas or liquid flow rates are not apparent in the video images. Each flow image is of air-water flow, taken at approximately the same flow conditions.

The normal gravity air-water flow is shown in Figure D.1, taken at a liquid flow rate of 0.288 m/s and a gas flow rate of 0.00225 kg/s. The image shows the waves of the annular flow, as well as some entrained liquid bubbles in the gas core. Some of the waves appear to be in the process of being sheared off the annulus.

Figure D.2 shows the microgravity air-water flow. The liquid flow is at 0.286 m/s and the gas flow rate is 0.00225 kg/s. As with the normal gravity flow, the microgravity image shows the features of annular flow: waves near the tube walls, entrained liquid bubbles and undercutting or shearing off of the liquid.

Figure D.1. Normal gravity air-water flow, V_{sl} = 0.288 m/s, $\dot{m}_g$ = 0.00225 kg/s.

Figure D.2. Microgravity air-water flow, V_{sl} = 0.286 m/s, $\dot{m}_g$ = 0.00225 kg/s.

Figure D.3 shows the hypergravity air-water flow. The liquid flow is at 0.286 m/s and the gas flow rate is 0.00227 kg/s. Unlike the normal gravity and microgravity flows, the hypergravity flow appears quite chaotic. No distinct surface waves can be seen, and the liquid appears to be creating bridges across the tube diameter. Based on this flow observation, it is possible that the hypergravity flows at the same set points as the normal and microgravity flows is not, in fact, in annular flow, but rather a churn type flow regime. Further research into the hypergravity flow regimes is required.

Figure D.3. Hypergravity air-water flow, V_{sl} = 0.286 m/s, $\dot{m}_g$ = 0.00227 kg/s.